POLITECNICO DI MILANO

Department of Mechanical Engineering
Doctoral Programme In Mechanical Engineering

SHEAR-MODE PROPAGATION OF SHORT CRACKS UNDER ROLLING CONTACT FATIGUE

Doctoral Dissertation of:
M. Gabriella TARANTINO
ID number. 738589

Supervisor:
Prof. Stefano BERETTA
Co-Supervisor:
Dr. Ioannis V. PAPADOPOULOS

Tutor:
Prof. Stefano BRUNI

The Chair of the Doctoral Program:
Prof. Giampiero MASTINU

2011 - XXIV Cycle

ἐὰν μὴ ἔπηλται ἀνέλπιστον,

οὐκ ἐξευρήσει, ἀνεξερεύνητον

ἐον και ἄπορον

Unless you expect the unexpected,
you will never find it, because it is
hard to be discovered and difficult to be attained

Heraclitus

Dedicated to Fabrizio and Michele

Acknowledgments

My best acknowledgments go to SKF Engineering& Research Centre, which has provided financial support to this research-project. I am deeply indebted Junbiao Lai and Mohamed Sherif for their precious help during my research visit at ERC.

Furthermore, I'd like to thank Dr. Stefano Foletti for his sharp but valuable spur.

List of publications

National Conferences*:*

- M.G.Tarantino, *Approccio multiassiale per la determinazione del coefficiente di intaglio a fatica*, XXXVIII Congresso nazionale AIAS, 9-11 Settembre 2009, Torino

- M.G.Tarantino, *Influenza dell'attrito e della rugosità sullo stato di sforzo all'apice della cricca sotto carichi affaticanti da fatica da contatto*, XXI Congresso nazionale IGF, 13-15 Giugno 2011, Cassino

International Conferences:

- M.G.Tarantino, I.V. Papadopoulos, S.Foletti, *A multiaxial approach for the determination of the fatigue strength reduction factor for V and U shaped notched specimens*, International Congress on Multiaxial Fatigue and Fracture, 8-10 Giugno 2010, Parma

- S.Beretta, S.Foletti, M.G.Tarantino,K.Valiulin *A novel experimental procedure to obtain stable mode III crack growth under RCF condition*, International Congress on Multiaxial Fatigue and Fracture, 8-10 Giugno 2010, Parma

- S.Beretta, S.Foletti, M.G.Tarantino, J.Lai *Competition between Mode I and Mode III under pure shear and RCF conditions*, 1st IJFatigue & FFems Joint Workshop, 7-9 Marzo 2011, Forni di Sopra

International Journals:

- S.Beretta, S.Foletti, M.G.Tarantino,K.Valiulin *A comparison of Mode II threshold under simple shear and RCF conditions*, Engineering Fracture mechanics, Vol. 78, Issue 8, 1742-1755, 2011

- S.Beretta, S.Foletti, M.G.Tarantino, J.Lai *Competition between Mode I and Mode III under pure shear and RCF conditions*, submetted for International Journal of fatigue

- M.G.Tarantino, I.V. Papadopoulos, S.Foletti, *A multiaxial approach for the determination of the fatigue strength reduction factor for V and U shaped notched specimens*, to be submitted International Journal of Fatigue

Tables of contents

List of figures

List of tables

List of symbols

A – deviatoric part of the shift tensor

a – crack length

b – notch depth

b_h – rate at with the yield surface size changes

C – initial kinematic hardening modulus

c – physical crack length

DEA – dark etched area

E – Young modulus

EDM – Electro-discharge maching

F – friction force

FE – finite element

FR – factory roof

k – local branch stress intensity factor

K – stress intensity factor

LEFM – linear elastic fracture mechanics

N – normal force

OOP – out of phase

p – local normal stresses

P – local opening force

q_f – local frictional stresses

Q – local shearing force

Q_∞ – maximum change of yield surface size

R – stress ratio

RCF – rolling contact fatigue

S – deviatoric stress tensor

SEM – scanning electron microscope

SIF – stress intensity factor

t – asperity height

UTS – ultimate stress

u – displacement of a point along the crack flank

WEA – white etched area

WF – weight function

ΔK_{III} – range of the nominal mode III stress intensity factor

$\Delta K_{th,I}$ – range of the nominal mode I stress intensity factor threshold

α – friction angle

$\boldsymbol{\alpha}$ – shift tensor

θ – asperity angle

φ – tilt angle

ψ – twist angle

θ – asperity angle

γ – rate of the kinematic hardening modulus

λ – asperity wavelength

ν – Poisson's ratio

μ – friction coefficient

r, φ, ψ – cylindrical coordinates

σ_y – yield stress

σ_0 – yield surface size

$\sigma|_0$ – initial value of the yield surface size

$\sqrt{}$area – crack size expressed in terms of square root of the projected crack area

Subscripts

eff – effective value of displacement or *K*

lc – long cracks

max – maximum value of *k* or *K*

pl – plastic

th – threshold

x- horizontal coordinate system used in FE analysis

y- vertical coordinate system used in FE analysis

I– mode I

Iw – displacement or *K* due to wedging

I0 – nominal displacement or *K* due to mode I

III – mode III

IIIf – displacement or *K* due to crack flank frictional stresses

III0 – nominal displacement or *K* due to mode III

Chapter 1
Introduction

1.1 Background and motivations

High-cycle contact fatigue failure has considerable industrial relevance in those applications where contact loads occur, e.g. in bearings, gears, cams, rail-wheel systems. The damage and failure of such components inevitably result in costly engineering loss and down-time.

Rolling contact fatigue (RCF) failures are cumulative damage phenomena: they are supposed to be caused by subsurface cracks which nucleate beneath the contact surface. The growth of subsurface RCF cracks is usually attributed to the cyclic shear stress component of the contact stresses. For this reason, the propagation is usually said to be "shear-dominated". Unlike the mode I growth (i.e. tensile-dominated growth) where the fatigue crack propagation involves a blunting and resharpening process at the crack tip, the mechanism of fatigue crack growth encouraged by shear occurs by cyclic shear displacements.

However, few similarities can be found between the growth of fatigue cracks under rolling contact and pure torsional loadings. When a component is subjected to rolling contact fatigue, the stress field experienced by the material is also characterized by the presence of compressive stresses. Figure 1.1 reports the tangential τ_{xz} and normal stress σ_z components due to the Hertzian contact. The coordinates x and z are taken in the direction of the tangent and normal to the contact surface, respectively. All the dimensions are normalized in respect to the half-width of the contact b. The stress components are instead normalized in respect to the maximum contact pressure p_0.

Compressive stresses in the material subsurface, are comparable in magnitude to the tangential stresses at the position along the contact where the latter component is maximum.

Under rolling contact fatigue, the fracture behaviour is governed by shear since the tendency to tensile growth is fully suppressed by the compressive stress, contrarily to what happens under pure torsional loading.

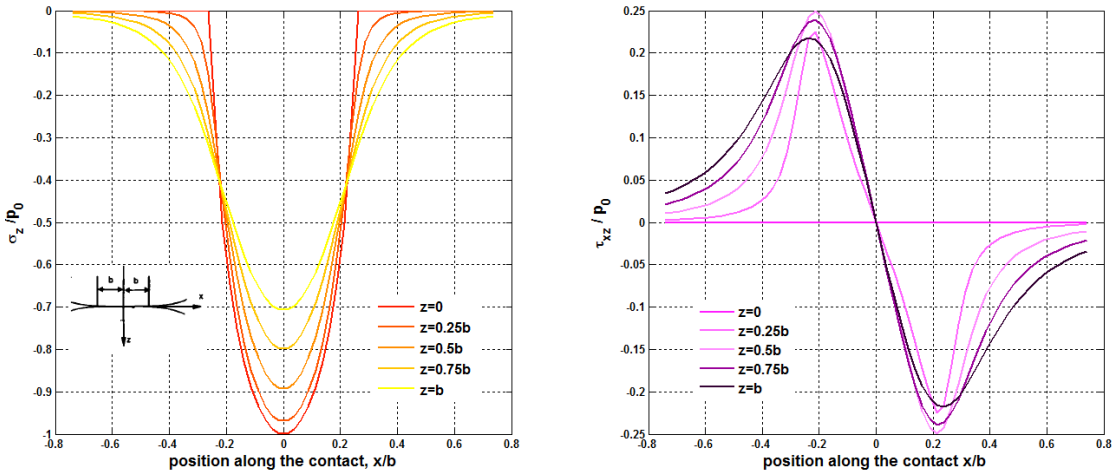

Figure 1.1. Components of stresses due to the Hertzian contact at various depths.

The shear-mode propagation mechanism under RCF is experimentally supported [1] by the macroscopic appearence of the fracture surfaces. A bearing steel "flaking-type" failure is shown in Figure 1.2: fracture pattern parallel to the contact surface can be easily observed.

According to Otsuka [1], the process of shear crack formation and propagation consist of two main stages: during the early stage fine shear cracks first nucleate parallel to the contact surface; subsequently the initial fine cracks grow into a macroscopic crack. The propagation is encouraged by two simultaneous mechanisms: the extension of the cracks themselves and the coalescence with the neighbouring cracks.

Otsuka and his co-workers also observed a different propagation behaviour between a brittle and a ductile material under rolling contact testing conditions. While in the early stage of damage no difference could be appreciated in the nucleation of the thin shear cracks, the process of crack growth appeared different: in hard materials the macroscopic crack was formed by linking the growing cracks in a direction normal to the contact surface; in soft metals, in stead, the initial cracks coalesced into a

macroscopic one. Consequently, RCF failures of brittle and ductile materials are commonly defined as “spalling-type” and “flaking- type” respectively.

A schematic illustration of the aforementioned mechanism of fatigue crack initiation and growth under RCF is shown in Figure 1.3.

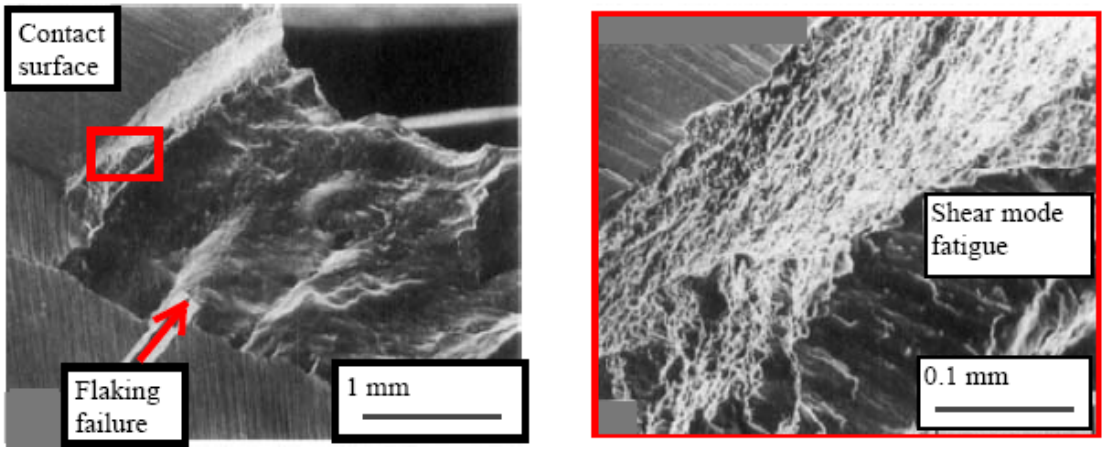

Figure 1.2. Flaking failure in rolling contact fatigue of a bearing steel: macroscopic and higher magnification view of the fracture. After Otsuka et al [1].

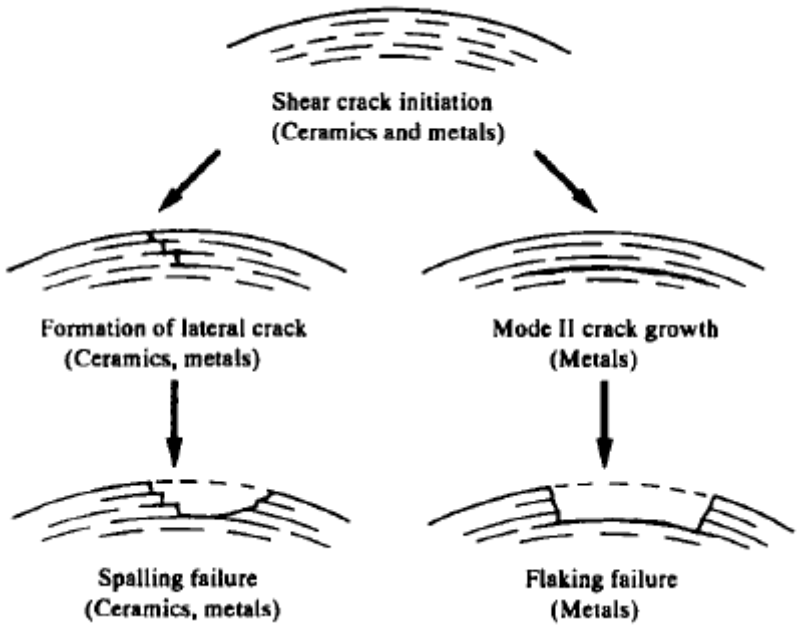

Figure 1.3. Mechanism of fatigue crack growth under rolling contact fatigue for brittle and ductile materials. After Otsuka et al [1].

Although the work of Otsuka et al [1]-[2] highlighted the main aspects concerning the shear mode propagation of fatigue cracks under rolling contact loadings, the growing cracks are quite often nucleated from small defects. Literature provides famous examples of crack initiation induced by the presence of micro-defects: the internal defects in the material may act as stress raisers encouraging the initiation of the surface or subsurface fatigue crack. In the work of Beretta et al [3], the origin of the fracture surface was found to be a cluster of Al_2O_3 inclusions aligned to the rolling direction. The fracture surface of the real railway wheel is shown in Figure 1.4. The final fracture appearance is regarded as the result of a complex propagation mechanism: the crack first propagated both parallel and perpendicular to the rolling direction and eventually became a circular shape (phase I); subsequently it grew by mode II and mode III (phase II). The first stage of the crack growth is proposed to be promoted by mode I under the residual tensile stresses produced by the cyclic compressive load.

Micro-structural changes may also occur in the proximity of the spots, Vincent et al [4] reported evidence of peculiar metallurgical transformations of the material around the defect zone: a wings-like emanation from the aluminium oxide inclusion was observed. Because of the shape, it was called *butterfly*. After etching in a nital acid solution, the butterfly wings appeared white in contrast with the surrounding matrix and oriented at 45 degrees with respect to the rolling contact surfaces, see Figure 1.4.

Owing to the fact that crack initiation is usually induced by the presence of micro-defects, the fatigue process under RCF should, therefore, be described in terms of shear propagation/threshold [5]-[6], as is the case with simple mode I where fatigue strength is controlled by the threshold condition of small crack which nucleate from micro-defects [7].

According to their dimensions cracks can be classified as [8]:

- *large*: large cracks have fracture dimensions that are large compared to the scale of microstructure in both directions;
- *short*: short cracks are physically short only in one dimension since their front is much longer than the characteristic microstructural length;

– *small*: small cracks are small and comparable to the microstructural size scale in all dimensions.

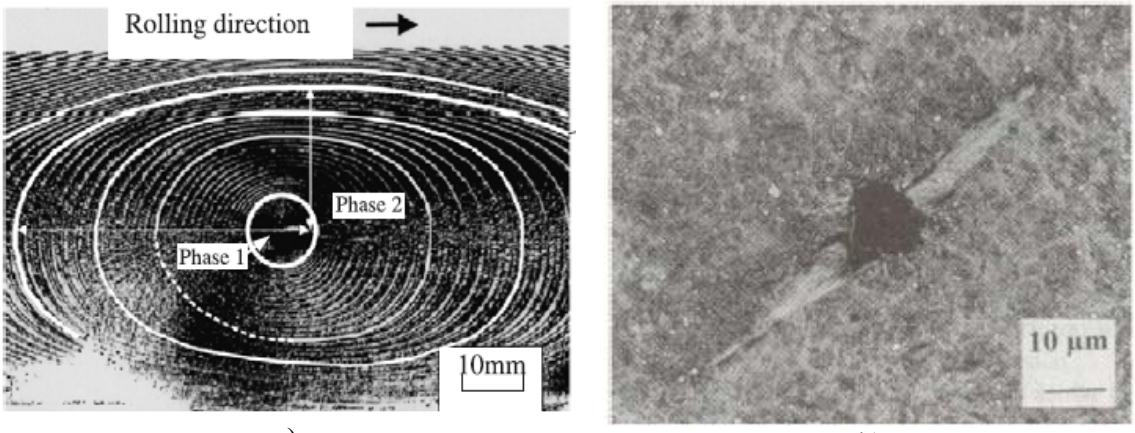

a) b)

Figure 1.4. Crack initiation induced by the presence of micro-defect: a) crack growth pattern of an elliptical crack in a real railway wheel [3]; b) optical micrograph of a butterfly around an aluminium oxide inclusion [4].

The length of the physical crack strongly influences the near-threshold behaviour: the fatigue threshold of small and short cracks is significantly smaller than the threshold measured for long cracks. The "short crack effect" has been extensively documented by literature under nominal mode I loading [9]. In the experimental study of Christman et al [10] concerning fatigue assessments of a SA542 Class 3 steel, the closure phenomenon at the crack tip was proposed to be the leading factor which contributes to a faster growth of the physically short cracks. Mode I growth rates were found to significantly decrease as the growing fatigue cracks had propagated over a small fraction of a mm due to the induced noticeable level of crack closure.

A short crack effect under mixed loadings is also reported by Campbell at al [8]: they investigated the threshold behaviour under combined mode I+II loadings in a Ti6Al4V alloy with a typical turbine blade microstructure. Again the crack tip shielding was proposed to be the prominent mechanism governing fatigue crack propagation because of the reduced extent of closure phenomena at the crack tip: small and short cracks have at their disposal a local driving force higher than the one available to large cracks at the same applied load level.

However compared to the large volume of information on competitive failure mechanisms under rolling contact fatigue [11]-[12], studies focused on crack growth behaviour of short cracks encouraged by shear under RCF are comparatively rare in literature. Additionally laboratory scale experiments for cracks growth under mixed loadings, simulating rolling contact fatigue conditions, are much more difficult than fatigue experimental studies under mode I testing conditions.

A crack size effect, influencing the near threshold behaviour of short semi-elliptical cracks (less than 1 mm in size) propagating by shear, is reported by Matsunaga et al [13]. In the mentioned study, experiments on micro-notched martensitic bearing steel samples were carried out in order to obtain stable shear mode crack growth. At this scope, a static compression was superimposed on the cyclic torsional loading in order to suppress the tendency for mode I branching.

Nevertheless, until now, only "experimentally" derived shear growth data on small defects have been incorporated into RCF models for subsurface fatigue ([4],[14]) under the implicit assumption that the growth rate under RCF conditions can be obtained by combining the experimental trend (threshold, growth rate) under pure mode II/mode III together with SIF calculations under the out- of-phase combination of mode I + mode II/mode III (see the discussion by Murakami [15] on a 'shelling' railway failure).

In the present thesis an attempt is done to overcome the lack of experimental data on crack growth rates and thresholds of short fatigue cracks propagated by shear under mixed loadings simulating RCF testing conditions: at this purpose the application of a novel experimental methodology, previously developed by Beretta et al. [16], has been extended onto a bearing and a railway steels in order to promote mode III co-planar crack propagation under rolling contact loads. Besides the consolidation of the new testing procedure, in the present study an attempt is also done to sufficiently clear up the mechanism governing the propagation of short cracks under contact stresses, thereby providing a plausible explanation which could support the crack growth behaviour observed experimentally.

In what follows a briefly literary survey of the past works on fatigue crack propagation under combined torsional and axial loadings will be presented and the

fundamental aspects of the fracture mechanism under anti-plane shear will be outlined. Finally the scope and the objectives of the thesis will be clarified.

1.2 Fatigue crack propagation under combined torsional and axial loadings: literary review

Literature provides a considerable number of works devoted to mixed mode fracture in both brittle and ductile materials. Besides rolling contact fatigue failures such as "flaking" in bearings and "shelling" in rails, turbo-generator shaft failures are also shear-dominated fractures. Turbine rotor shafts undergo complex varying stresses: torsional overloads due to electrical faults and alternating mode I loading due to self-weight bending. The importance of mixed loading condition on fatigue crack growth in rotating shaft is stated in [17].

The mixed mode fracture tests under combined torsional and axial loading are commonly carried out using circumferentially notched specimens bars [18]-[21]; a schematic diagram of the specimen is given in Figure 1.5.

The mode III crack propagation behaviour is principally examined as the radially inward concentric cracking at the notched bar. In order to promote the coplanar propagation, a pre-crack is usually introduced by push-pull cycles before starting the test. In the work of Yates et all [22], a 5 mm deep circumferential slit was in stead introduced by electric discharged machined in order to eliminate fracture surface rubbing.

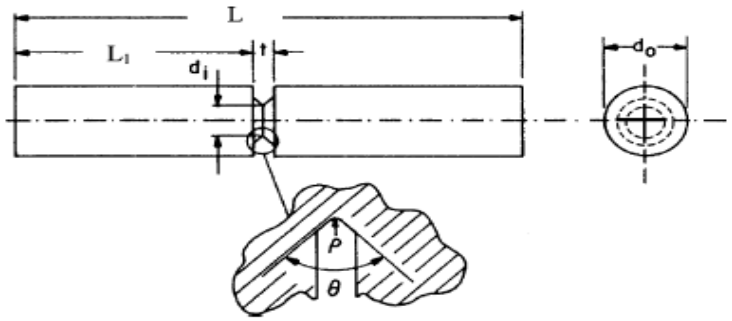

Figure 1.5. Mixed mode I/III fracture specimen [18].

However, although simple in geometry the circumferentially notched specimen is extremely prone to misalignment problems. In order to avoid undesidered bending moment, which causes asymmetric crack growth, Ritchie et al [21] adopted a special designed torsional Wood's metal grips.

All the experimental works under combined torsional and axial loading, directed to understand the conditions governing the onset of mode III fatigue crack growth, revealed a complex crack path morphology of the fracture surfaces depending on the testing conditions.

The macroscopic appearance of crack surfaces of ductile materials [18],[20]-[23] was found to be determined by the cracking mode dominating the competition between tensile and shear fractures. A transition from a completely flat to a faceted surface was revealed after the optical and scanning electron observations of fractographs. The non-flat surface is commonly called by literature "*factory roof*" and it appears to be dominated by mode I, see Figure 1.6; while the flat surface is dominated by shear because of the evidence of rubbing marks.

On the other hand, the fracture behaviour of brittle materials [18]-[19] was found to be solely due to a tensile failure mechanism: the fracture surface morphology of brittle materials was characterised by radial three-dimensional microstructures regularly shaped around the crack front.

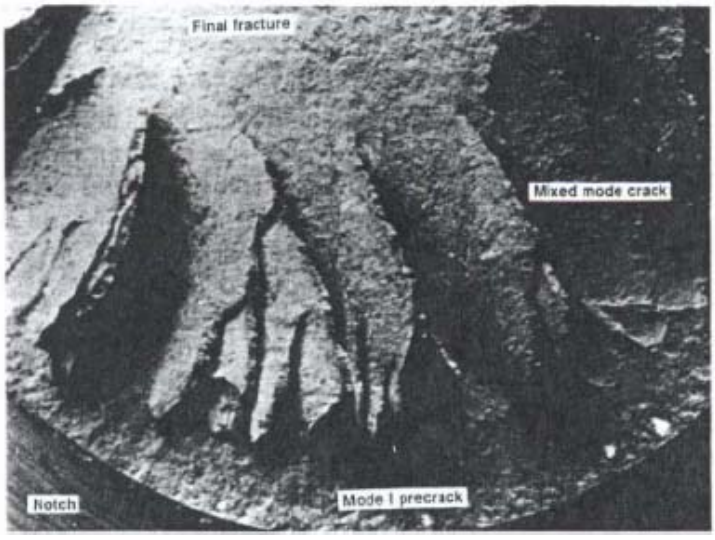

Figure 1.6. Mechanism of factory roof under mixed loadings. After Tong et al [23].

Furthermore, the fracture behaviour strongly depends on the loading mixity as well as on the fatigue stress ratio. The influence of the ratio R on the fracture morphology was investigated by Tong et al [23] through in-phase fatigue tests on a 3.5 % NiCrMoV steel.

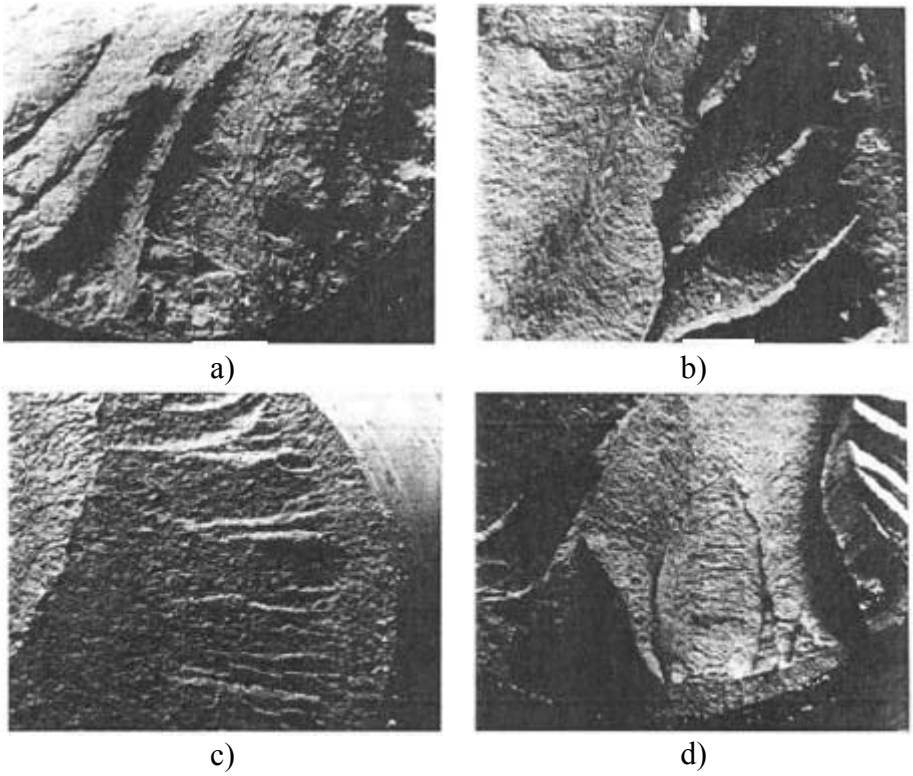

Figure 1.7. Appearence of the fracture surfaces at different R ratios and loading mixities: a) R=-1 and $\Delta K_I/ \Delta K_{III}=1$; b) R=0.1 and $\Delta K_I/ \Delta K_{III}=1$; c) R=-1 and $\Delta K_I/ \Delta K_{III}=0.5$; d) R=0.1 and $\Delta K_I/ \Delta K_{III}=0.5$. After Tong et al [23].

At negative R ratios, dissipative phenomena engendered by cyclic tangential displacements are responsible for a flat fracture surface appearance, see Figure 1.7.

When a component is subjected to torsional loading, the crack surfaces are relatively displaced over each other and fretting phenomena, involving severe abrasion and oxide formation, occur between the mating fracture surfaces. It is also reported [24] that the specimens were observed to become hot to touch during testing with wear-like debris emerging from the crack opening.

The effect of friction is somewhat relevant since the interaction between the sliding crack faces causes a reduction of the effective stress intensity factor experienced by

the crack tip. A schematic illustration of the mechanism of surface interference involving rubbing and interlocking between asperities is depicted in Figure 1.8.

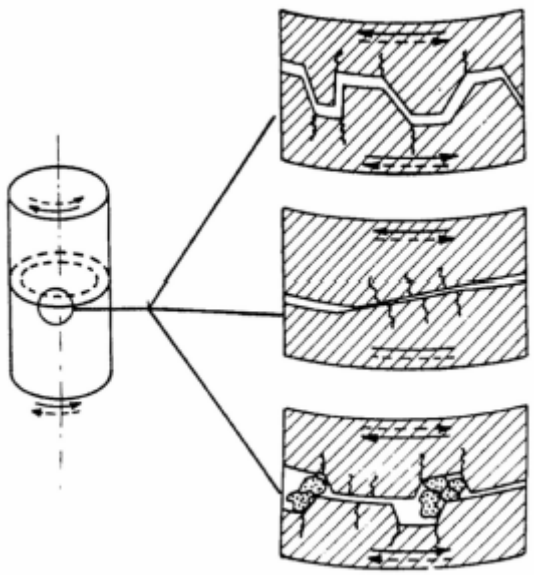

Figure 1.8. Crack surface interference under cyclic torsional loading: a) schematic illustration of the mechanisms of surface interference. After Ritchie et al [21].

Ritchie [21], Nayeb-Hashemi [24], Tschegg [25] and their co-workers examined the role of friction on fatigue crack propagation promoted by shear by superimposing a static tensile loading to the applied alternating torque. Whenever the combination of the superimposed mode I loading and extensive plasticity allow the crack to remain open for the majority of the loading cycle, less abrasion and little evidence of fretting oxide formation were observed.

1.3 Mechanisms governing the fracture behaviour under anti-plane shear

Although extensively confirmed experimentally ([20]-[23],[25]), the competition between tensile and shear failure mechanism characterizing the macroscopic fracture appearance under mixed I/III loading has not been exhaustively discussed.

Very few past works were directed to provide physical explanation for the mechanism governing fatigue crack propagation encouraged by shear [26].

Nayeb-Hashemi et al [24] developed a micro-mechanical model for shear crack advance under pure anti-plane loading: the crack extension was proposed to occur via mode II coalescence of microcracks initiated at inclusions in the immediate vicinity of, and parallel to, the mode III crack front. This modelling analysis was supported by the observations of fractographs (Figure 1.9) where elongated voids, parallel to the crack front, are shown.

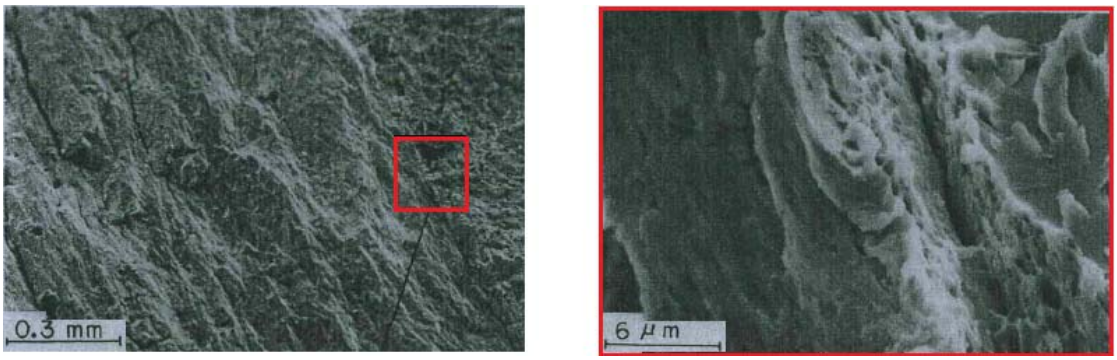

Figure 1.9. Micromechanical modelling of crack propagation under anti-plane shear showing elongated voids formed parallel to the crack front. After Nayeb-Hashemi et al [24].

However, the most peculiar macroscopic appearance of mode III fracture surfaces is the "factory roof". The mechanism governing the FR formation has been recently investigated by different authors [27]-[28]. It was found that prior to the formation of factory roof, many semi-elliptical cracks are nucleated at the initial circumferential crack tip under anti-plane shear. After sectioning and polishing [27], the "factory roof" profile also appeared to be characterized by a number of crack branches (increasing as more of the surface layer is removed). The branching angles were found to be larger than ± 45° and rather close to ± 70.5°, where the former angles correspond to the direction of remote maximum principal stress, the latter to the direction of the local maximum tangential stress. A schematic illustration of the factory roof formation mechanism and the crack braches, after sectioning and polishing, are shown in Figure 1.10.

Pokluda et al [28] extended the knowledge of the factory roof formation mechanism providing physically based relationships developed with the purpose of predicting the initiation and growth of the FR morphology.

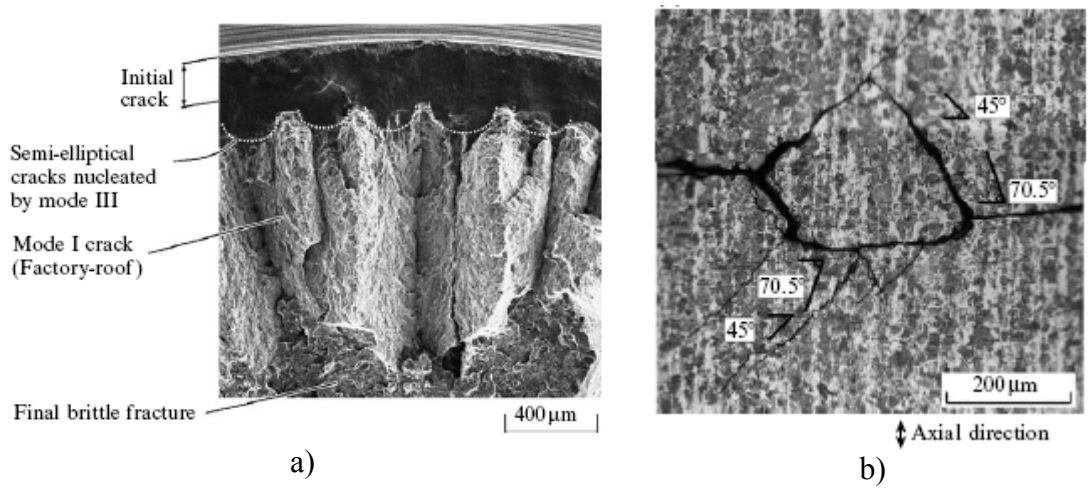

Figure 1.10. Mechanism of "factory roof" formation: a) schematic illustration; b) crack branches after sectioning and polishing. After Murakami et al [27].

In agreement with the discussion by Murakami [27], the theoretical modelling analysis of Pokluda and his co-workers first confirmed the "factory roof" initiation from elementary mode I branches developed along the front of the semi-elliptical surface cracks, which in turn were nucleated at the circumferential crack tip. Additionally, the most probable sites of the mode I branching were also predicted. The framework of the theoretical analysis was a complex mathematical procedure directed to find the twisting and tilting angles (X and Θ respectively, see Figure 1.11) associated with a branch of a maximal local mode I stress intensity factor. All the positions along the semi-elliptical crack front, defined by the polar angle φ, were explored and the synergy effect of both mode II and mode III loading on the creation of the mode I branch was also considered.

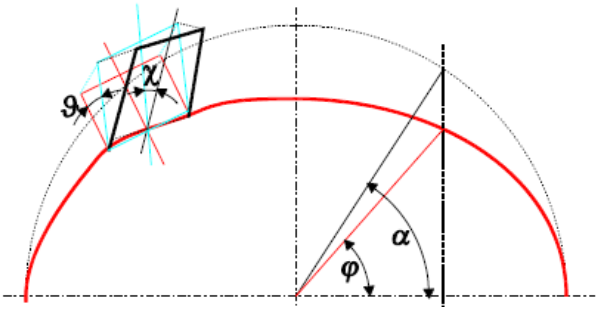

Figure 1.11. Scheme of the branched element. After Pokluda et al [28].

According to the theoretical analysis of Pokluda and his co-workers, two segments on the semi-elliptic crack front were proposed to be the probable loci for the initiation of the "factory roof" nuclei. A good correspondence between the theoretical predictions and the real position of the FR nuclei was found, see Figure 1.12.

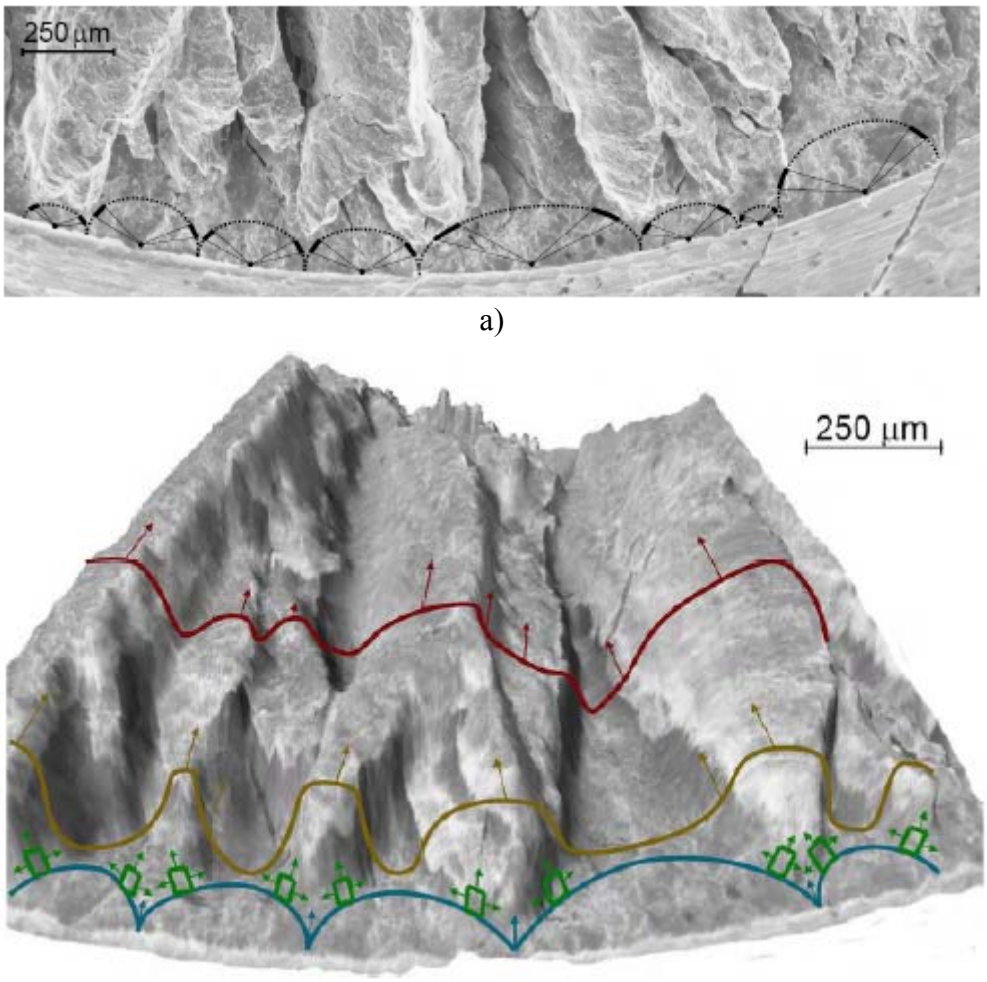

a)

b)

Figure 1.12. Creation and further propagation of FR nuclei: a) correspondence between the predicted position of the mode I branch at the semi-elliptical crack front and the real position of the FR nuclei; b) 3D image of the "factory roof" formation.

The kinetics of the "factory roof" formation (see a 3D image in Figure 1.12) was also qualitatively assessed [28] and three principal stages were distinguished:

– 1st stage: the formation of the complex FR morphology started with the creation of mode I branches at defined sites along the semi-elliptical cracks

nucleated at the circumferential crack tip. Mode I branches appeared first on the larger semi-ellipses. At the end of this stage, the initial FR crack front consisted of local spatial ledges and branches which formed the embryonic massifs connected by the remaining crack front of the semi-elliptical cracks;

- 2nd stage: during this stage the embryonic massifs expanded in both the radial (inside the specimen bulk) and the tangential (along the semi-elliptical crack front) directions. Both the height and the width of the nuclei increased while forming a U-shaped valley of a decreasing width. At the end of this stage, the main lamellar structure, similar to a "lance", was formed;
- 3rd stage: during this final stage the FR resembled a saw-tooth profile. It propagateds further in the radial direction. Because of geometrical reasons, the width of the "factory roof" front decreased while approaching the centre of the sample. Consequently the massifs appeared mutually closer and their heights and widths decreased. The FR patterns gradually extinguished in conjunction with the final fracture of the sample.

1.4 Dissertation outlines

The aim of the present thesis is to exhaustively clear up the mechanism governing the shear-mode propagation of short fatigue cracks under mixed loadings simulating subsurface rolling contact fatigue conditions.

The dissertation outlines can be highlighted through the attempts directed to answer to the following "challenging" questions:

- Is there a "short crack effect" on the near-threshold behaviour under RCF?
- Is it possible to correlate crack growth data under rolling contact loadings with the experimental trend under simple shear?
- Can the stress field at the crack tip be characterized on the basis of the external loading only?
- Which is the role played by the far-field compression on the crack growth behaviour under RCF?

In order to answer to the first question, a novel experimental test procedure has been consolidated onto a bearing and a railway steels. Mode III crack growth rates and thresholds, obtained under rolling contact testing conditions, have been obtained by adopting a novel experimental methodology first developed by Beretta et al [16].
On the other hand, the co-planar crack growth data obtained under rolling contact loading have been compared with the experimental trend under simple shear in order to verify whether the experimentally derived shear growth data on small defects can be easily incorporated into RCF models for subsurface fatigue without making any errors.
Furthermore, for crack propagation under both rolling contact and pure torsional loadings, co-planar mode III crack propagation rates have been related to the effective mode III stress intensity range in order to provide a unique description of mode III crack propagation behaviour over the above testing conditions. Accordingly, when the effective mode III SIF is used to describe the co-planar crack growth, frictional dissipative phenomena due to rubbing and interlocking between sliding crack surfaces are taken into account. At this scope, a partial slip analytical model was developed to quantify the effect of crack face friction under both simple shear and rolling contact loads.
During the crack flanks sliding interaction the surface irregularities, characterizing the crack profile on a microscopic size scale, are wedge open. The dilatancy effect, introducing a mode I wedging stress intensity factor, together with the frictional dissipation of the applied mode III SIF can significantly affect the stress field actually experienced at the crack tip. A micro-mechanical model, where the mentioned effects engendered by crack flanks sliding interaction were taken into account through the coupling between mode I and mode III displacements, has been developed with the aim of correctly characterizing the local mode mixity at the crack tip.
Finally, in order to answer to the last question about the role played by the far-field cyclic compression, whether it acts alone or superimposed to the alternating torsion, elastic-plastic finite element analyses with crack advance have been conducted.
Within this framework the dissertation is organized as follows:

- in *chapter 2* the novel experimental methodology, directed to promote mode III coplanar crack propagation, is described. Fatigue test results, on micro-notched hourglass samples subjected to an out-of-phase loading pattern simulating conditions typical of sub-surface RCF in bearings, are presented and the crack size dependency on the threshold value is investigated;
- in *chapter 3* the bearing steel co-planar crack growth data obtained under rolling contact loadings are compared with the experimental trend under simple shear. The effect of crack face friction is also examined and the mode III effective thresholds under both simple shear and rolling contact fatigue testing conditions are thereby compared;
- in *chapter 4* a micro-mechanical cyclic analytical model is developed to quantify the effects of the interaction engendered by the sliding contact between the rough crack surfaces. The model, developed under a general mixed I+III testing condition, can be also readily applied under pure mode III loading;
- in *chapter 5* the leading mechanism governing the macroscopic fracture behaviour under mixed loadings is investigated and the competition between tensile and shear failures is examined by the exploitation of the micro-mechanical model developed in chapter 4. The conditions governing the onset of mode I/mode III crack branching are examined on the basis the effective stress field actually experienced by the material at the crack tip;
- in *chapter 6* the role played by the far-field cyclic compression on fatigue crack propagation encouraged by shear under rolling contact loads is investigated. The influence of the compressive stress, when it acts alone, is first examined experimentally. Elastic-plastic finite element analyses with crack advance are also conducted in order to support the experimental findings under both pure compressive and rolling contact testing conditions.

Conclusions and recommendations for future works are listed in *chapter 7*.

Chapter 2

Fatigue crack growth assessments under rolling contact fatigue conditions

2.1 Introduction

This chapter is devoted to the assessments on fatigue crack growth and near-threshold behaviour of short semi-elliptical cracks under rolling contact loadings. The crack growth curves have been obtained after testing cylindrical micro-notched specimens under an out-of-phase load path simulating sub-surface RCF stress conditions. The tests were carried out in ambient air. Various sizes of artificial defects have been introduced onto the hourglass specimens in order to investigate the crack size dependency on the threshold values. Moreover, the experimental tests have been specifically directed to mode III fatigue assessments: it has been demonstrated [13] that the shape of non-propagating cracks in smooth specimen is strongly influenced by elongated inclusions and the near-threshold behaviour of such shallow cracks is predominantly prejudiced by the threshold condition for growth in the internal direction rather than along the surface. Mode III SIF is, in fact, much higher than mode II SIF near the surface.

The test methodology adopted in the current study was previously developed and applied onto a gear steel material by Beretta et al [16]. In the present chapter, the novel experimental methodology has been extended and consolidated onto a bearing steel material. A part of the experimental data on the bearing steel has been reported in [29] and [30].

Furthermore, the fatigue propagation behaviour encouraged by shear under RCF conditions has also been investigated onto a ductile railway steel. Fatigue crack growth data for the railway steel are reported in *Appendix A*. In what follow the experimental test procedure is described and the fatigue test results are presented.

Finally, the co-planar crack fracture surfaces have been metallurgically investigated after etching in nital solution and the effect of crack surface interference has also been examined after the optical and scanning electron microscope observations of the mode III fractographs. Chemical analyses were also carried out to support the experimental findings revealed by SEM.

2.2 Experimental details

2.2.1 Material

The material analyzed is bainitic bearing steel. The Vickers micro-hardness value measurement (load 0.98 N) and the monotonic and cyclic mechanical properties are reported in Table 2.1. The material showed a strain hardening behaviour when subjected to cyclic loading.

	E [MPa]	**HV**	**UTS [MPa]**	**σ_y [MPa]**	**$\sigma_{y,\ cyclic\ 0.2\%}$[MPa]**
Bearing steel	204355	690	2364	1982	2072

Table 2.1 Material mechanical properties.

2.2.2 Specimens

All fatigue tests were carried out on pre-cracked micro-notched hourglass specimens. Three defects sizes, expressed in terms of Murakami's √area parameter, equal to 630 μm, 315 μm and 220 μm were considered. The geometry of the specimens and the micro-notches adopted are presented in Figure 2.1. Before starting fatigue tests all specimens were electro polished to avoid the effect of the surface residual stresses. Artificial micro-notches were then introduced by means of electro-discharging machining (EDM). In order to promote coplanar crack propagation, a preliminary mode I fatigue test pre-cracking procedure was adopted. All specimens were subjected to push-pull axial fatigue for 10^7 cycles with a stress ratio R= -1 at a stress level close

to the range of the mode I stress intensity factor fatigue threshold ΔK_{Ith}. An addition compression pre-cracking was applied to the specimen in order to obtain non-propagating cracks going out from the micro-notch on the surface. Further details on mode I fatigue assessments for the bearing steel are reported in [29]. The pre-cracking procedure induced small non-propagating fatigue cracks with a depth of approximately 20 μm, see Figure 2.1.

All specimens were observed under SEM to verify the success of the pre-cracking procedure, if not successful the mode I pre-cracking was repeated.

2.2.3 Fatigue tests

After the pre-cracking procedure, the specimens were subjected to multiaxial fatigue tests. The main idea of the experimental procedure was to run fatigue tests by decreasing the load from one specimen to another until no fatigue crack growth occurs. During the fatigue tests an optical microscope Leica system permitted to control the surface-mixed mode crack advance continuously during the test.

Multiaxial fatigue tests were conducted in force/torque control by means of an MTS 809 Axial Torsional System. Fatigue tests were carried out at a frequency of 2 Hz adopting a torsion/push-pull sequence under load control, simulating conditions of sub-surface RCF in bearings , with axial force always in compression and shifted 90° relatively to the torsional cycle. The load pattern was supplied by SKF and loaded point by point into the test rig controlling software.

An example of the load pattern used for multiaxial fatigue tests is shown in Figure 2.2 in terms of stress intensity factors for a shallow pre-cracked micro-notch of √area = 220 μm under $\Delta K_{III}/ \Delta K_{Ith} \approx 1$.

The multiaxial fatigue tests were interrupted on the basis of the maximum surface crack length measurements $a_s \leq 1$ mm or otherwise, according to the number of fatigue cycle ($N = 2 \times 10^6$), if the near-threshold crack propagation behaviour was of interest.

Following the fatigue test, all the specimens were subjected to intense ultrasonic cleaning in acetone in order to remove the debris clopping the defect. After this procedure had been completed, all the specimens were examined under SEM. Both the

specimen surface appearance (aspect of crack mouth, length of crack emerging on the surface) and the co-planar fracture surface morphology were examined. The latter was investigated after static cryogenic rupture in liquid hydrogen.

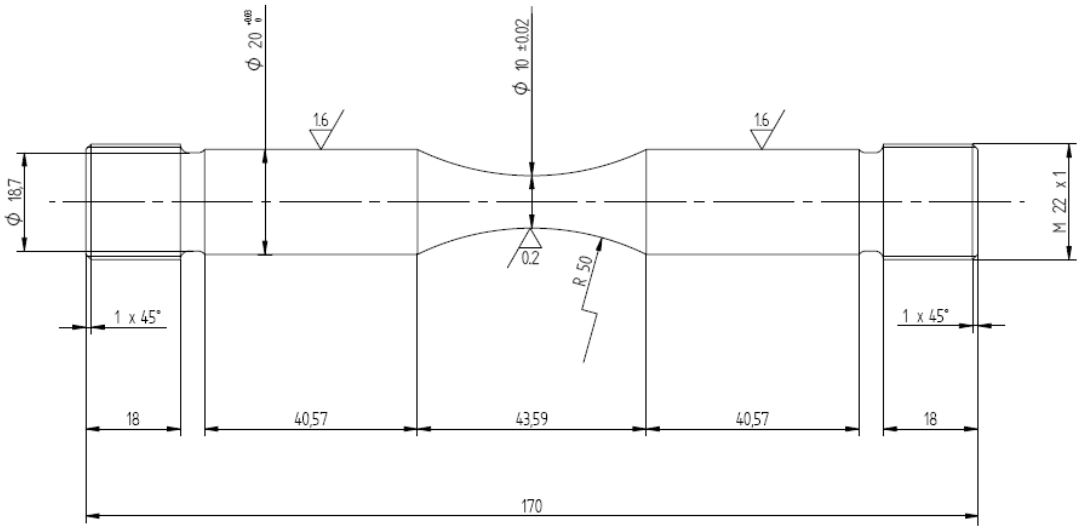

a)

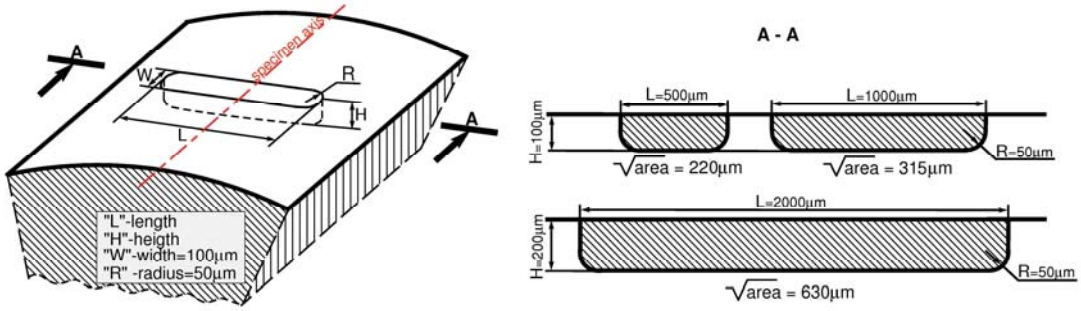

b)

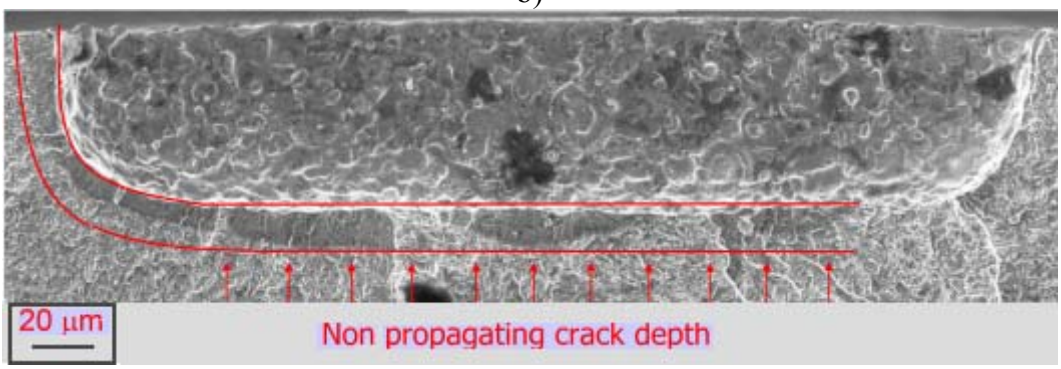

c)

Figure 2.1. Fatigue tests: a) specimen geometry for multiaxial fatigue test; b) artificial micro-notches shape and dimensions; mode I pre-cracking onto a micro-notched specimen (√area=220 µm) broken under liquid hydrogen.

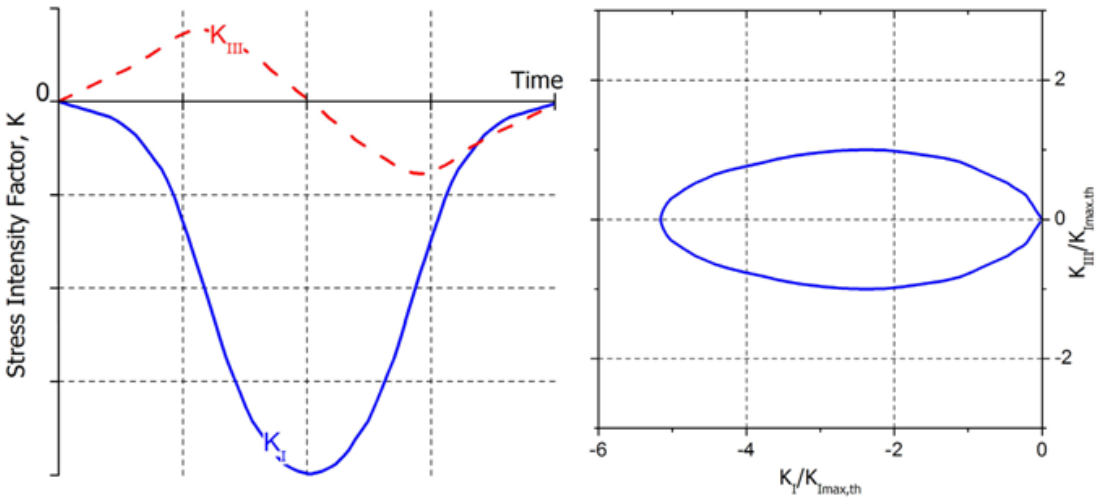

Figure 2.2. Load pattern scheme adopted for out-of-phase fatigue tests.

2.3 Fatigue tests results

Due to the out-of-phase load pattern, a complex crack propagation behaviour has been observed. Following an examination of the specimens fractographies, it appears clear that the out-of phase loading scheme promotes mode III co-planar crack growth, owing to the fact that it was possible to obtain continuous mode III propagation at much lower ΔK_{III} levels than mode I threshold, and thus inhibit the development of mode I kinked cracks (see Figure 2.3).

In particular it can be remarked that in tests where $\Delta K_{III} < \Delta K_{Ith}$ no appreciable surface crack growth is observed, while in all the test at $\Delta K_{III} > \Delta K_{Ith}$, the development of mode I tilted cracks along the crack front is noted, see Figure 2.4. The current test results fully confirm previous results obtained by Beretta et al. [16] onto a gear steel.

A possible reason for this 'promotion of shear growth' and co-planar growth stability is the evidence of huge plastic deformation and rubbing of fracture lips. As it can be seen in Figure 2.5, following out of phase fatigue test, the crack remains widely open as opposed to its state after pre-cracking.

During fatigue tests, the emission of debris emerging from the crack was also noted. The presence of debris has to be attributed to the abrasion process engendered by the interaction of the sliding rough crack surfaces during anti-plane shear. Matsunaga [13] also reported evidence of debris emission during fatigue tests on a commercial grade

SAE 52100 bearing steel (the load path consisted of a fully-reversed torsion with a superimposed static axial compression and the compressive stress was applied parallel to the fatigue crack). According to Matsunaga the presence of debris also indicated that the crack growth threshold had been increased by the interference of crack faces.

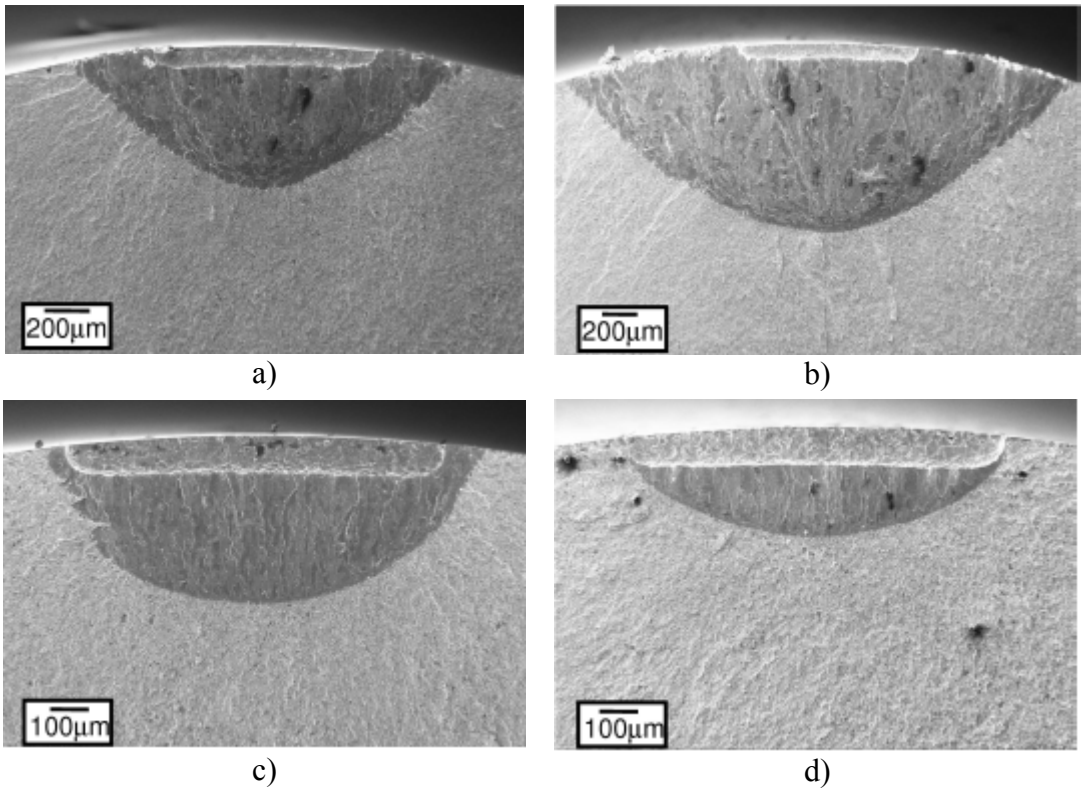

Figure 2.3. Mode III fracture surfaces for micro-notches of √area = 315 µm specimen tested at: a) $\Delta K_{III}/\Delta K_{Ith}$ = 1.3 for N = $2.5 \cdot 10^4$ cycles; b) $\Delta K_{III}/\Delta K_{Ith}$ = 1.1 for N = 10^5 cycles; c) $\Delta K_{III}/\Delta K_{Ith}$ = 0.87 for N = 10^4 cycles; d) $\Delta K_{III}/\Delta K_{Ith}$ = 0.7 for N = $1.2 \cdot 10^5$ cycles.

Fatigue tests were conducted until the threshold condition was achieved. However, although a working definition of mode I fatigue threshold has been generally accepted, a consistent definition of fatigue threshold values for other modes of cracking do no exist. Tschegg [26] interpreted as “mode III fatigue threshold” the lowest stress intensity factor range at which the macroscopic appearance of the fracture surface was characterized by a flat surface. Hellier et al. [31] similarly defined the mode III threshold as the applied SIF at which a transition from a completely flat to a faceted fracture surface occurred. In the current study, the

threshold condition has been defined by the nominal mode III stress intensity range at which a discontinuous or absent co-planar propagation is observed, see Figure 2.6.

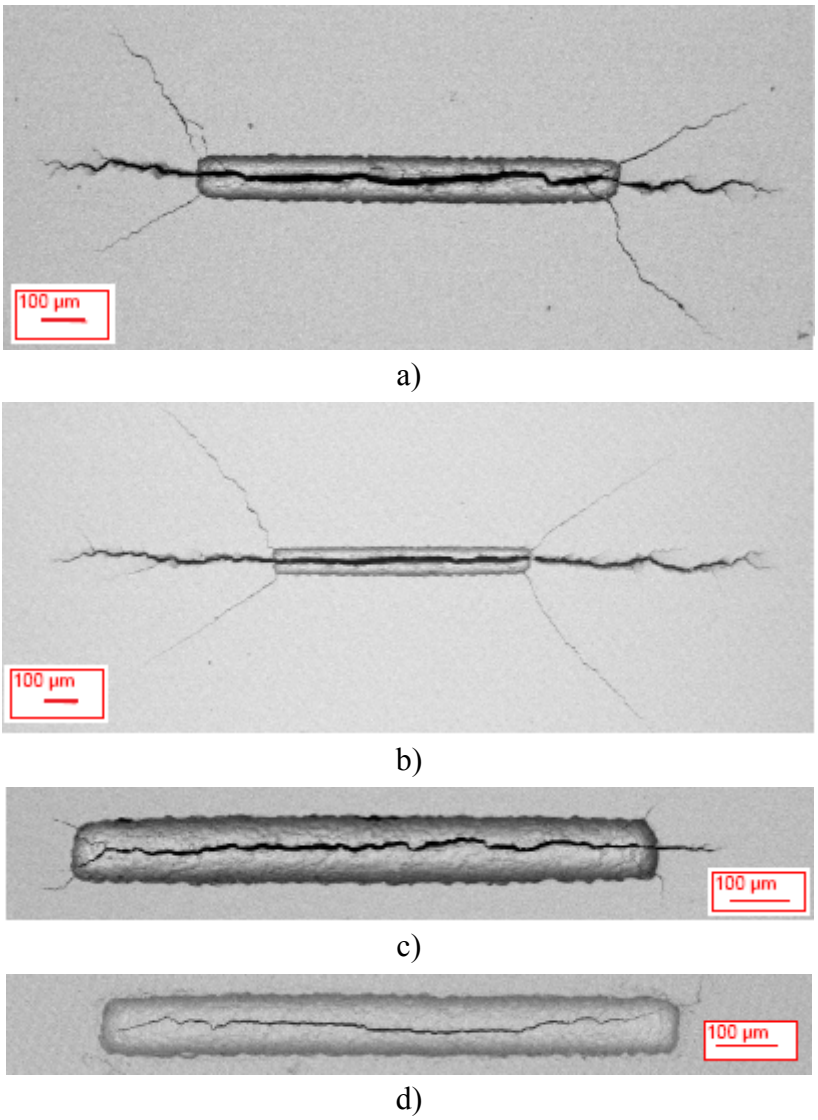

Figure 2.4. Specimen surfaces for micro-notches of √area = 315 µm specimen tested at: a) $\Delta K_{III}/\Delta K_{Ith}$ = 1.3 for N = $2.5 \cdot 10^4$ cycles; b) $\Delta K_{III}/\Delta K_{Ith}$ = 1.1 for N = 10^5 cycles; c) $\Delta K_{III}/\Delta K_{Ith}$ = 0.87 for N = 10^4 cycles; d) $\Delta K_{III}/\Delta K_{Ith}$ = 0.7 for N = $1.2 \cdot 10^5$ cycles.

The mode III crack growth rates are reported in Figure 2.7, together with thresholds values under pure torsional loading. The crack growth and near-threshold behaviour of the bearing steel under pure anti-plane shear is investigated in [29] and [30]. Fatigue crack growth data $\Delta a/\Delta N$, expressed in terms of nominal mode III stress intensity factor range ΔK_{III}, are presented in a normalised form, with ΔK_{III} normalised with

respect to mode I threshold for long cracks $\Delta K_{Ith,LC}$. The range of the threshold stress intensity factor for short crack is related to the range of the threshold stress intensity factor for long cracks [32].

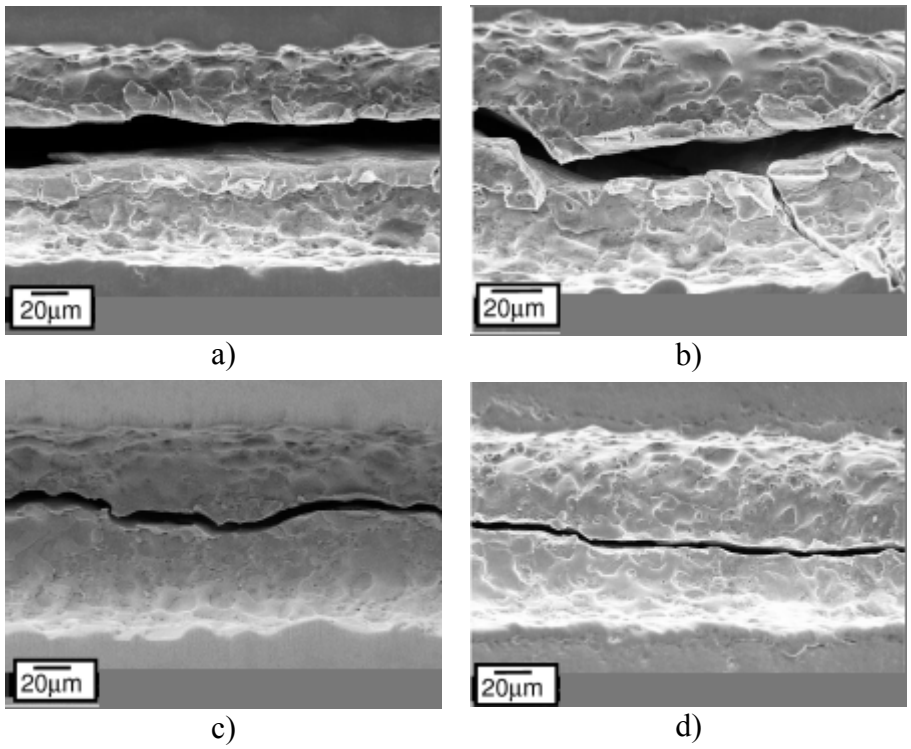

Figure 2.5. Evidence of crack lips opening for micro-notches of √area = 315 µm specimen tested at: a) $\Delta K_{III}/\Delta K_{Ith} = 1.3$ for $N = 2.5 \cdot 10^4$ cycles; b) $\Delta K_{III}/\Delta K_{Ith} = 1.1$ for $N = 10^5$ cycles; c) $\Delta K_{III}/\Delta K_{Ith} = 0.87$ for $N = 10^4$ cycles; d) $\Delta K_{III}/\Delta K_{Ith} = 0.7$ for $N = 1.2 \cdot 10^5$ cycles.

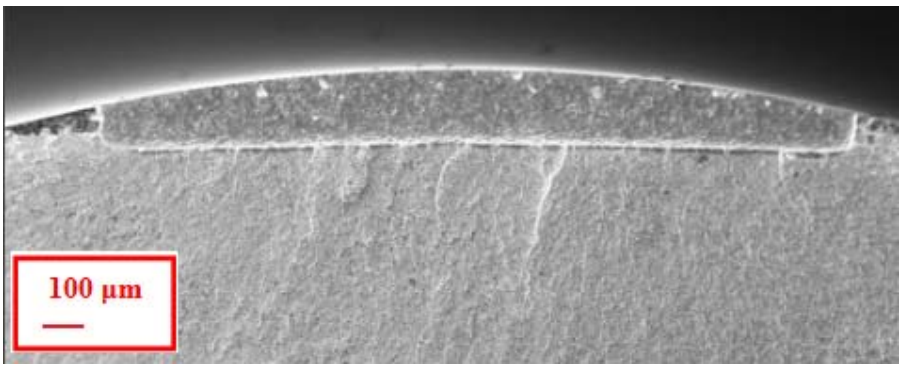

Figure 2.6. Absent co-planar propagation onto a micro-notched specimen (√area = 630 µm) tested at $\Delta K_{III}/\Delta K_{Ith} = 0.5$ for $N = 4 \cdot 10^5$ cycles.

The mode III crack growth rates $\Delta a/\Delta N$ have been calculated after the specimens breaking under liquid hydrogen. On account of the fact that the SIF at the deepest

point of the crack remains constant although the change of the aspect ratio during the crack propagation [16], $\Delta a/\Delta N$ data have been plotted versus ΔK_{III} considering the initial SIF at the beginning the OOP tests. The method used to compute nominal SIF has been extensively described in [32]: a set of FE model adopting three types of shallow micro-notches with a coplanar crack of different depths (emanating from the bottom of the defect and modelled into a rectangular shape), loaded by uniform shear had been carried out by Beretta et al in order to find the value of the geometric factor able to take into account the effect of the notch geometry on ΔK_{III}. In the mentioned work, the results of the FE models were analysed in terms of SIF at the deepest point of the crack with the assumption that the crack, emanating from the notch, has a depth equal to the sum of the notch depth and the co-planar crack length, thereby considering the notch as a crack. The geometric factor was found by comparing the FE stress intensity factors with both the analytical solution of Sih and Kassir [33], which had proved to be satisfactory for semi-elliptical surface cracks, and the bi-dimensional SIF solution for edge cracks.

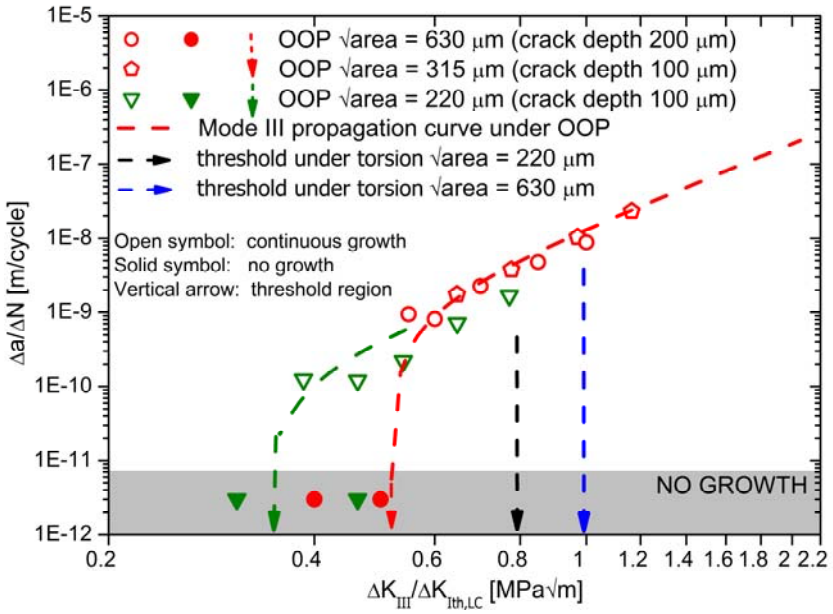

Figure 2.7. Coplanar mode III average propagation rates: multiaxial fatigue tests vs. pure torsional fatigue test results in terms of ΔK_{III}.

A crack size dependency on the threshold value under out-of-phase loading can be inferred from Figure 2.7 due to fact that the mode III threshold values decrease while

the crack size is decreasing. For the above reason, it is of some importance considering the crack size effect when estimating rolling contact fatigue strength.

2.4 Analysis of the fracture surfaces

The fracture surfaces have been carefully observed in order to investigate whether or not micro-structural changes occurred in the material beneath the fatigue region.

2.4.1 Sub-surface crack appearance

Firstly the opening between the crack lips has been examined through polishing and sectioning on a specimen tested at $\Delta K_{III}/\Delta K_{Ith} = 0.8$ (tested interrupted at $N = 2 \times 10^5$ cycles): Figure 2.8 shows that the crack opening is constant within the whole co-planar crack depth. The crack fracture surface opening is almost 18 μm.

Surface fracture fractographies on the sectioned specimen also highlight the typical appearance of a crack under RCF loading conditions (Figure 2.8), several sub-surfaces multiple sites of crack branching can be observed at the main co-planar crack propagation site. The appearance of an RCF crack shows evidence of intense material deformation due to the local rubbing and sliding interaction of the mating crack surfaces.

2.4.2 Micro-structural changes beneath the fracture surface

Rolling contact fatigue testing conditions in steel quite often involve micro-structural changes: “white etched areas (WEA)” and “butterflies” are material damage phenomena frequently observed along the crack ([4],[34]). It has been already reported ([13],[27]) that during fatigue crack growth encouraged by shear (both under mode II and mode III loadings) the changed microstructure appears different compared with the typical WEA and butterflies. The new microstructure has to be related to the large cyclic shear deformation at the crack tip.

The mode III fracture surfaces have been carefully inspected in order to examine the micro-structural changes eventually occurring in the material beneath the contact

surface. Metallurgical and chemical analyses were carried out to find evidence of oxidation phenomena. During the tests, fretting debris emerged from cracks: it can be intuitively supposed that they are engendered by the severe abrasion between the mating rough crack surfaces.

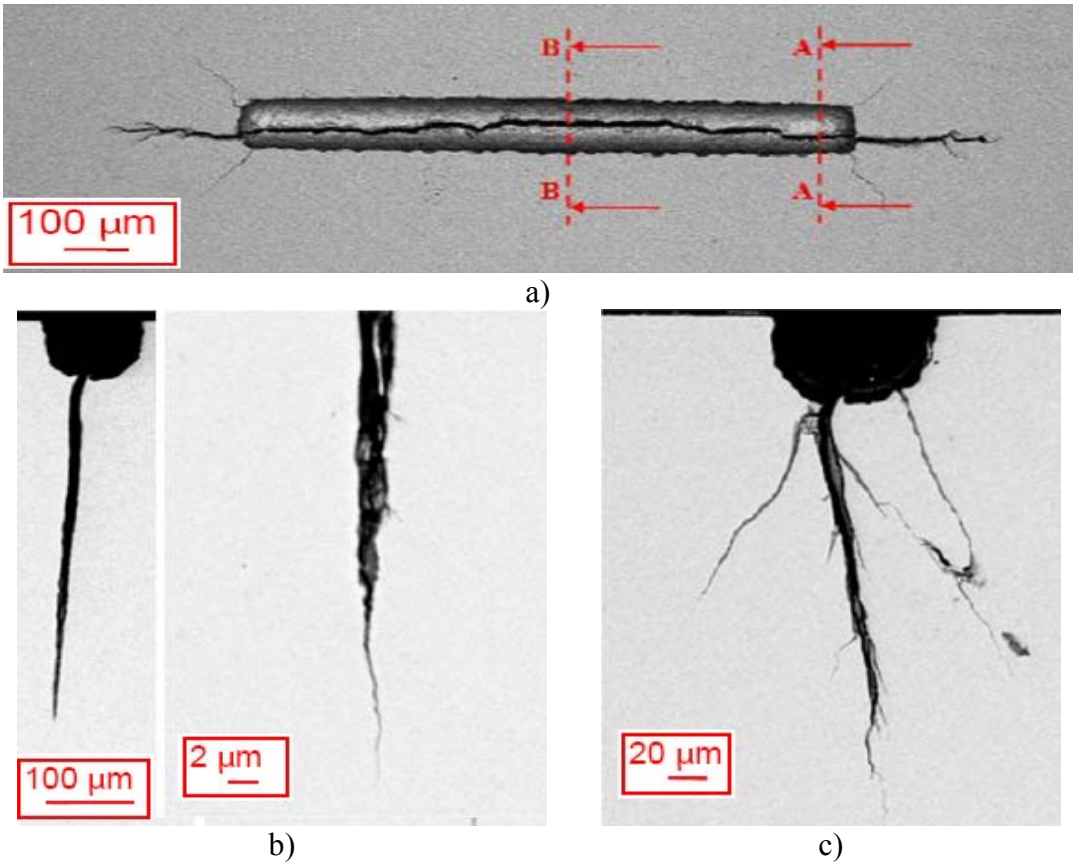

Figure 2.8. Multiaxial fatigue specimen tested at $\Delta K_{III}/\Delta K_{Ith} = 0.8$, test interrupted at N = 2 x 10^5 cycles: a) specimen surface; b) central area section (section B-B) and a magnification; c) typical appearance of a RCF crack (section A-A).

The co-planar fracture surfaces have been first etched in a nital acid solution (nital 0.2 %), and then observed under SEM at high magnifications. Figure 2.9 shows the etched co-planar fatigue surfaces of a micro-notch √area = 630 µm tested at $\Delta K_{III}/\Delta K_{Ith}$ = 0.85 (test interrupted at N = 1.2 x 10^5 cycles); two different gray scale chromatic areas can be distinguished at very high magnifications (2000x):

– light gray areas: such areas correspond to the undamaged regions of the co-planar surface where the original microstructure can be clearly detected; no

evidence of abrasive and dissipative phenomena appears. The undamaged structure is revealed by the presence of the carbides;

– dark gray areas: such areas correspond to the damaged regions of the coplanar surface; a thick oxidized layer appears on the surface, it is proposed to be formed during the abrasive process involving the sliding crack surfaces. Under shear loading the rough asperities of the crack flanks slide over each other; consequently dissipative phenomena arise due to the smearing of the crack flanks. Shear rubbing marks parallel to the applied mode III loading are also noticeable on the oxidized layer.

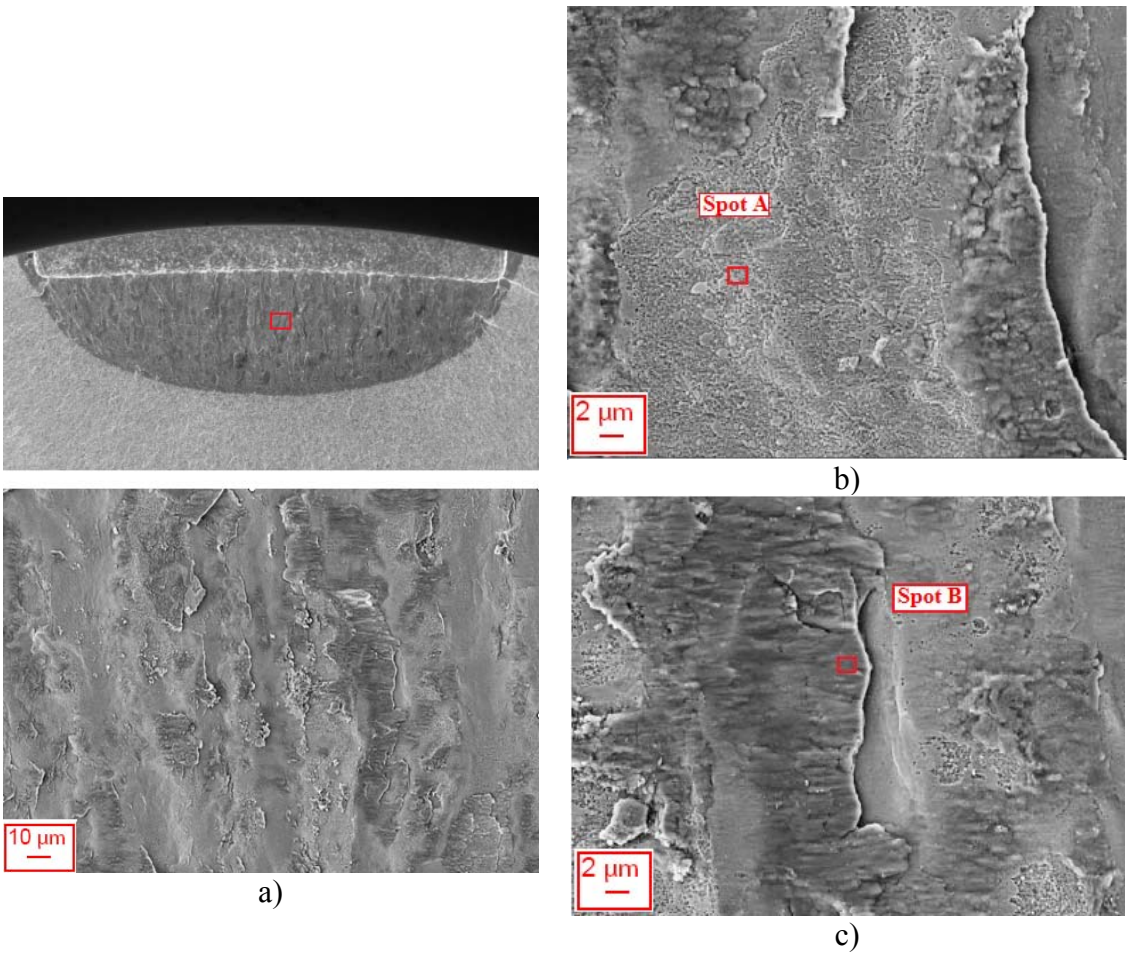

Figure 2.9. Mode III surface SEM observations of a micro-notch √area = 630 µm tested at $\Delta K_{III}/\Delta K_{Ith} = 0.85$ for N = 1.2 x 10^5 cycles: a) fracture surface and high magnification (500 x) of the framed area after etching in nital acid; b)-c) magnifications (2000 x) of the framed area in a) revealing the undamaged and damaged microstructure respectively.

Both light and dark gray areas of the co-planar fatigue region have been analysed in order to inspect the chemical compositions. Chemical analyses were also directed to reveal the presence/absence of oxygen in the damaged (i.e. oxidized)/undamaged fatigue areas. Two arbitrary spots within the damage and undamaged sites have been chosen for the analysis. They are referred as spot "A" and "B" respectively. Results are reported in Table 2.2 and Table 2.3.

	C [%]	**Cr [%]**	**Mn [%]**	**Fe [%]**	**Mo [%]**
Spot A	10.32	9.45	1.24	73.82	5.18

Table 2.2. Weight % of the elements present in spot A.

	C [%]	**Cr [%]**	**O [%]**	**Fe [%]**
Spot B	3.13	1.48	31.28	64.12

Table 2.3. Weight % of the elements present in spot B.

The high weight percentage of oxygen revealed by the chemical analysis of the spot B confirms that the thick dark gray areas are oxidized layers.

Furthermore, besides the examination of the co-planar fatigue region, the mode III fracture surfaces have been sectioned and polished in order to inspect micro-structural changes eventually occurring beneath the fatigue region.

Figure 2.10 reports the etched micro-structure of the co-planar fracture surface central section of a micro-notch $\sqrt{area}$ = 630 μm tested at $\Delta K_{III}/\Delta K_{Ith} = 1$ for N = 1.2 x 10^5 cycles. Two secondary branched cracks can be observed along the co-planar crack depth, approximately close to the notch region. The longest branch crack has a length of about 100 μm, while the shortest secondary crack is around 40 μm. At high magnification gray bands are also observed along the secondary cracks. The thickness of the gray band gradually decreases while approaching the crack tip. The microstructure around the branched cracks is the original ultrafine bainitic material structure: the elongated acicular lamellas of ferrite as well the carbides can be detected in Figure 2.10. Compared with the surrounding bulk material, the gray bands along secondary cracks appear more dark in shading.

Evidence of gray band layers, where the microstructure is dark compared to the original microstructure, are also reported by literature ([13],[27]): the gray band layers are commonly inferred as the typical micro-structural changes characterizing fatigue crack growth encouraged by shear. Murakami called these areas "dark etching areas (DEA)" in contrast to the white etched areas (WEA). It is presumed that the changed micro-structure is created by the large cyclic shear deformation experienced by the crack tip.

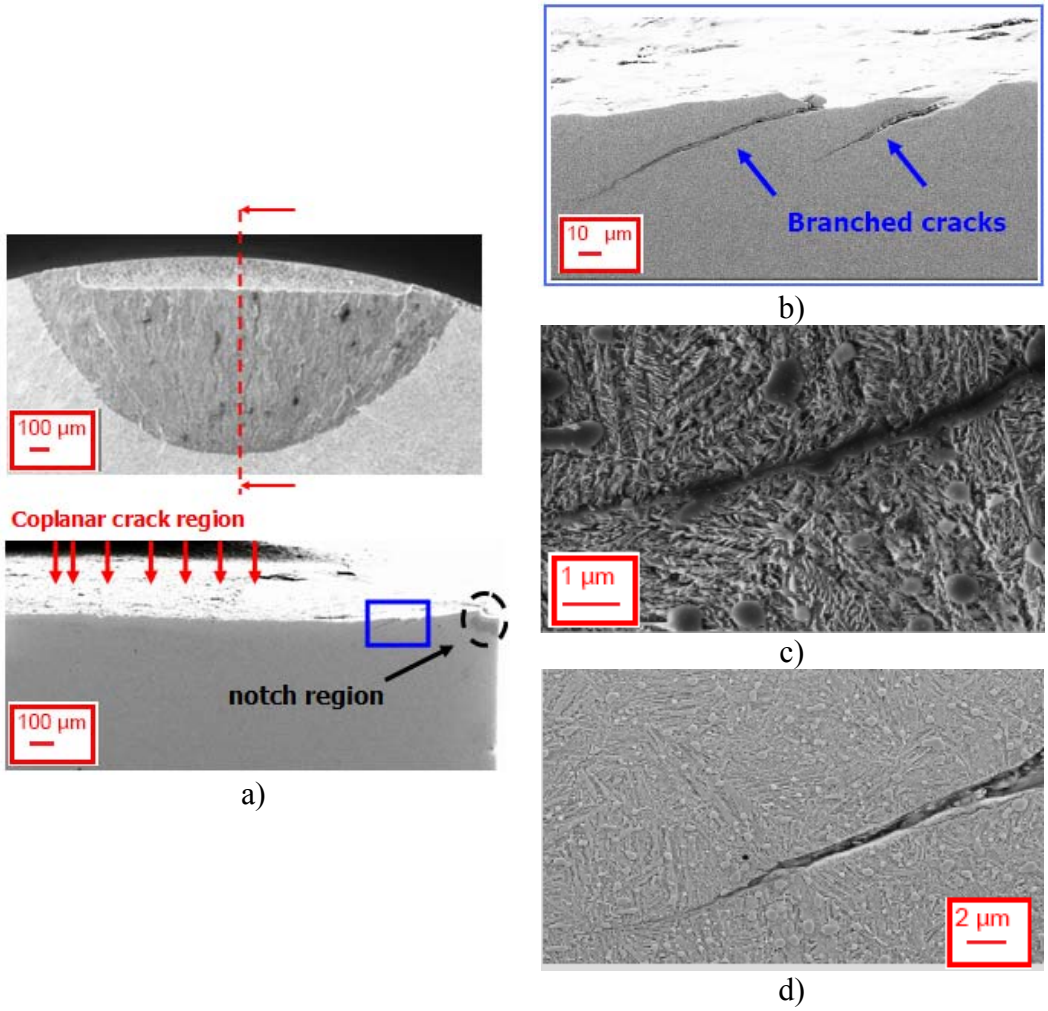

Figure 2.10. Micro-structural changes beneath the fatigue region: a) central section of a micro-notch √area = 630 µm tested at $\Delta K_{III}/\Delta K_{Ith} = 1$ for N = 1.2 x 10^5 cycles: b) evidence of branched secondary cracks along the coplanar crack depth; c)-d) gray band observed along the longest branched cracks in b) (high magnified detail of the secondary crack tip is depicted in c)).

Moreover, it is reported that within the gray bands the micro-structure is extremely fine: under atomic force microscope, the DEA microstructure in ferritic steel appeared formed by very fine grains with radii ranging from 100 to 200 nm (the original ferrite grain size was around 30 μm). The reduction of the grain size is proposed to be responsible for the increase in Vickers hardness (HV): while the original hardness of the ferrite grains was HV = 164 and HV = 175 for mode II and mode III cracks respectively (the Vickers hardness was measured with a load of 0.029 N and 0.098 in the former and latter case respectively), corresponding mean values of DEA Vickers hardness were instead HV = 468 and HV = 678.

2.5 Conclusions

In the present chapter the crack growth and near- threshold behaviour of short cracks under rolling contact fatigue loading was assessed. A novel experimental methodology, previously developed by Beretta et al in [16], has been consolidated onto a bearing steel material. Furthermore, fatigue growth assessments onto a railway steel have also been reported in *Appendix A*.

The experimental procedure was directed to obtain mode III co-planar crack propagation data on pre-cracked specimens containing shallow micro-notches with $\sqrt{area} < 1000$ μm. The hourglass micro-notched samples were subjected to an out-of-phase load pattern with the axial loading always in compression and shifted 90° in respect to the alternating torsion.

Fatigue test results on the bearing steel under rolling contact loadings confirmed that:

- the out-of-phase pattern enhances the co-planar crack growth (mode I is prevented as long as ΔK_{III} is lower than ΔK_{Ith}); the mode III threshold values under out-of-phase loads $\Delta K_{III,OOPth}$ are also much lower than the thresholds under simple shear;
- a short crack effect is found; the mode III threshold value under out-of-phase loads $\Delta K_{III,OOPth}$ decreased with a decrease in crack size;

– the enhancement of the co-planar crack growth under RCF conditions is associated with severe rubbing of the crack faces and a residual opening between the crack lips is also observed.

Fractographic observations of the co-planar fracture surfaces, after etching in nital acid, showed two distinctive chromatic areas. Evidence of oxidation phenomena was revealed by chemical analysis of the dark layers on the mode III macroscopic appearance.

Micro-structural changes were also found beneath the contact surface, after sectioning and polishing and dark etched areas (DEA) were observed inside secondary cracks developed along the coplanar crack depth close to the notch region.

Chapter 3
Comparison of crack growth and near-threshold behaviour under simple shear and RCF conditions

3.1 Introduction

The experimental results presented in *chapter 2*, together with similar results onto a gear steel [16], have clearly shown that the out-of-phase load pattern encourages the co-planar growth and leads to a severe reduction of the minimum mode III stress intensity factor range ΔK_{III} at which co-planar crack growth could occur. Neverthless, the enhanced mode III propagation promoted by the out-of-phase testing condition does not appear to be justified within a linear elastic fracture mechanics description. In fact, as opposed to simple shear, the superimposition of compression on the alternating torsion should lead to an increase in friction, which in turn reduces the crack driving force ([15], [35]-[36]) more than in the case of simple shear.

On the other hand, the other distinctive feature of the "out-of-phase growth" is the fact that crack advance is characterised by a residual crack opening caused by plastic deformation and wear (recognizable on account of the large amount of debris). This opening can significantly reduce the friction dissipation during the out-of-phase tests.

Moreover, until now no attempts have been made to verify the effective growth rates under sub-surface rolling contact fatigue condition and to compare them with data under simple shear; on the contrary, only experimentally derived shear growth data on small defects have been incorporated into RCF models of subsurface fatigue [4],[14].

The aim of the present chapter is to compare the mode III crack growth and threshold data under pure shear and rolling contact testing conditions. Furthermore, in order to provide a unique description of the mode III crack propagation behaviour, an attempt is done to combine the experimental trend over the above testing conditions together

with the effective mode III SIF range calculation. A this scope, a globally elastic micro-mechanical model capable of estimating the effective ΔK_{III} has been employed. Moreover, the effect of the residual crack opening between the crack lips on crack face friction under OOP loads has been investigated and included in the theoretical modelling analysis.

3.2 Torsional fatigue test results

Although torsional test results on the bearing steel, were not obtained in the current work, they are now briefly presented in order to allow the theoretical discussion (developed in both the present and the following chapters) on the comparison between the mode III crack propagation and fracture behaviour under RCF and pure torsional loadings.

Torsional fatigue tests were carried out on micro-notched hourglass specimens at a stress ratio R = -1 using a RUMUL CRACKTRONIC resonance machine operating at an average frequency of 60 Hz. The fatigue test procedure adopted has already been described in *chapter 2* for the OOP tests.

Following an examination of the mode III fracture surfaces, two main types of co-planar growth regime can be distinguished, see Figure 3.1:

- the "discontinuous growth regime": this regime is observed at ΔK_{III} levels close to ΔK_{Ith}; the macroscopic fracture appearance is characterised by the formation of semi-elliptical mode III pockets;
- the "continuous co-planar growth regime": this regime is observed at ΔK_{III} levels higher than ΔK_{Ith}; it is characterized by a stable mode III co-planar growth revealed by a flat macroscopic appearance of the fracture surfaces.

The mode III threshold ΔK_{IIIth}, corresponding to a "discontinuous" coplanar crack is very close to ΔK_{Ith}. The conclusion that ΔK_{IIIth} corresponds to a discontinous co-planar crack is also confirmed by the average $\Delta a/\Delta N$ measured from the crack advance

showing typical propagation rates for a threshold region. On the contrary, the continuous growth is characterised by $\Delta a/\Delta N$ in the range of 10^{-9} m/cycle.

Under pure torsional loading, failures always occurred in mode I on tilted fracture planes at 45° which had been nucleated along thin shear cracks at the bottom of the micro-notches.

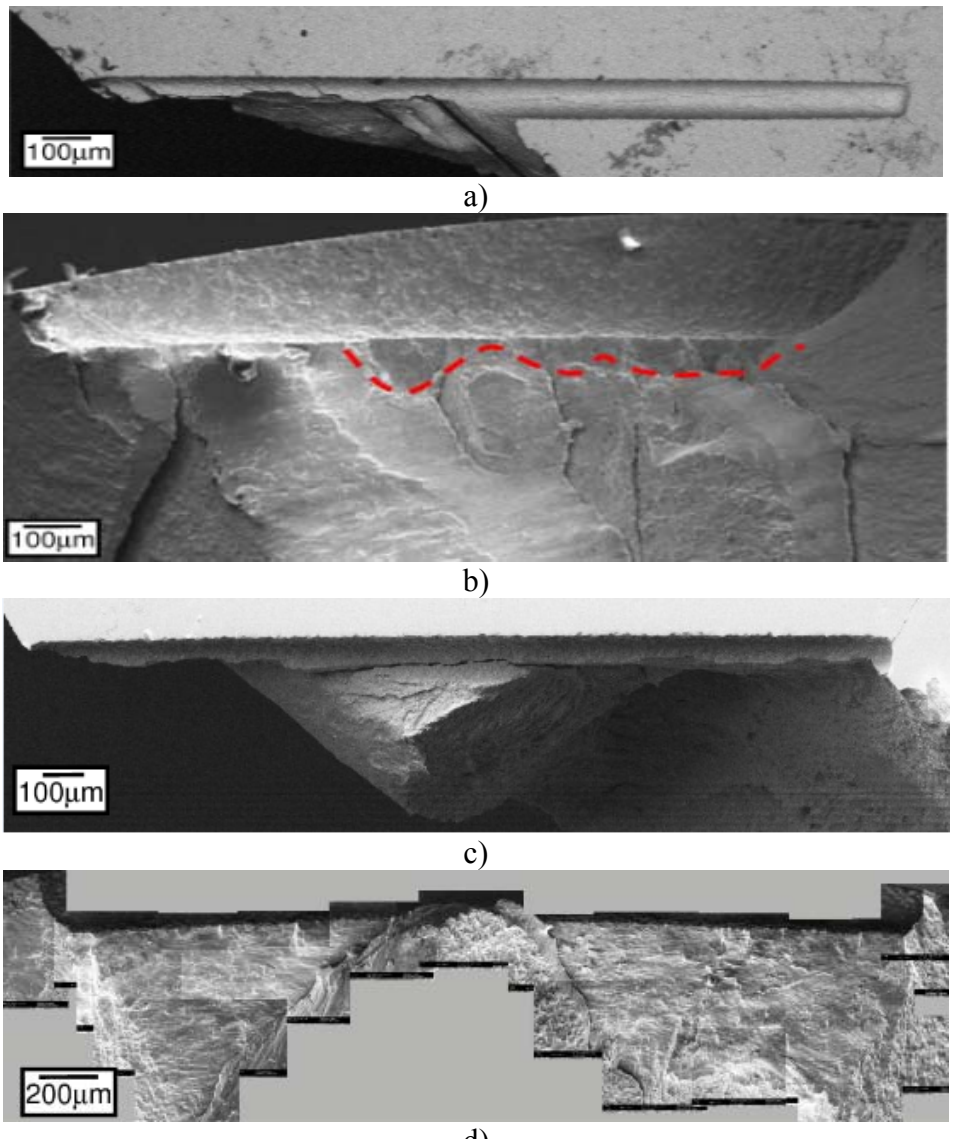

Figure 3.1. SEM photos of torsional samples (micro-notch √area = 630 µm) after static fracture: a) top view and b) 90° tilted view of a discontinuous co-planar crack (sample tested at $\Delta K_{III}/\ \Delta K_{Ith}$ = 1.18 broken at N = 6 x 10^4 cycles); a) top view and b) 90° tilted view of a continuous co-planar crack (sample tested at $\Delta K_{III}/\ \Delta K_{Ith}$ = 1.75 broken at N = 3 x 10^3 cycles).

Debris emission, caused by intense rubbing was mainly observed during the tests carried out at high ΔK_{III} levels. In order to provide a straightforward comparison between the OOP and pure torsional fracture surfaces, metallurgical and chemical analyses have been conducted. Figure 3.2 shows a high magnification (2000 x) of the etched co-planar fatigue region (blue framed area) obtained testing a micro-notched sample ($\sqrt{area}$ = 220 μm) at $\Delta K_{III}/\Delta K_{Ith}$ = 1.15 (test interrupted at N = 9 x 10^4 cycles). The fracture surface appears less oxidized in comparison with the RCF co-planar fatigue region (see the results in *chapter 2*). Small oxidized areas are localized in the co-planar extent. A limited presence of oxygen in the damaged site, spot "A", is revealed by chemical analysis. Results are reported in Table 3.1.

	C [%]	**Cr [%]**	**O [%]**	**Fe [%]**
Spot A	6.17	1.75	3.97	88.11

Table 3.1. Weights % of the elements present in spot A.

The small weight % of oxygen can also be attributed to the oxidation processes provoked by a chemical reaction of the material surface with the ambient air (a long time is passed between the metallurgical inspections of the torsional fracture surfaces, carried out in the current study, and the experimental tests).
Finally, the bearing steel torsional fatigue data together with the experimental trend under RCF loadings are shown in Figure 3.3.

3.3 Comparison of torsional and out-of-phase tests results

When the applied stress-intensity factor range ΔK_{III} is used to combine crack growth data under simple shear with the experimental trend under OOP loading (see Figure 3.3) or vice versa, a unique description of mode III fracture behaviour may not be achievable. The lack of correlation of crack growth data can be attributed to dissipative phenomena, involving friction and abrasion between the mating crack surfaces. The friction dissipation of the effective driving force, actually experienced at the crack tip, is crucial when dealing with mode III fracture; however, frictional

effects are not taken into account when ΔK_{III} is used to characterize the mode III fracture behaviour.

In the current discussion an attempt is done to quantify the role of crack face friction on mode III propagation behaviour under both simple shear and rolling contact testing conditions.

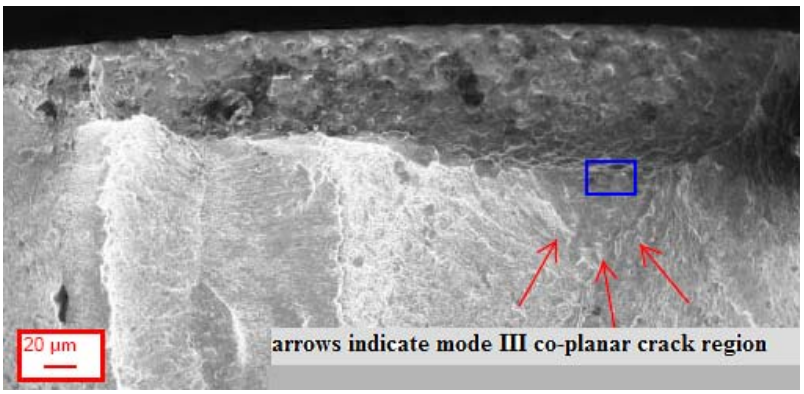

a)

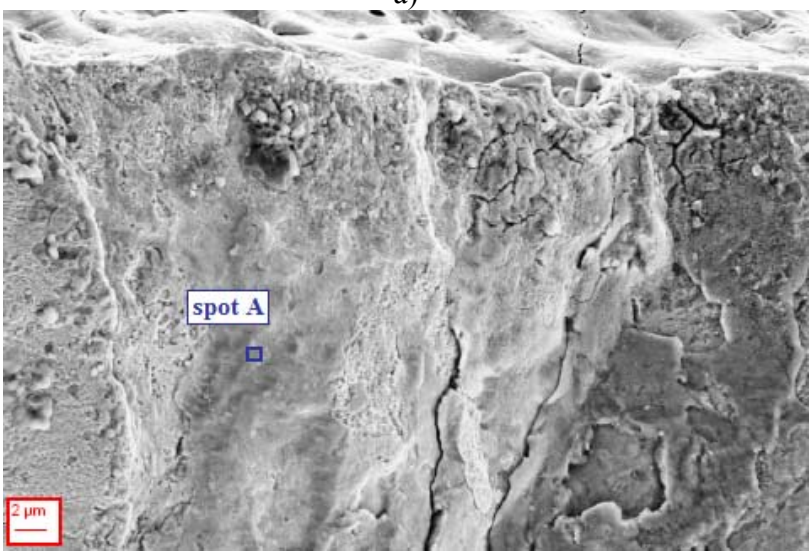

b)

Figure 3.2. Mode III surface SEM observations of a micro-notch √area = 220 µm tested at $\Delta K_{III}/\Delta K_{Ith} = 1.15$ for N = 9 x 10^4 cycles: a) fracture surface and b) high magnification (1000 x) of the framed area after etching in nital acid.

3.3.1 Estimation of the effective ΔK_{III}: a micro-mechanical frictional model

During cyclic shear loading (both mode II and mode III) the crack surfaces move parallel to each other while remaining closed: therefore friction between sliding crack flanks exists. In a fracture mechanics representation, crack surfaces are commonly

assumed macroscopically flat, on a microscopic scale, in stead, they have a rough profile. During the relative shear displacements, the contacting peaks and valleys of the rough crack surfaces interact in a complicated manner through a combination of sliding, sticking and other dissipative phenomena.

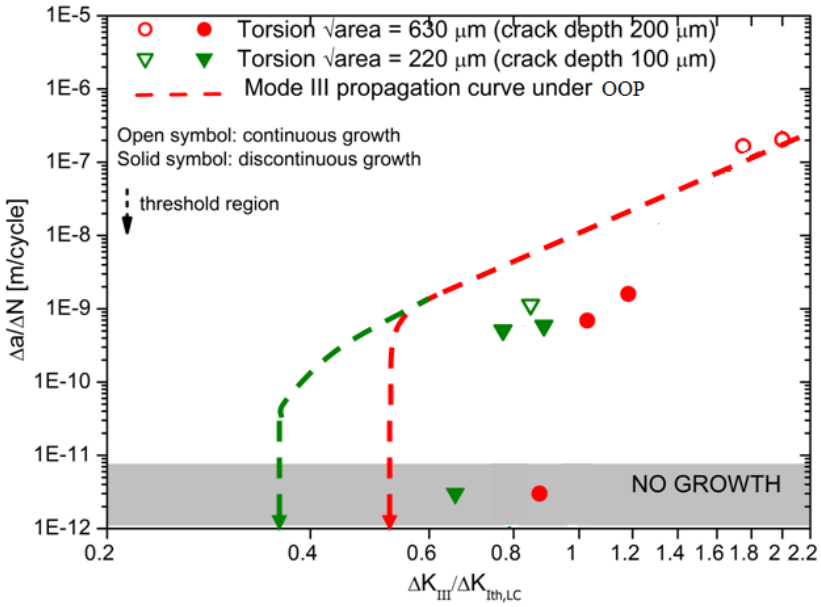

Figure 3.3. Average propagation rates obtained for mode III co-planar cracks under pure torsional loading.

Consequently, the nominal external value of ΔK_{III}, partly dissipated by friction, is reduced to a lower effective value. The mentioned phenomenon was named by Tschegg [37] "sliding mode crack closure", analogously to fatigue crack closure in mode I. During his experiments [26] on circumferentially notched specimens of AISI 4340 steel, he observed a monotonic decrease of the crack growth rate with increasing crack length at constant applied ΔK_{III}. In order to exclude the influence of friction between the sliding crack surfaces, Tschegg extrapolated the "true" mode III growth rates corresponding to a crack of length approximately equal to zero, thereby correlating mode III crack growth rates with the effective stress intensity values.

Since the effective SIF is physically responsible for crack propagation, it appears necessary to characterize the mode III fracture behaviour under both pure shear and RCF testing conditions by adopting the effective ΔK_{III}. At this scope, a globally elastic micro-mechanical model has been employed and the effect of crack face friction on

the nominal ΔK_{III} has been quantified. The residual opening between the crack lips, peculiar of the OOP tests, was also taken into account in the theoretical analysis. Finally, the two test methods (i.e. pure torsion and RCF loadings) have been compared. The model used to estimate the effective ΔK_{III}, under out-of-phase and pure torsion tests, assumes a 2D crack of depth *a* at the free surface of an elastic-plastic half space. The presence of three-dimensional effects can be neglected for the narrow defects since it has been shown that for a/b > 1.2 the K_{III} at the crack tip of a straight crack ahead of the notch rapidly approaches ($0.95 < K_{III,3D} / K_{II,2D} < 1$) the 2D solution for edge cracks [38] (see Figure 3.4). The effective stress intensity factor at the tip of the crack is :

$$\Delta K_{III,eff} = \Delta K_{app} - 2K_f \tag{3.1}$$

where K_f is the "frictional stress intensity factor" (the mode III stress intensity dissipated by friction) and factor 2 accounts for the frictional resistance at the maximum and minimum value of applied shear stress τ. The frictional shear stress intensity factor K_f is analytically calculated using the fracture mechanics approach based on the weight function method for the geometry configuration of an edge crack subjected to an arbitrary tangential stress distribution [39]:

$$K_f = \sqrt{\frac{a}{\pi}} \int_0^a \frac{\tau_f(x)}{\sqrt{a^2 - x^2}} dx \tag{3.2}$$

where:

$$\tau_f(x) = \mu \sigma_c(x) \tag{3.3}$$

The frictional shear stresses $\tau_f(x)$, acting in opposition to the applied shear stress, are proportional to the normal contact stresses according to the Coulomb's law, Eq. (3.3) μ is the friction coefficient (a value of 0.5 is assumed for this parameter).

It is worth remarking that Eq. (3.3) is also valid for a through crack of length 2a in a plane: therefore it is here assumed (the degree of approximation of this assumption

was then verified by means of a FE analysis of the open crack) that the pressure acting on the crack face could be simply calculated as a 2D crack under plane strain condition.

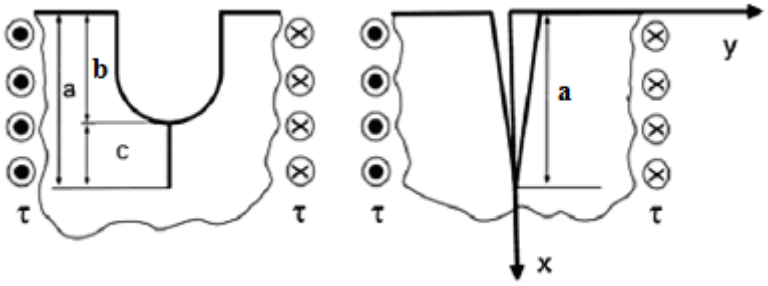

Figure 3.4. Schematic of the 2D simplification of the shallow notch + crack under mode III.

3.3.2 Estimation of contact pressures and ΔK_{IIIeff} under OOP

In order to correctly estimate the contact stresses on the crack of Figure 2.8 (c = 520 μm), the crack profile has been accurately reconstructed by image processing and a detail of the crack is depicted in Figure 3.5. Due to the magnified vertical axis, it can be observed that the crack is not exactly co-planar.

In order to calculate the normal stresses $\sigma_c(x)$ an analytical model based on the Newman crack closure model [40], but suitably modified, is used. The model is based on the superimposition of two elastic problems on the experimentally observed physical crack:

- a crack in a infinite plate subjected to a remote compressive loading σ_∞;
- a crack in a infinite plate subjected to a partial normal stress on its faces.

In the present study the crack edges have been divided into n discrete bar elements. The length of an element along the crack profile, L_j, is the experimentally observed crack opening: when the element length is smaller than the current crack-surface displacement due to remote compressive loading, V_j, the element goes in contact and a normal stresses arises in order to make $V_j - L_j = 0$, see Figure 3.5.

The displacement at point i is:

$$V_i = \sigma_\infty f\left(x_i\right) - \sum_{j=1}^{n} \sigma_{c,j} g\left(x_i, x_j\right) \tag{3.4}$$

where $f(x_i)$ and $g(x_i, x_j)$ are influence function given by:

$$f\left(x_i\right) = \frac{2\left(1-\upsilon^2\right)}{E^2}\sqrt{a^2 - x_i^2} \tag{3.5}$$

$$g\left(x_i, x_j\right) = G\left(x_i, x_j\right) + G\left(-x_i, x_j\right) \tag{3.6}$$

The influence function $f(x_i)$ depends on the material constants, i.e. the Young modulus E and the Poisson ratio v, as well as on the total crack length a. On the other hand, the influence function $g(x_i, x_j)$ is a complex function of the $G(x_i, x_j)$ and $G(-x_i, x_j)$, reported in Eq. (3.7). The latter equation is a function of the material constants and of the geometric parameters a and w_j, where w_j is the width of the j-th crack element.

$$\begin{aligned} G\left(x_i, x_j\right) = \frac{2\left(1-\upsilon^2\right)}{\pi E}\Bigg\{ & \left(b_2 - x_i\right)\cosh^{-1}\left(\frac{a^2 - b_2 x_i}{a\left|b_2 - x_i\right|}\right) + \\ & -\left(b_1 - x_i\right)\cosh^{-1}\left(\frac{a^2 - b_1 x_i}{a\left|b_1 - x_i\right|}\right) + \sqrt{a^2 - x_i^2}\left[\sin^{-1}\left(\frac{b_2}{a}\right) - \sin^{-1}\left(\frac{b_1}{a}\right)\right]\Bigg\} \end{aligned} \tag{3.7}$$

where $b_1 = x_j - w_j$, $b_2 = x_j + w_j$.

The compatibility equation is expressed as $V_j - L_j = 0$ which allows to obtain:

$$\sum_{j=1}^{n} \sigma_{c,j} g\left(x_i, x_j\right) = \sigma_\infty f\left(x_i\right) - L_i \qquad \text{for } i = 1,\ldots,n \tag{3.8}$$

The linear system of equations, Eq. (3.8), is iteratively solved by adding the following constraints: the maximum value of the contact stresses cannot exceed the material yield stress σ_y as well as the normal stresses are forced to be zero for elements which are not in contact.

Calculations for the crack in Figure 2.8 (c = 520 μm) have been carried out and the results are shown in Figure 3.6. At the minimum value of the compressive loading cycle only a few crack face elements come into contact (9.7% of the crack surface) with pressures (the normal stresses σ_i) which are equal to the material yield stress σ_y.
By performing the analytical computation of the frictional stress intensity factor for each step of the compressive loading cycle, it can be concluded that there is no significant reduction of the effective cyclic mode III stress intensity factor due to friction: the effective value of the stress intensity ΔK_{IIIeff} remains almost equal to its nominal value, i.e. $\Delta K_{IIIeff} / \Delta K_{IIIapplied} = 95\%$.

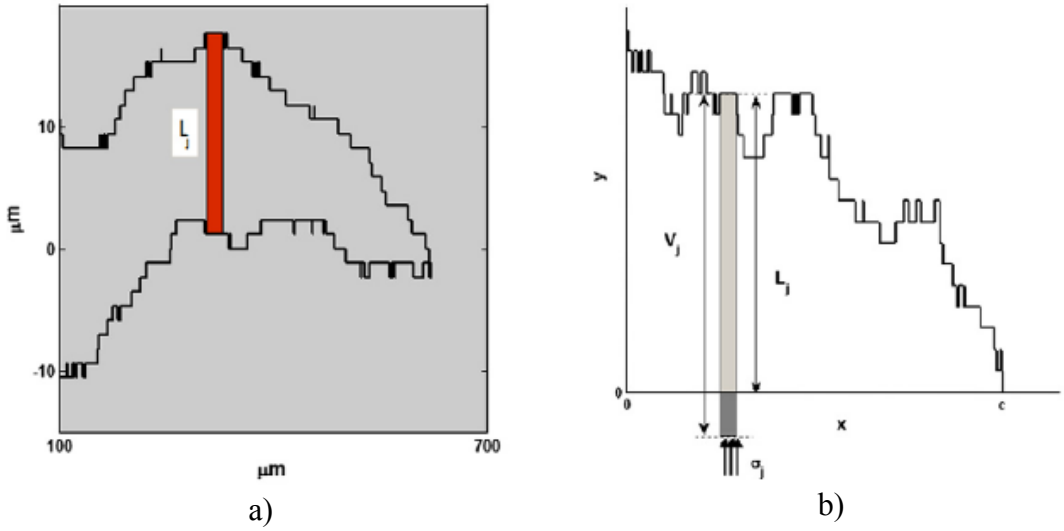

a) b)

Figure 3.5. Estimation of contact pressures: a) digitalization of the crack profile fro the crack of Figure 2.7; b) definition of the variables adopted in the calculation of pressure distribution at minimum stress in terms of compatibility equations.

3.3.3 Verification by FE analysis of ΔK_{IIIeff} under OOP loads

FE analyses have been carried out in order to verify the analytical calculations shown in the previous section. It should be noted that neither the analytical nor the FE models make an attempt to explain why the crack lips are open. Moreover they are employed in order to estimate (without any simplified assumption about the crack geometry) the effect of friction on the nominal cyclic mode III stress amplitude $\Delta K_{IIIapplied}$ at the deepest point of the crack.

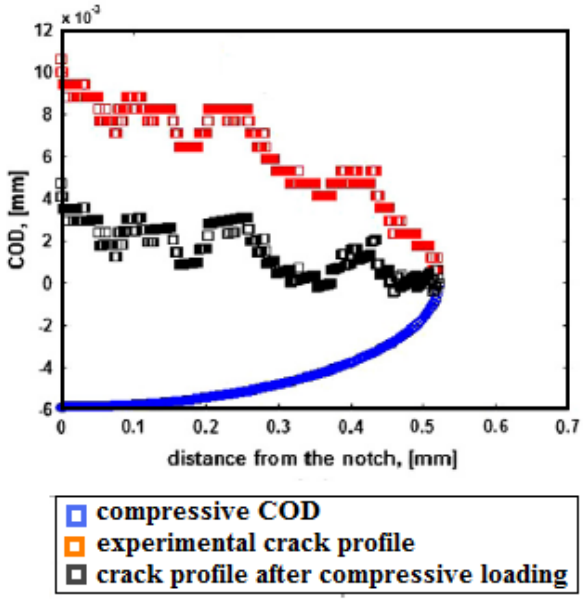

a)

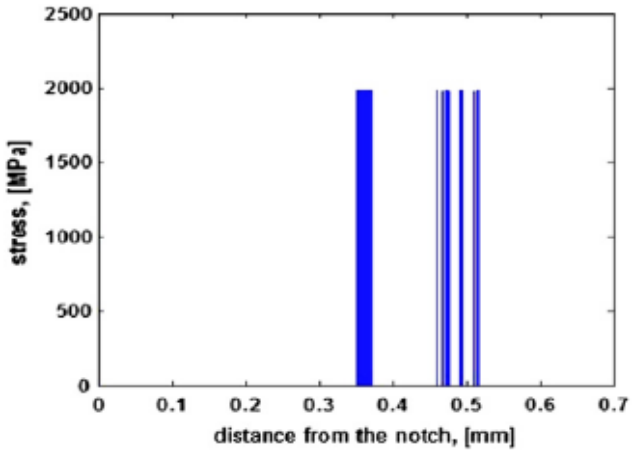

b)

Figure 3.6. Results of pressure distribution analysis: a) calculation of crack profile at the maximum compressive stress; b) distribution of contact stresses along the crack.

For this reason a pure elastic numerical model has been constructed using the boundary conditions described in [29],[32] and by introducing semi-circular cracks in accordance with experimental evidence (coplanar crack depth c = 520μm) without modelling the notch itself. The depth of coplanar crack makes this simplification acceptable due to the disappearance of the notch effect moving away from it. In the finite element model the crack is open and the value of this opening is estimated in

accordance with experimental evidence (see Figure 3.7). Loads are applied by means of two amplitude load definitions shifted on 90° degrees according to the experimentally used load pattern. Analyses have been carried out by adopting three different values of the friction coefficient (μ = 0.5, μ = 0.7, μ = 1). A 20-node isoparametric element with reduced integration (ABAQUS C3D20R element) is used in the three dimensional analysis. A fine structural mesh is created along the crack front. An additional hard contact "condition" is introduced to prevent penetration of the two crack lips. Moreover a Coulomb friction model is also used.

Even with a simplified crack geometry (owing to the fact that the detailed discretization of Figure 3.5 could not be modelled), the results of the FE analysis show that the crack faces remain almost open during an OOP cycle. When the crack is open, the effective cyclic mode III stress intensity factor remains equal to the nominal value thereby confirming that the experimental evidence of surface rubbing prevents friction between the mating crack faces under the compressive part of the OOP loading cycle.

3.3.4 Estimation of ΔK_{IIIeff} under pure torsional loading

Fractographic features observed for mode III fatigue crack growth of specimens containing shallow defects showed evidence of intense rubbing and production of debris which flattens the surface during crack propagation [16]. The observation of smearing of the fracture surfaces is solely due to the frictional effects during the torsional loading cycle: in fact, even though in a fracture mechanics representation, the fracture surface is idealised as macroscopically flat, on a microscopic scale, the crack front is rough and consists of peaks and valleys. During mode III loading, the roughness asperities, like the crack faces, are displaced in relation to one another. The mode I opening induced by the mismatch of the fracture surface roughness produces a significant friction which leads to the characteristic decrease of crack speed resulting in the coplanar growth observed in mode II and mode III.

This phenomenon is somewhat similar to fatigue crack closure under mode I loading induced by fracture surface roughness or morphology and exhaustively described by Suresh et al [41]. The mechanism, termed "roughness-induced crack closure", arises when the size-scale of the fracture surface roughness is comparable to the crack tip

opening displacements. The study of Suresh et al has also indicated that the roughness-induced closure, under nominal mode I loading, is usually characterized by significant shear displacements at the crack tip (confirmed experimentally using stereo-imaging pictures).

Large mode II displacements were also found to accompany crack advance at the near-threshold levels, where maximum plastic zone dimensions are less than the micro-structural grain size. The crack path morphologies revealed by metallographic sections and replicas of near-threshold fatigue cracks in steel [42], aluminium alloys, and titanium [43] were characterized by a faceted or zig-zag fracture path, thereby confirming the idea that the contact between crack surfaces occurs at discrete points due to the roughness-induced closure mechanism.

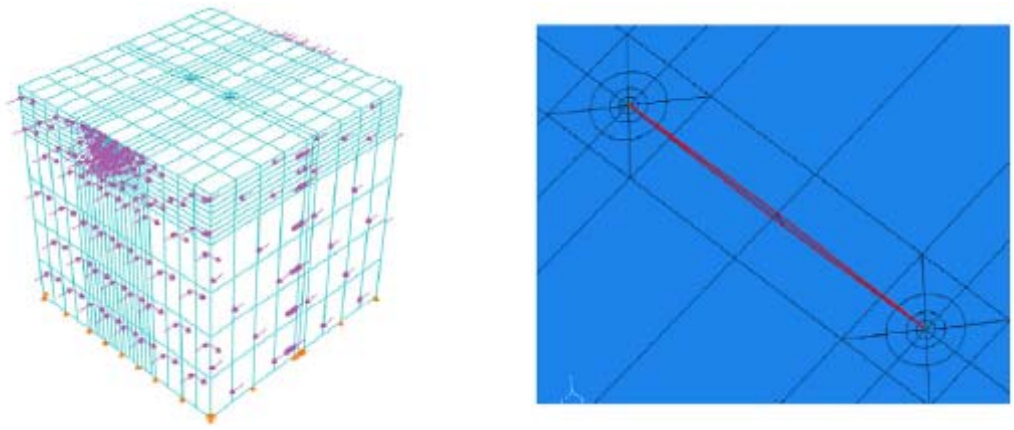

Figure 3.7. Verification by FEM of the ΔK_{IIIeff} for the crack of Figure 3.5: a) FEM model of the crack subjected to the OOP stress cycle; b) magnification of the open crack simulating the profile of the real crack.

The first attempt to quantify the effect of fracture surface roughness on fatigue crack growth promoted by shear is due to Gross and Mendelsohn [44]-[45]: they developed a model of frictional interaction capable of quantifying the magnitude of the frictional stress intensity factor K_f, due to the mismatch of rough fracture surfaces during anti-plane shear loading. The model was employed to analyze both monotonic and cyclic crack growth data obtained testing cylindrical specimens with circumferentially edge cracks under torsion.

Although the importance of the fracture surface interaction effect on fatigue propagation of shear cracks is acknowledged, literature provides few theoretical works directed to quantify the effective stress intensity factor under pure anti-plane shear. Besides the study of Gross and Mendelsohn, a contribution in this direction has to be attributed to Vaziri and Nayeb-Hashemi [46]. In the latter work the results of the theoretical investigation were used to model the dynamic response of circumferentially cracked round shafts under cyclic torsional loading.

In the current study the analytical model of Gross and Mendelsohn, suitably modified, is employed in order to correlate mode III fatigue crack growth data obtained under pure alternating torsion with the effective SIF ΔK_{IIIeff}. Once again, the model used, is the 2D model shown in Figure 3.4.

The frictional SIF is due to fracture surface interactions: during mode III cyclic loading the crack faces, which are modelled as rough (with an average wavelength, λ, and an average amplitude, t), may interact over some extent of the edge crack, thereby causing the smearing of the roughness asperities. The fracture surface interaction may induce normal contact stresses σ_c among the mating asperities on the crack faces, resulting in frictional shear stresses τ_f, acting in opposition to the applied shear stresses and proportional to the contact stress through the friction coefficient μ, Eq. (3.3), once again assumed equal to 0.5. The extent of the interaction between the crack faces, x_c, and the resulting contact pressure distribution $\sigma_c(x)$ depends on both the applied remote shear loading and the roughness parameters.

Unlike the original work of Gross and Mendelsohn [44]-[45] and the subsequent work of Vaziri and Nayeb-Hashemi [46], where the roughness parameters were reasonably hypothesized, in the current work both the average amplitude and wavelength of the asperities are taken from experimental roughness measurements: a discretization of a typical fracture surface profile in a torsional sample at a distance from the width of notch equal to the value of the pre-crack depth is depicted in Figure 3.8.

While the roughness asperity height, along the fracture surface where the roughness profile has been measured, shows evidence of frictional dissipation and smearing of the crack faces since, in these regions, the profile height is smoother than in the other crack regions (see Figure 3.8), the roughness asperity wavelength has almost the same

average value along the profile measured (a value of 2 μm gives an average description of the measurements).

According to the approach used by Gross and Mendelsohn, the extent of crack surface interaction and the possible contact pressure distribution can be obtained by considering the crack opening (mode I) and sliding (mode III) displacements respectively.

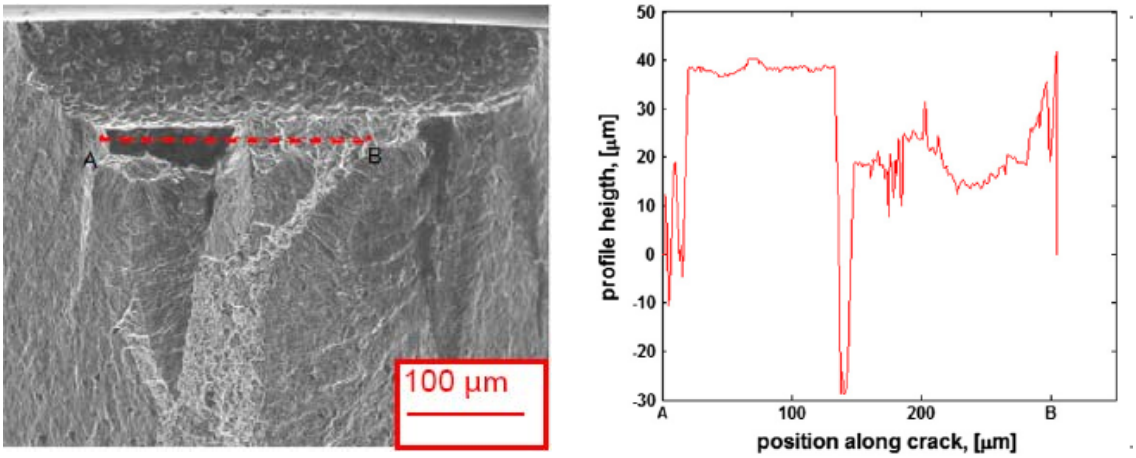

a) b)

Figure 3.8. a) Torsional specimen (micro-notch √area = 221 μm) tested at $\Delta K_{III}/\Delta K_{Ith}$ = 1.1 for 8.7 x 10^4 cycles; b) typical fracture surface profile.

The mode III displacements for an edge crack subjected to anti-plane shear can be written as:

$$u_3(x) = \frac{2\tau}{G}\sqrt{a^2 - x^2} \tag{3.9}$$

where G is the shear elastic modulus. Once the shear displacements are greater than half the wavelength of the roughness, asperities are overcome meaning that the extent of fracture surface interaction is given by the position x_c along the edge crack where:

$$u_3(x_c) = \frac{\lambda}{2}, \quad x_c = \sqrt{a^2 - \pi a\left(\frac{\lambda G}{4\Delta K_{IIIapplied}}\right)^2} \tag{3.10}$$

In Eq. (3.10) λ is the physical parameter used to describe the asperity wavelength of the roughness profile.

It is assumed that there is no interaction between the crack faces for $x < x_c$, since the crack opening displacement, resulting from the mismatch of the asperities, is higher than the asperity height for $x \le x_c$. In particular mode I displacements depend on mode III displacements for the whole extent of the crack surface interaction, i.e. :

$$\begin{aligned} u_1(x) &= \frac{2t}{\lambda} u_3(x) \qquad \text{for} \quad x_c \le x \le a \\ u_1(x) &> t \qquad\qquad\quad \text{for} \quad 0 \le x \le x_c \end{aligned} \tag{3.11}$$

where the term $2t / \lambda$ accounts for the inclination of roughness flanks and t is the roughness asperity height.

The resulting contact pressure distribution has been found by numerically solving the elastic problem of a central crack partially loaded along its crack faces (Figure 3.5); the element discretisation of the crack edge, previously described, is adopted. The displacement at a point i is:

$$V_i = \sum_{j=1}^{n} \sigma_{c,j} g(x_i, x_j) = u_1(x_i) \tag{3.12}$$

where the COD field can be calculated from Eq. (3.11) and the influence function from Eq. (3.6).

Furthermore, the maximum value of the contact stresses cannot exceed the material yield stress σ_y and the normal stresses are forced to be zero for $x < x_c$ (where there is no interaction between the crack faces). Once the traction distribution on the crack edge is numerically calculated, the frictional stress intensity factor can be calculated by means of Eq.(3.3).

The fundamental difference in the current model and the original work of Gross and Mendelsohn [44] has to be found in the method used to calculate the normal stress distribution along the crack flanks: in the theoretical study of Gross and Mendelsohn the contact pressure was obtained by modelling the crack surface interaction as edge

dislocations. The crack opening displacements at any point along the macroscopic crack were modelled as a continuous distribution of infinitesimal edge dislocations, after having assumed the Burgers vector perpendicular to the crack plane.

Furthermore, the current model differs from the work of Vaziri and Nayeb-Hashemi [46], where the possible pressure profiles along the crack flanks were hypothesized based on the assumption that the largest normal pressure developed at the crack tip.

Mode III fatigue crack growth data in terms of the effective range of the stress intensity factor ΔK_{IIIeff} are shown in Figure 3.9.

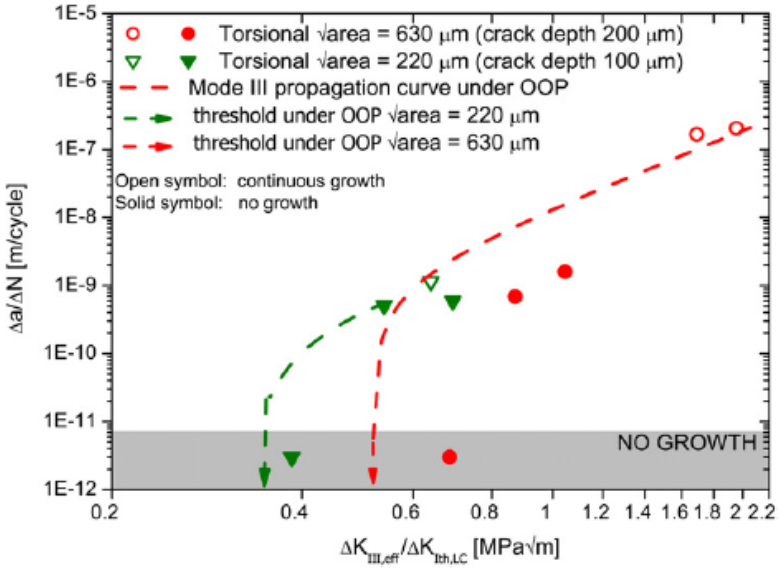

Figure 3.9. Average mode III co-planar crack propagation rates.

The effective cyclic mode III threshold $\Delta K_{IIIth,eff}$ under simple shear is smaller than the nominal threshold mode I threshold ΔK_{Ith}, thereby supporting the experimental evidence of mode III coplanar stable propagation in multiaxial out-of-phase tests where the $\Delta K_{IIIapplied}/\Delta K_{Ith}$ ratio is less than one.

Furthermore, when the effective mode III SIF range is used to correlate the torsional crack growth data with the experimental trend under OOP, a unique description of mode III fracture behaviour can be achieved: torsional data lie on the out-of-phase propagation curve and the threshold data fall on the RCF threshold region.

3.4 Conclusions

In the present chapter an attempt has been done in order to correlate the out-of-phase and torsional crack growth data for the bearing steel.

Torsional fatigue results were obtained after testing pre-cracked micro-notched specimens at a stress ratio R = -1. Following an examination of results, three fundamental differences between torsional and RCF fatigue assessments can be remarked:

- in torsional experiments the values of ΔK_{III} – at which the onset of co-planar propagation occurs, even with a discontinuous growth, - are very close to those of ΔK_{Ith} meaning that co-planar crack growth becomes stable for $\Delta K_{III} > 1.2\ \Delta K_{Ith}$;
- the threshold condition determined in pure torsion is much higher than $\Delta K_{III,OOPth}$;
- the co-planar crack growth under pure torsional loading is not characterized by a residual opening between the crack faces, the latter associated with the severe rubbing of the crack faces.

Furthermore, when frictional dissipative effects are not taken into account a lack of similarity between torsional crack growth data and the experimental trend under RCF is observed.

During cyclic shear loading the fracture surface move parallel to each other while remaining closed. As a result the contacting peaks and valleys of the microscopically rough fracture surfaces interact in a complicated manner through a combination of sliding, sticking and other abrasion phenomena. Consequently the nominal external value of ΔK_{III}, partly dissipated by friction, is reduced to a lower effective value.

A micro/mechanical analytical model, based on assuming a 2D crack of depth *a* at the free surface of an elastic-plastic half space, has been then employed in order to estimate the effective mode III SIF range. The effect of crack face friction, under both out-of-phase and torsional testing conditions, has also been quantified. The theoretical model of frictional interaction has shown that:

- the typical crack opening values caused by the out-of-phase loads prevent contact of the crack faces during the RCF load cycles. Consequently since there is no friction of the crack faces, the $\Delta K_{III,OOPth}$ measured actually corresponds to the effective threshold; such result was also confirmed by FE analysis on a pure elastic numerical model where a semi-circular crack in accordance with experimental evidence was introduced;
- torsional tests results are consistent with crack growth RCF data if the effective value of the stress intensity ΔK_{IIIeff} is used to characterize the mode III fracture behaviour.

Chapter 4

A model for crack sliding interaction under pure mode III and mixed-mode I+III loadings

4.1 Introduction

The effects of crack surface interaction are capital in the understanding of fatigue crack propagation promoted by shear. In the common fracture mechanics representation, cracks are modelled as discontinuities possessing smooth and frictionless surfaces. This assumption is quite satisfactory in mode I loading, where the crack experiences opening and closing phenomena at its tip, while it is misleading in mode II/III loadings, where the closed or partially closed cracks are displaced relatively to each other. Consequently frictional phenomena exist between the mating rough crack flanks under shear loading. The generally faceted crack surface morphology naturally arise in many polycrystalline and aggregate materials (i.e. metals, ceramic, concrete, brittle geo-materials as rock and bio-material as bones); however, the tortuous crack profile can also be attributed to oxide-built up on the crack plane [47].

Nevertheless, modelling analyses of fracture surface interference under simple mode III and mixed mode I/III fractures are not well-developed. In *chapter 3* an elastic-plastic partial slip frictional model, capable of estimating the effective crack driving force ΔK_{IIIeff} under anti-plane shear has been employed. In the mentioned model the contacting peaks and valleys of the microscopically rough crack surfaces interact over some extent of the edge crack, through a combination of sliding and sticking thereby causing the smearing of the roughness asperities. The applied stress intensity factor K_{III} is reduced by the frictional SIF K_f, engendered by the frictional shear stresses τ_f acting in opposition to the applied shear stresses and proportional to the contact pressure through the friction coefficient μ. When the effect of crack face friction was

taken into account, the theoretical modelling analysis supported the experimental findings (see the discussion in *chapter 3*).

Nevertheless, despite of the attractiveness of its simple mathematical framework, such model has some limitations: first, it can only be applied globally during a cycle (i.e. the calculation of the effective mode III SIF at each time step may not be achieved); second, the crack interaction occurs across the macroscopic plane and the stress transfer on the asperity slope is ignored. Because of the latter assumptions, the coupling between crack sliding and opening displacement (*dilatancy* phenomenon) is neglected and consequently, the effect of ΔK_I on the crack growth behaviour is not taken into account.

When crack fracture surfaces are displaced relative to one another, the roughness asperities are proposed to wedge the crack open. The produced dilatancy is resisted by normal contact stress which, in turn, are related to the frictional stresses through the Coulomb coefficient. The frictional stresses again act in opposition to the applied shear load.

Experimental evidence of fracture surface interference phenomenona is found in [48]: Goulet et al used a three-illumination beam, phase-shifted speckle interferometry to measure the shear and opening displacements fields around the tip of a mode I fatigue pre-crack subjected to remote shear loading.

A literary survey of the modelling analyses of fracture surface interaction, where the effect of dilatancy is taken into account, is provided in the following.

Furthermore, a model for crack sliding interaction under pure mode III and mixed mode I+III is developed. With respect to the modelling analysis developed in *chapter 3*, in the current theoretical study two aspects are well accounted for :

- the forward and backward sliding under cyclic loads;
- the coupling between the shear mode attenuation and the induced mode I stress intensities (dilatancy effect).

4.2 Modelling analyses of fracture surface interference: literary review

A few number of publications which include dilatancy in the analysis of crack surface interference is available in literature. In what follows a literature survey of crack surface interaction modelling under nominal mode I, mode II and mode III loadings is provided.

4.2.1 Modelling analysis of dilatancy for mode I cracks

The earliest attempts directed to consider the coupling between opening and sliding displacements, induced by the mismatch of faceted crack surfaces, have been done under dominantly plane strain mode I loading conditions. The first prominent analysis for fatigue crack closure, induced by fracture surface roughness, has to be attributed to Suresh and Ritchie [41]: in their quantitative study a two dimensional geometrical model, incorporating the contribution from both mode I and mode II crack tip displacements on fatigue crack closure, was proposed. The fracture roughness of the crack surfaces was simply idealized as saw-tooth rigid asperities roughly equal in size. On the other hand, Beevers et al [49] namely investigated the interaction effects of a single rigid asperity on the closure phenomena experienced at the crack tip. The slope of the asperity was assumed to be 90°. The single asperity model was successfully applied in order to investigate the effect of crack surface interference in nickel alloys and steels.

A mixed mode fatigue crack closure model was later proposed by Carlson and Beevers [50] in order examine the effect of the loading mixity on the conditions required for crack to branching. A crack with an inclined jog, situated at a discrete distance from the crack tip, was used to analyze the crack surface interference. The effect of friction was also included. The sketch adopted was suggested by the observation of the fatigue crack path revealed at high magnifications. A non proportional loading state at the crack tip was predicted by the theoretical study and the relevant role played by the local mode II loading on the conditions required for the promotion of crack branching was remarked.

4.2.2 Modelling analysis of dilatancy for mode II cracks

With respect to mode II loading, Ballarini and Plesha [51] examined the mechanism of sliding contact interaction onto a centre crack in an infinite medium under monotonic in-plane shear loading. The crack surfaces were assumed to be globally smooth and both the roughness and frictional effects were incorporated through a constitutive law. On the microscopic size scale, the roughness crack flanks was modelled as an evenly distributed saw-tooth asperity profile. However, although the model appears attractive from a mathematical point of view, its application is limited to simple geometries on account of the numerical problems encountered.

Furthermore, when the theoretical analysis of crack surface interference is developed under monotonic loading, it cannot be readily extended to cyclic loading conditions. Smith and Smith [52]-[53] cleared up the differences between the above testing conditions on the sliding interaction mechanism: when a shear crack is subjected to a monotonic loading, slip is unidirectional and only takes place on first loading; oppositely, under cyclic loading, slip is said to be reversed since it takes place during both loading and unloading within a cycle. According to Smith and Smith, three possible sources may contribute to the frictional attenuation during sliding interaction:

- the wedging open between asperities, revealed after the examinations of replicas;
- the extensive plastic deformation of interlocking asperities, detected by SEM observations of the fracture surfaces;
- the compressive residual stresses existing behind the crack tip.

Compressive stresses are proposed to be engendered by the plastic wake formed behind the crack tip during mode I pre-cracking. The frictional dissipation due to the compressive residual stresses was included in the theoretical model of Yu and Abel [54]-[55]. In their work, the sliding contact mechanism was investigated onto an infinite medium with a centre crack. The crack flanks roughness was again modelled as a uniform distribution of saw-tooth asperity. The residual stresses acting as

compressive stresses between the mating asperities, were proposed to be caused by plastic wakes, fretting debris and oxidation build-ups.

Tong et al [56] provided a theoretical modelling analysis of crack surface interference under both cyclic mode II and mixed I+II loadings. The sliding contact interaction mechanism within one facet was examined, after having assumed the shear displacements at the crack mouth small in comparison with the facet length. Geometrical relationships, for both backward and forward sliding contact, were provided for a variety of friction coefficients and inclinations angles. Satisfactory agreements with the experimental results were obtained by the authors.

Nevertheless, the crack surface roughness parameters, often assumed in the mentioned works, were not inferred by experimental measurements. A realistic representation of the rough profile was achieved by Mendelsohn et al [57]: the crack sliding contact behaviour was analyzed by digitalizing the randomly distributed roughness profiles of the mode I edge in modified compact tension specimens. The shear attenuation as well as the dilatancy phenomenon were predicted by adopting analytical laws correlating loads and displacements.

4.2.3 Modelling analysis of dilatancy for mode III cracks

With respect to mode III loading, theoretical studies including dilatancy are rare in literature. Only the extended work of Gross and Mendelsonh [58] is available under mode III testing conditions. Although the stress transfer was again assumed to occur on the macroscopic plane (as in the original work [44]), in the extended model the normal contact stresses were found by resolving the contact across the asperity and the mode I stress intensity, induced by the wedging open between the mating crack surfaces, was also calculated.

Gross and Mendelsonh employed the model with the aim of investigating the effect of loading mixity on stress corrosion cracking in Al alloys. Furthermore, experimental studies comparing the mode I and the mode III stress corrosion crack resistances in order to determine whether the stress corrosion crack growth is promoted by hydrogen enbrittlement or by anodic dissolution, were contradicted by the model due to the fact that a pure mode III condition cannot be achievable.

4.3 Proposed model

4.3.1 Characteristics and assumptions

A modified frictional analytical model, based on the original work of Tong et al [56] (developed under pure mode II and mixed mode I+II testing conditions) is now presented.

The modelling analysis is again performed assuming a 2D crack of depth *a* at the free surface of an elastic-plastic half space (Figure 4.1), where the total crack depth *a* is given by the sum of both the notch and the pre-crack length. Three-dimensional effects are neglected for the reasons already mentioned in *chapter 3*. The notch is considered to be frictionless and the problem is treated as a partially-loaded edge crack in a semi-infinite plate. The crack surface irregularities are assumed to be evenly distributed saw-tooth rigid asperities with Coulomb friction at the asperities facets.

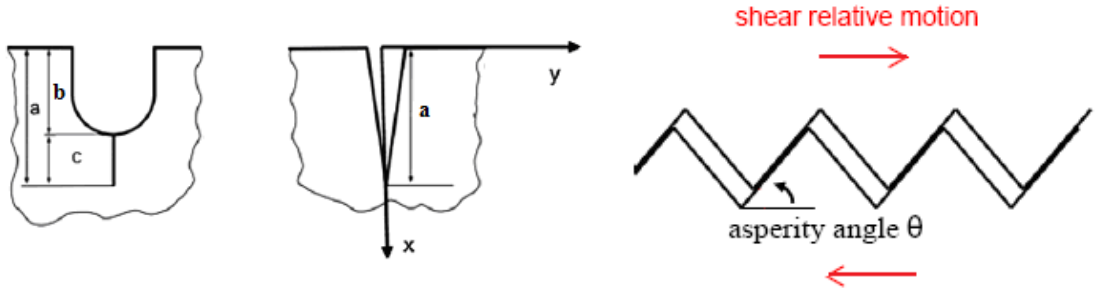

Figure 4.1. a) Schematic of the 2D simplification for shallow notch + pre-crack; b) rigid saw-tooth asperity profile.

With respect to the work of Tong et al [56], where the crystallographic feature θ was a hypothesized from the knowledge of microstructure, in the current study the slope of the asperity has been estimated on the basis of the real crack profile, it was indeed derived from experimental roughness measurements (see *chapter 5*).

Moreover, the left- and right-hand-side facet angles are hypothesized to be equal.

The plastic deformation and the wearing degradation of the asperities are not considered in the modelling analysis.

4.3.2 Formulation of the model

The shear attenuation is proposed to be only related to the normal contact stresses arising on account of the crack flanks wedging open over surface irregularities. Crack surface interference can be described by means of displacement and force restrictions, consistently with Elber's original modelling of fatigue crack closure phenomenon [59]. The coupling between the normal and the tangential components of the effective displacements at the position *x* along the crack length is expressed by:

$$2u_{I,eff}(x) = \xi \cdot \tan\theta \cdot 2u_{III,eff}(x) \tag{4.1}$$

The factor 2 accounts for the total displacement between the opposing crack surfaces, since *u* is measured with respect to the middle plane of the crack. The constant ξ corresponds to ξ=-1 or to ξ=+1 when the asperity interaction occurs at the left-hand (i.e. reversed loading) or right-hand facet respectively. Eq. (4.1) is valid when the shear displacement are small in comparison to the facet length and slip is then confined within one facet. For the model to be applicable the mating crack surfaces should always be in contact; in order to ensure this condition is fulfilled, it is sufficient to ensure that the nominal mode I and mode III displacements ($u_{I,0}$ and $u_{III,0}$ respectively) satisfy the following geometrical restriction:

$$\frac{2u_{I0}(x)}{2u_{III0}(x)} \le \xi \tan\theta \tag{4.2}$$

Under mixed-mode I+III loadings the nominal mode I displacement is enhanced by an additional component due to wedging, while under pure mode III loading $u_{I,eff}$ is simply the mode I wedging displacement. On the other hand, the effective sliding displacement $u_{III,eff}$, is always the nominal shear displacement reduced by the frictional tangential displacement whatever the testing condition:

$$2u_{I,eff}(x) = 2u_{I0}(x) + 2u_{hw}(x) \tag{4.3}$$

$$2u_{III,eff}(x) = 2u_{III0}(x) - 2u_{IIIf}(x) \tag{4.4}$$

The mode I wedging $u_{I,w}$/mode III frictional displacements $u_{III,f}$ are due to the normal contact/ frictional stresses which may arise due to the interaction between the rough crack flanks. The mode I and mode III crack displacements due to an arbitrary normal and tangential stress distribution, i.e. $p(x)$ and $q_f(x)$ respectively, applied between the notch depth b and the crack tip a (see Figure 4.1) can be calculated by:

$$2u_{Iw}(x) = \frac{8}{\pi E'} \int_x^a \int_b^s \frac{g_I\left(x/s\right)}{s \cdot \sqrt{1-\left(x/s\right)^2}} \cdot \frac{g_I\left(\zeta/s\right)}{\sqrt{1-\left(\zeta/s\right)^2}} p(\zeta) d\zeta ds \tag{4.5}$$

$$2u_{IIIf}(x) = \frac{4}{\pi G} \int_x^a \int_b^s \frac{q_f(\zeta)}{s \cdot \sqrt{1-\left(x/s\right)^2} \cdot \sqrt{1-\left(\zeta/s\right)^2}} d\zeta ds \tag{4.6}$$

where $E' = E/(1-\nu^2)$; E and G are the Young's and the shear Modulus, ν is the Poisson's ratio and [60]:

$$\begin{aligned} g_I\left(x/a\right) = 1 + \left(1-\left(x/a\right)^2\right)\Big(0.2945 - 0.3912\left(x/a\right)^2 \\ + 0.7685\left(x/a\right)^4 - 0.9942\left(x/a\right)^6 + 0.5094\left(x/a\right)^8\Big) \end{aligned} \tag{4.7}$$

Similarly, the nominal mode I and mode III displacements (u_{I0} and u_{III0} respectively) can be calculated by applying the weight function method for an edge crack in a semi-infinite plate subjected to a uniform stress distribution along its length, i.e.

$$2u_{I0}(x) = \frac{8\sigma_\infty}{\pi E'} \int_x^a \int_0^s \frac{g_I\left(x/s\right)}{s \cdot \sqrt{1-\left(x/s\right)^2}} \cdot \frac{g_I\left(\zeta/s\right)}{\sqrt{1-\left(\zeta/s\right)^2}} d\zeta ds \tag{4.8}$$

$$2u_{III0}(x) = \frac{4\tau_\infty}{\pi G}\int_x^a \int_0^s \frac{1}{s\cdot\sqrt{1-\left(x/s\right)^2}\cdot\sqrt{1-\left(\zeta/s\right)^2}} d\zeta\, ds \tag{4.9}$$

Possible crack flanks contact pressure distribution are depicted in Figure 4.2. In Figure 4.2a it is assumed that the contact pressure varies linearly from the maximum at the crack tip ($x = a$) to zero at the notch depth ($x = b$); the maximum pressure is equal to or less than the material yield stress, σ_y. When the maximum pressure exceeds the yield stress the contact stresses distribution is assumed to be that of Figure 4.2b: in this case the pressure is constant and equal to σ_y from the crack tip to a point $x = x_1$, then it decreases linearly to zero until the notch depth is approached. When $x_1 = b$ a uniform contact pressure distribution equal to the material yield stress is assumed.

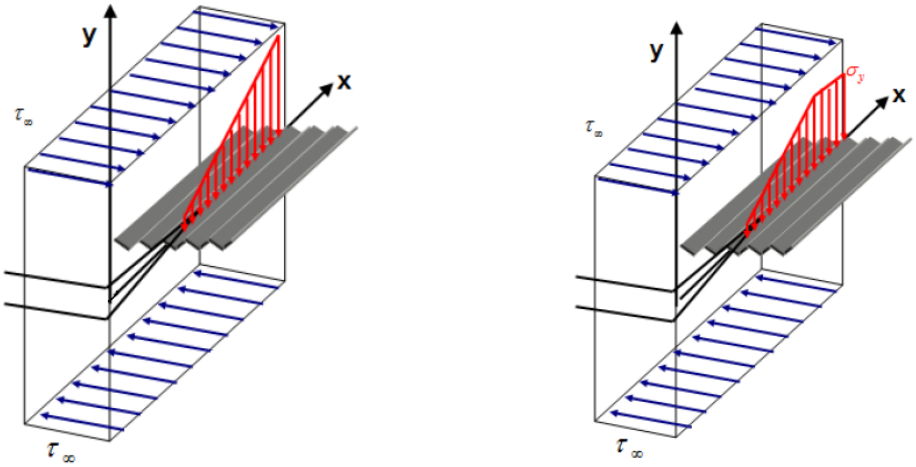

Figure 4.2. Possible contact pressure distribution profiles between the mating fracture surfaces arising from the crack surface interaction: a) linear distribution, b) elastic-plastic distribution.

With respect to original model of Tong et al [56], where a linear distribution for the contact stresses was only hypothesized, in the current work a perfect plasticity assumption has been employed in order to constraint the maximum value of the stress at the crack tip.

The normal force N and the friction force F are related by the Coulomb friction law; under limiting friction condition, if α is the friction angle (see Figure 4.3), the normal and tangential interaction forces relationship is expressed by:

$$\mu = \tan\alpha = \frac{F}{N} \tag{4.10}$$

For the different movement situations (Figure 4.3), i.e. uphill and downhill sliding, the resolved components of the resultant interaction force along the vertical and horizontal directions, P and Q respectively, are geometrically related by the following equation:

$$Q = P \cdot \tan\left(\theta + \chi\alpha\right) \tag{4.11}$$

where the constant χ corresponds to χ=+1 and to χ=-1 for uphill and downhill sliding respectively.

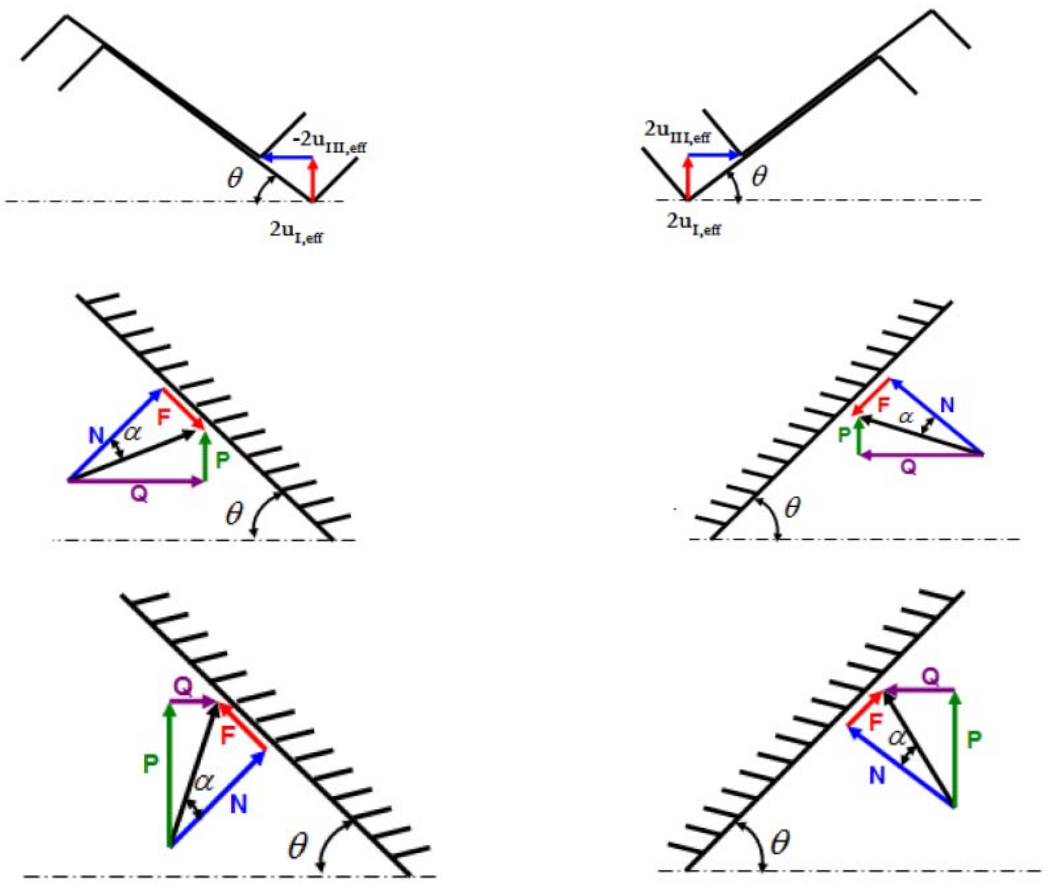

Figure 4.3. a) displacements coupling for crack surface contact at left-hand and right-hand facet; crack surface interaction during uphill b) and downhill c) sliding at left-hand and right-hand facet contact.

Furthermore, it should be remarked that with respect to the work of Tong et al [56], the current model is extended to deal with two-sided facet interference. The system of Eqs. (4.1)-(4.11) can be solved simultaneously to give a compatible set of crack-surface interference stresses and displacements.

Upon converge the effective tangential displacements $u_{III,eff}$ and the mode I wedging $u_{I,w}$ displacements at the end of the physical crack length ($x = b$) can be expressed by:

$$2u_{Iw}\left(x=b\right)=\frac{1}{1+C\tan\left(\theta+\chi\alpha\right)\tan\theta}\left(\xi\cdot 2u_{III0}\left(x=b\right)\tan\theta-2u_{I0}\left(x=b\right)\right) \tag{4.12}$$

$$\begin{aligned}2u_{IIIeff}\left(x=b\right)=&\frac{1}{1+C\tan\left(\theta+\chi\alpha\right)\tan\theta}2u_{III0}\left(x=b\right)+\\&+\ \xi\frac{C\tan\left(\theta+\chi\alpha\right)}{1+C\tan\left(\theta+\chi\alpha\right)\tan\theta}2u_{I0}\left(x=b\right)\end{aligned} \tag{4.13}$$

The constant C is expressed by Eq. (4.14), where h_{III} (b/a) and h_I (b/a) are respectively the geometric factors for mode III and mode I displacements for a partially loaded edge crack in a semi-infinite plate [39] subjected to a linear stress distribution.

$$C=\frac{E'}{G}\frac{h_{III}\left(b/a\right)}{h_I\left(b/a\right)} \tag{4.14}$$

The integrated results for h_{III} (b/a) and h_I (b/a) are shown in Figure 4.4 while their analytical formulation is expressed by:

$$2u_{Iw}\left(x=b\right)=\frac{4a}{\pi E'}h_I\left(b/a\right)p\left(x=a\right) \tag{4.15}$$

$$2u_{IIIf}\left(x=b\right)=\frac{4a}{\pi G}h_{III}\left(b/a\right)q_f\left(x=a\right) \tag{4.16}$$

Further details about the closed-form solutions of the crack surface displacements, due to the interaction between the mating asperities, can be found in *Appendix B*.

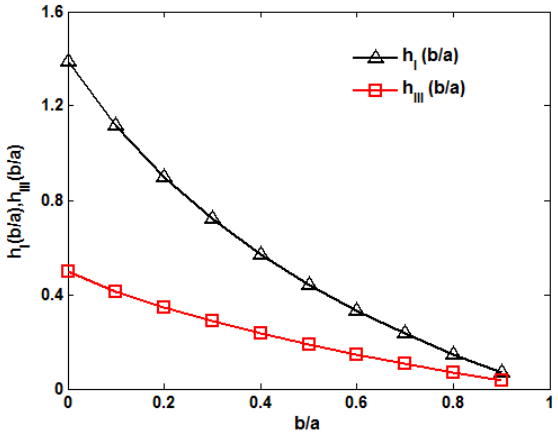

Figure 4.4. Geometry factors for displacements for a partially loaded edge crack in a semi-infinite plate.

Once the wedging displacement at the notch depth is known (Eq. (4.12)), the normal contact stresses can be calculated from Eq. (4.5), after having assumed the possible pressure distribution. A linear stress distribution is first assumed, if the maximum pressure at the crack tip *p(x=a)*, calculated by Eq. (4.15), exceeds the material yield strength the elastic plastic-distribution is then assumed.

Once the normal contact stresses are known, the frictional shear stresses can be calculated by Eq. (4.11). The partially loaded distributed normal and tangential stresses, due to local wedging and frictional sliding, integrated on the edge crack, produce a mode I wedging and a mode III frictional stress intensity factors, i.e. K_{Iw} and K_{IIIf} respectively:

$$K_{Iw} = \frac{2}{\sqrt{\pi a}} \int_b^a \frac{g_I\left(x/a\right)}{\sqrt{1-\left(x/a\right)^2}} \cdot p\left(x\right) dx \tag{4.17}$$

$$K_{IIIf} = \frac{2}{\sqrt{\pi a}} \int_b^a \frac{1}{\sqrt{1-\left(x/a\right)^2}} \cdot q_f\left(x\right) dx \tag{4.18}$$

where $g_I(x/a)$ is expressed by Eq. (4.7).

The effective mode I and mode III stress intensities, at each time step during the loading cycle, are thereby obtained:

$$K_{I,eff}(t) = K_{I0}(t) + K_{Iw}(t) \tag{4.19}$$

$$K_{III,eff}(t) = K_{III0}(t) - K_{IIIf}(t) \tag{4.20}$$

where K_{I0} and K_{III0} are the applied mode I and mode III stress intensity factors respectively. Once again the nominal SIFs can be calculated by applying the WF method:

$$K_{I0} = \frac{2\sigma_\infty}{\sqrt{\pi a}} \int_0^a \frac{g_I\left(x/a\right)}{\sqrt{1-\left(x/a\right)^2}} dx \tag{4.21}$$

$$K_{III0} = \frac{2\tau_\infty}{\sqrt{\pi a}} \int_0^a \frac{1}{\sqrt{1-\left(x/a\right)^2}} dx \tag{4.22}$$

4.4 Model behaviour under pure mode III loading: locking and unlocking mechanisms

Although the analytical formulation of the model has been presented for a general mixed-mode (I+III) loading condition, it can be easily simplified in order to analyze the crack surface interference under anti-plane shear. For the sake of simplicity, the model behaviour is now discussed under pure mode III testing condition. A discussion of the model response under mixed-loading would lose generality since the crack sliding interaction under biaxial testing condition depends on the load mixity [23].

The key of understanding of the model response can be found in the locking/unlocking behaviour of the mating asperities engendered by the cyclic shear displacements. According to the definitions given in [52], the terminology used in the current modelling analysis of crack surface interference under shear is recalled:

- a crack is said to be "*slipped*" at any point if mode III displacements are present; if slip does not reach the tip a partially slipped condition is assumed;

– a crack is said to be "*unlocked*" at any point if its flanks are free to slide over one another as the load is changed; a mathematical definition of locking is the following $\partial(2u_{III0})/\ \partial\tau_{\infty} \neq 0$. Unlocking may be partial or full along the crack length in the same manner of slip.

The locking/unlocking behaviour can be analysed thorugh the trend of the effective mode III displacement $2u_{IIIeff}$ at a point along the crack flank. Figure 4.5 shows a schematic of the variations of nominal and effective mode III displacements during the a fatigue cycle at R = -1. A negative stress ratio is assumed in the theoretical discussion since negative ratios are more damaging than positive fatigue ratios [23].

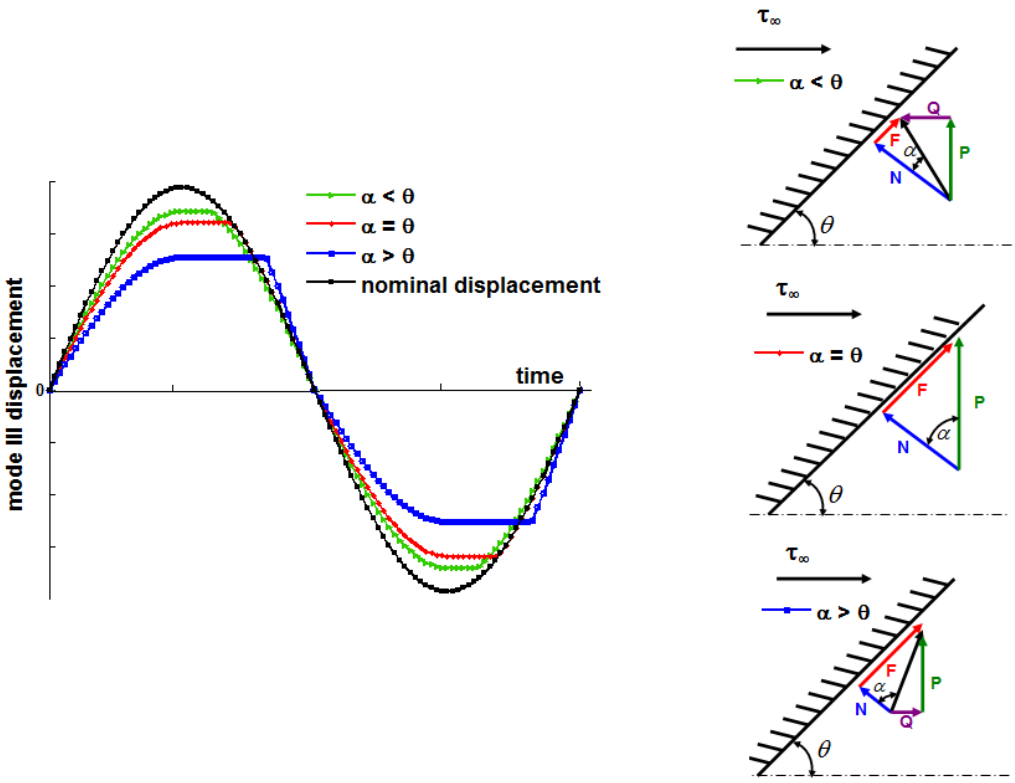

Figure 4.5. Schematic of variations of nominal and effective mode III displacements during a fully reversed mode III fatigue cycle.

The influence of both the friction and asperity angle (i.e. α and θ respectively) on the effective mode III cyclic displacements variation is also revealed. The shape of $2u_{IIIeff}$ trend depends on the geometrical relationship between the horizontal and vertical

components of the resultant interaction force (provided by Eq. (4.11)). A geometric illustration of the normal and friction forces decomposition during downhill sliding at right-hand facet is shown as example.

During loading the local tangential force increase whatever the friction and the asperity angle values; upon unloading, in stead, the horizontal component of the interaction force varies as follows:

- when $\alpha > \theta$, an increase is observed;
- when $\alpha = \theta$, no variations are observed;
- when $\alpha < \theta$, a decrease is observed.

Furthermore, during loading the crack is fully unlocked till its tip, at load reversal (both at maximum and minimum load) the crack is fully locked: locking takes place due to the fact that upon unloading, the frictional shear stresses should resist to slip in the unloading direction as well as to the limiting frictional stresses developed in the slipped region of the crack at the maximum/minimum load. Unlocking, which spreads progressively from the notch to the crack tip, would not take place until the reduction in the applied load is such that the effective shear displacement is equal to the maximum value of $2u_{III\,eff}$ during the loading phase (i.e. $2u_{III\,eff}$ at the maximum/minimum load).

Accordingly, during a cycle the current effective crack tip at each time step would be interpreted as the boundary between the locked and unlocked regions of the crack: ahead of the effective crack tip the crack faces are locked, while behind it the crack faces are unlocked with the possibility to slide over one another.

The “locking” and “unlocking” mechanism experienced by the crack during a fully reversed pure mode III cycle is qualitatively depicted in Figure 4.6.

During loading (i.e. loading and reversed loading), the crack is fully locked and the effective crack tip corresponds to the physical crack tip; on the other hand, during unloading (i.e. unloading and reversed loading), the crack is partially locked and the effective crack tip gradually moves from the notch depth to the crack tip.

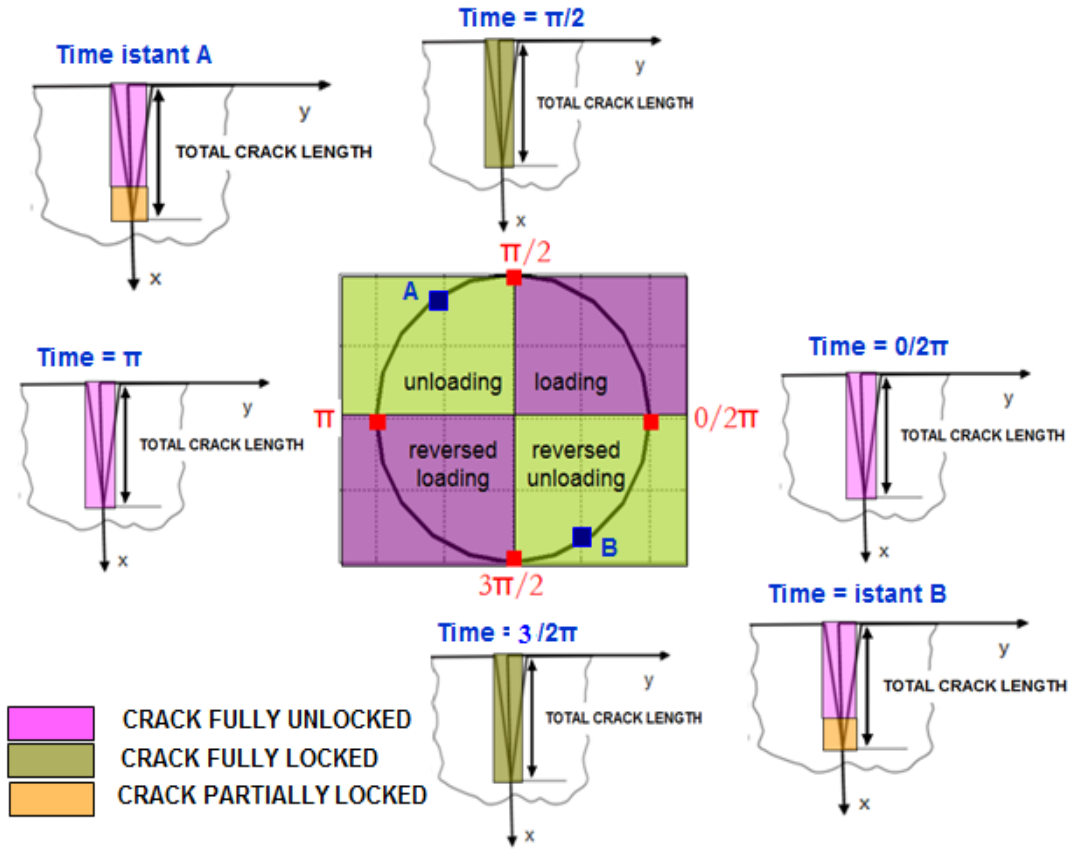

Figure 4.6. Locking and unlocking mechanism experienced by the crack tip during a fully reversed mode III loading cycle.

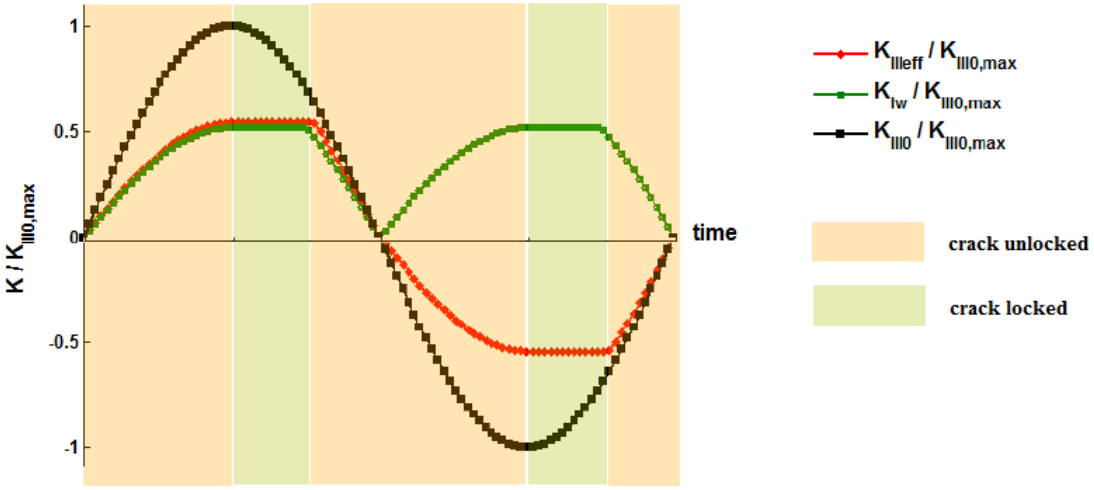

Figure 4.7. Schematic of the variation of the stress intensities during a fully reversed torsional loading cycle.

Finally a schematic of the variation of the nominal and effective mode III stress intensities together with the trend of the induced mode I SIF are reported in Figure

4.7. A friction angle lower than the asperity angle ($\alpha < \theta$) is assumed for the qualitative representations of the SIFs. Results are normalized with respect to the maximum value of the applied mode III stress intensity factor $K_{III0,max}$.

Following the observations of the SIFs qualitative variation during the torsional loading cycle, it appears evident that a pure applied mode III loading may never be achieved in practise: the crack tip actually experiences a mixed-mode (I/III) loading condition and the contribution of the induced mode I stress intensity can be comparable to that of the effective mode III stress intensity.

4.5 Conclusions

In the present chapter a physical model has been proposed in order to quantify the effect of crack surface interaction due to the crack flanks roughness under pure mode III and mixed I+III loadings. The model, based on the original work of Tong et al [56], assumes a 2D crack of depth *a* at the free surface of an elastic-plastic half space, where the total crack depth *a* is given by the sum of the notch and the pre-crack length. The notch is considered to be frictionless and the problem is treated as a partially-loaded edge crack in a semi-infinite plate. The crack surface irregularities are assumed to be evenly distributed saw-tooth rigid asperities with Coulomb friction at the asperities facets. The physical parameter used to describe rough fracture surface is the slope of the asperity, which is derived from experimental roughness measurements.

Unlike the simple theoretical model employed in *chapter 3*, capable of estimating the effective mode III SIF range globally during a cycle, the proposed modelling analysis also takes into account the coupling between crack sliding and opening displacements (*dilatancy* phenomenon) engendered by the rough crack surfaces sliding. The crack surface wedging open over asperities both generates a positive mode I stress intensity at the crack tip and resisting normal contact stresses, which in turn give rise to shear attenuation.

According to the theoretical modelling analysis, the sliding interaction between faceted crack flanks can significantly affect the loading mixity at the crack tip, thereby suggesting that the effective crack tip stress field may not be evaluated on the basis of

the external loading only. Furthermore, the model has shown that a pure mode III loading condition may not be achievable in practise.

The model behaviour under simple shear has been discussed and the locking/ unlocking at load reversals were found to be fundamental in the understanding of the mechanism of sliding interaction between the rough crack surfaces.

Applications of the model will be provided in *chapter 5*.

Chapter 5

Competition between mode I and mode III failures under simple shear and RCF conditions

5.1 Introduction

Fracture and fatigue crack path under both pure mode III and mixed mode I+III loadings are essentially dictated by the loading mixity at the crack tip as well as by the material itself. The macroscopic appearance of the fracture surfaces is established by the cracking mode dominating the competition between mode I and mode III failures. Both tensile and shear propagation modes encourage the crack growth under fatigue torsional loading [61]. A transition form a shear- (macroscopically flat fracture surface) to a tensile-dominated (i.e. "factory roof") fracture was observed by Tschegg [26] during crack propagation. Besides the loading mixity at the crack tip, the fracture mode is also affected by the applied loading amplitude: according to Tschegg experiments, at low nominal ΔK_{III} a tensile propagation mode dictates the crack growth and the macroscopic fracture appearance resembles a "factory roof"; on the other hand, at high ΔK_{III} the propagation is promoted by shear and the sliding interaction between the crack surfaces flattens the fracture surface.

The conditions governing the onset of crack branching depend on the effective crack tip stress field, which cannot be evaluated on the basis of the external loading only. According to the theoretical discussion developed in *chapter 4*, the crack sliding contact interaction is proposed to be responsible for both the shear attenuation (i.e. the mode III SIF reduction to a lower effective value) and the wedging open behaviour of the crack surface asperities (.i.e. the generation of a positive mode I SIF).

In this chapter an attempt is done in order to analyze the conditions required for the promotion of mode I/mode III crack branching. A theoretical discussion on the macroscopic fracture modes, which characterize failures under rolling contact and pure torsional testing conditions, has been carried out. The current study is supported

by the exploitation of the model for crack sliding interaction developed in *chapter 4* and the competition between mode I and mode III dominated failures has been theoretically examined in terms of mode I and mode III branch SIFs.
Furthermore, new experimental tests have been carried out with the aim of deeply understanding the physics of the complex mechanism of crack growth encouraged by shear when the axial loading, superimposed to the alternating torsion, is partly in tension partly in compression.

5.2 New experimental fatigue tests

In order to make a clear distinction between the multiaxial load path, adopted for the new experimental fatigue tests, and the out-of-phase load pattern (*chapter 2*), the following caption is used: "load path 1" will refer to the out-of-phase testing condition and "load path 2" will refer to the new load pattern scheme.

5.2.1 Fatigue test procedure

All fatigue tests have been carried out on pre-cracked micro-notched hourglass specimens. A defect size, expressed in terms of Murakami's √area parameter, equal to 315 μm, has been considered. The bearing steel specimens geometry and micro-notch adopted have already been reported in *chapter 2*. In order to promote co-planar crack propagation, a preliminary mode I fatigue test pre-cracking procedure was again adopted (all specimens were subject to push-pull axial fatigue for 10^7 cycles at R = -1 at a stress level close to ΔK_{Ith}). The tests were conducted in force/torque control by means of a MTS 809 Axial Torsional Systemat a frequency of 1 Hz. The load pattern, supplied by SKF and consisting of an alternating torsion with the superimposition of an axial loading, simulates the stress state experienced by an inclined sub-surface crack under contact loads. The shape of the axial loading differs from the one adopted in the out-of-phase scheme: firstly, the nominal mode I loading is party in tension partly in compression; secondly, the absolute value of the minimum compression is much lower than the one assumed in load path 1. While in the load path 1 the ratio σ_{min}/τ_{max} was almost equal to $\sigma_{min}/\tau_{max} = -3.5$, in load path 2 the same ratio is equal to

σ_{min}/τ_{max} = -0.7 (about five times less than in the OOP scheme). The load path 2 is depicted in Figure 5.1.

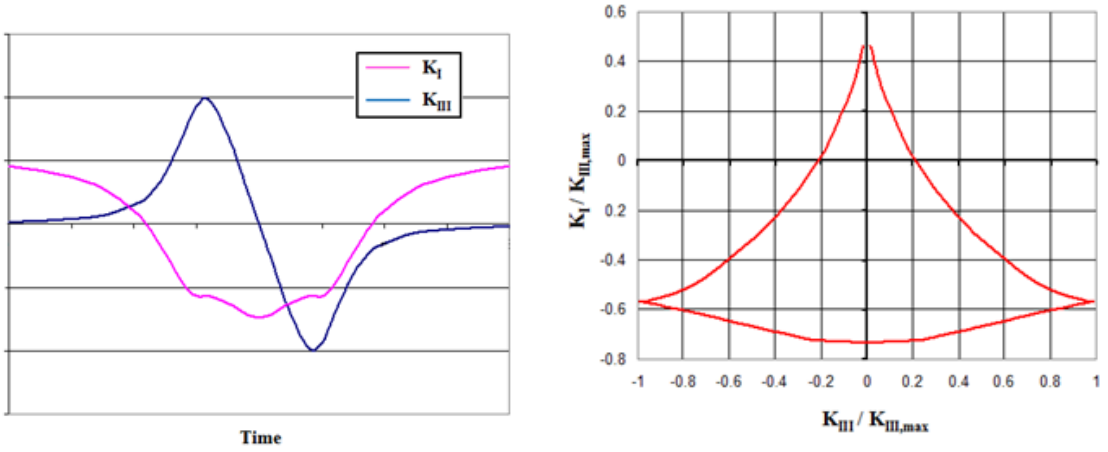

Figure 5.1. Load pattern scheme (load path 2) adopted for multiaxial fatigue tests.

Multiaxial fatigue tests were interrupted on the basis of the maximum surface crack length measurements (a_s<1 mm) otherwise in according to the number of fatigue cycles ($N_f = 2 \cdot 10^6$), if the near threshold crack propagation behaviour was of interest.

5.2.2 Fatigue test results

Fatigue test results are now presented by describing the main features of their experimental fracture surfaces observed from fractographies. Particular attention has been deserved to the macroscopic appearance of the fracture surfaces. Furthermore, the transition, eventually occurring, from a tortuous crack surface (characterized by a non-planar crack front, often rotated and segmented, i.e. “factory roof”) to a planar, completely flat, crack surface has been also inspected.

Following an examination of fatigue test results, it appears that the fracture surfaces of both load path 1 and load path 2 samples do not resemble each others; while many similarities can be found between load path 2 and torsional crack appearance.

A comparison between the mode III fracture surfaces for both the two multiaxial loading paths is depicted in Figure 5.2: when the new load path is adopted, a slender

mode III propagation could be observed in contrast with the enhanced coplanar crack growth promoted by the out-of-phase scheme.

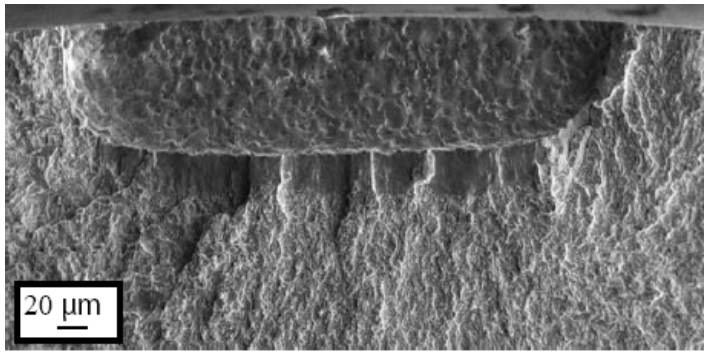

a)

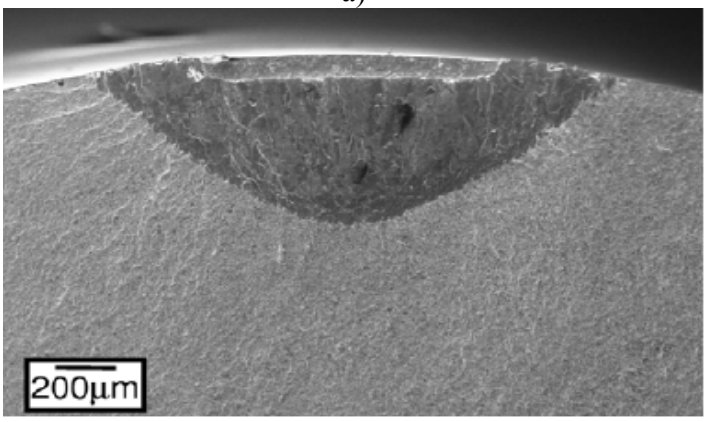

b)

Figure 5.2. Comparison of mode III fracture surfaces (micro-notch √area = 315µm) obtained under the two multiaxial load patterns: a) specimen tested at $\Delta K_{III}/\Delta K_{Ith} = 1.2$ for N = 8 x 10^4 cycles with load path 2; b) specimen tested $\Delta K_{III}/\Delta K_{Ith} = 1.3$ for N = 2.5 x 10^4 cycles with load path 1.

Moreover, load path 2 failures always occurred on tilted 45° degrees planes nucleated along thin shear cracks at the bottom of the micro-notches and a "factory roof" morphology could also observed; the FR appearance is caused by mode I crack branching formed from small semi-elliptical crack nucleated at the initial crack front by shear [28], see Figure 5.3.

From the defect top view only the development of mode I kinked crack can be noted (Figure 5.3 and Figure 5.4) and the critical applied mode III range of stress intensity factor value, which could be pointed out as the boundary value between a 'discontinuous' and a 'continuous' crack propagation regimes, is actually higher than ΔK_{Ith} (Figure 5.3). Unlike in the case of torsional loading where the nominal mode III

threshold ΔK_{IIIth}, corresponding to a 'discontinuous' co-planar crack, was very close to $\Delta K_{Ith,}$ for the load path 2 the onset and a stable mode III coplanar propagation were observed at $\Delta K_{III}/\Delta K_{th,I}$ = 1.4 (Figure 5.3) and at $\Delta K_{III}/\Delta K_{th,I}$ = 1.6 (Figure 5.4) respectively. Furthermore, mode I surface propagation remains faster.

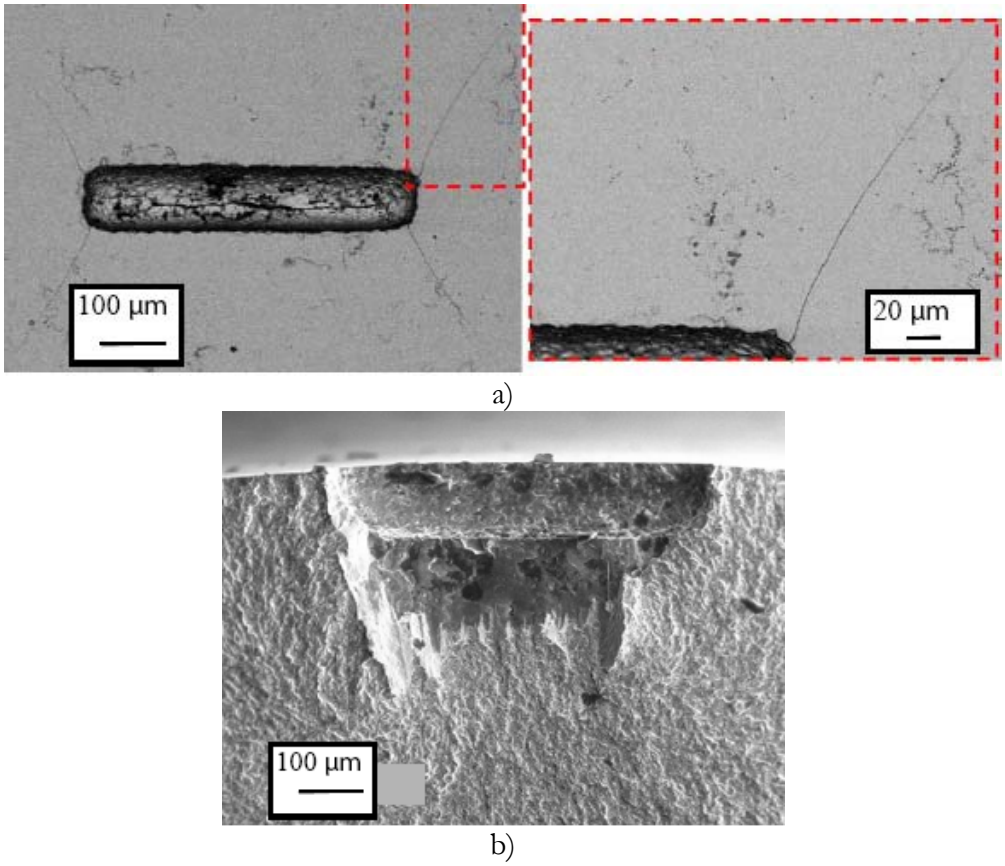

Figure 5.3. Fractographs of load path 2 micro-notched sample (√area = 315µm) tested at $\Delta K_{III}/\Delta K_{Ith}$ = 1.4, test interrupted at N = 5 x 10^4 cycles at : a) top view and b) 90° tilted view.

After the examination of load path 2 test results, a role of the far field compression can be assessed in the promotion of co-planar crack propagation since the differences between load path 1 and load path 2 fracture modes, could be solely attributed to the mode I loading superimposed to the alternating torsion.

Anyway, the role played by the far-field cyclic compression under rolling contact fatigue testing conditions will be deeply investigated and discussed in *chapter 6*.

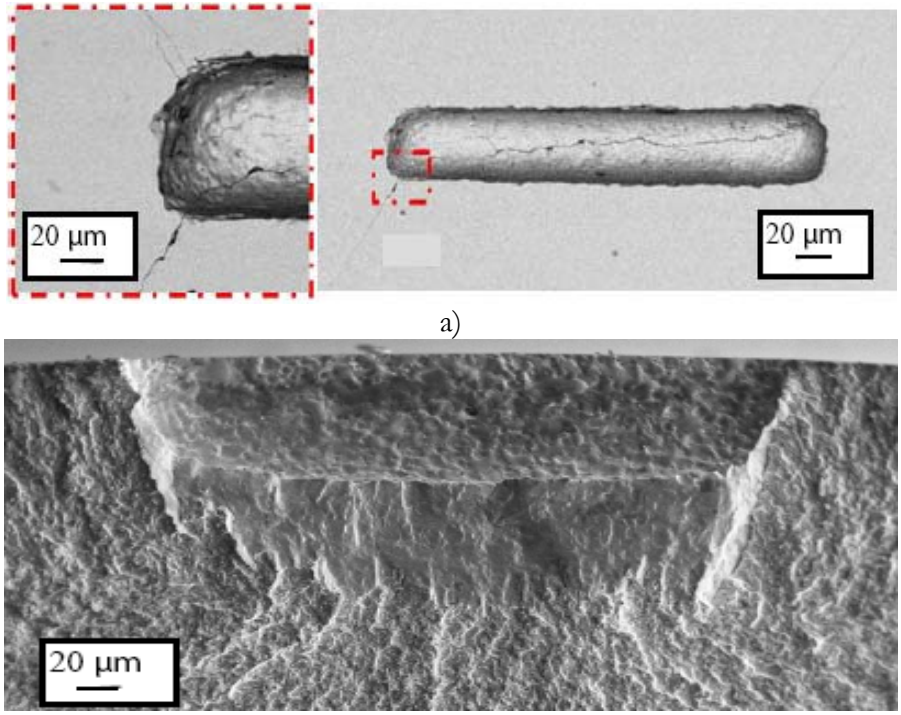

Figure 5.4. Fractographs of load path 2 micro-notched sample (√area = 315µm) tested at $\Delta K_{III}/\Delta K_{Ith}$ = 1.6, test interrupted at N = 2.5 x 10^4 cycles at : a) top view and b) 90° tilted view.

5.3 Competition between mode I and mode III fracture modes: a LEFM approach

The experimental fracture surfaces, observed from fractographies, can be classified into two distinctive macroscopical fracture types: '*tensile (mode I) type*' and '*shear (mode III) type'*.

The appearance of a *tensile type* (mode I-dominated) fracture is typically a non-flat fracture surface: the fracture surface morphology has three dimensional macro-structures almost regularly spaced around the crack front. This type of fracture is observed under both pure torsional and load path 2 testing conditions. On the other side, the appearance of a *shear type* (mode III-dominated) fracture is typically a flat fracture surface with evidence of shear rubbing marks: such type of fracture is observed under out-of-phase loadings.

The competition between the two failure modes (mode I vs. mode III) has been analyzed by adopting a LEFM approach: both the torsional and the multiaxial (load

paths 1 and 2) patterns have been examined in terms of local mode I and mode III branch stress intensity factors. The basis for the calculation is the near-field solution for stress distribution at the crack front [62]:

$$\begin{cases} \sigma_r = \dfrac{K_I}{4\sqrt{2\pi r}}\left[5\cos\left(\dfrac{\varphi}{2}\right)-\cos\left(\dfrac{3\varphi}{2}\right)\right]-\dfrac{K_{II}}{4\sqrt{2\pi r}}\left[5\sin\left(\dfrac{\varphi}{2}\right)-3\sin\left(\dfrac{3\varphi}{2}\right)\right] \\ \sigma_\varphi = \dfrac{K_I}{4\sqrt{2\pi r}}\left[3\cos\left(\dfrac{\varphi}{2}\right)+\cos\left(\dfrac{3\varphi}{2}\right)\right]-\dfrac{K_{II}}{4\sqrt{2\pi r}}\left[3\sin\left(\dfrac{\varphi}{2}\right)+3\sin\left(\dfrac{3\varphi}{2}\right)\right] \\ \sigma_z = \nu\left(\sigma_r+\sigma_\varphi\right) = \dfrac{8\nu}{4\sqrt{2\pi r}}\left[K_I\cos\left(\dfrac{\varphi}{2}\right)-K_{II}\sin\left(\dfrac{\varphi}{2}\right)\right] \\ \tau_{r\varphi} = \dfrac{K_I}{4\sqrt{2\pi r}}\left[\sin\left(\dfrac{\varphi}{2}\right)+\sin\left(\dfrac{3\varphi}{2}\right)\right]+\dfrac{K_{II}}{4\sqrt{2\pi r}}\left[\cos\left(\dfrac{\varphi}{2}\right)-3\cos\left(\dfrac{3\varphi}{2}\right)\right] \\ \tau_{rz} = \dfrac{K_{III}}{\sqrt{2\pi r}}\sin\left(\dfrac{\varphi}{2}\right) \\ \tau_{\varphi z} = \dfrac{K_{III}}{\sqrt{2\pi r}}\cos\left(\dfrac{\varphi}{2}\right) \end{cases} \tag{5.1}$$

All those stress field equations (Eq. (5.1)) are expressed as a function of the cylindrical coordinates system, i.e. *r*, *φ*, and *z*.

Resolving the stress state onto a twisted plane, identified by an angle ψ (see Figure 5.5), the mode I and mode III branch crack stress intensity factors have been obtained by multiplying the tensile $\sigma_{\varphi'}$ and the shear $\tau_{\varphi' z'}$ stresses, near the tip of a branch crack by $(2\pi r)^{0.5}$:

$$\begin{cases} k_I(\varphi,\psi,t) = K_I(t)\left[\cos^3\left(\dfrac{\varphi}{2}\right)\cos^2(\psi)+2\nu\cos\left(\dfrac{\varphi}{2}\right)\sin^2(\psi)\right]+ \\ \qquad -K_{III}(t)\cos\left(\dfrac{\varphi}{2}\right)\sin(2\psi) \\ k_{III}(\varphi,\psi,t) = K_I(t)\left[\dfrac{1}{2}\cos^3\left(\dfrac{\varphi}{2}\right)\sin(2\psi)-\nu\cos\left(\dfrac{\varphi}{2}\right)\sin(2\psi)\right]+ \\ \qquad +K_{III}(t)\cos\left(\dfrac{\varphi}{2}\right)\cos(2\psi) \end{cases} \tag{5.2}$$

where K_I and K_{III} are the nominal stress intensity factors calculated assuming a small 20 μm crack at the bottom of the micro-notch (i.e. the mode I pre-crack).

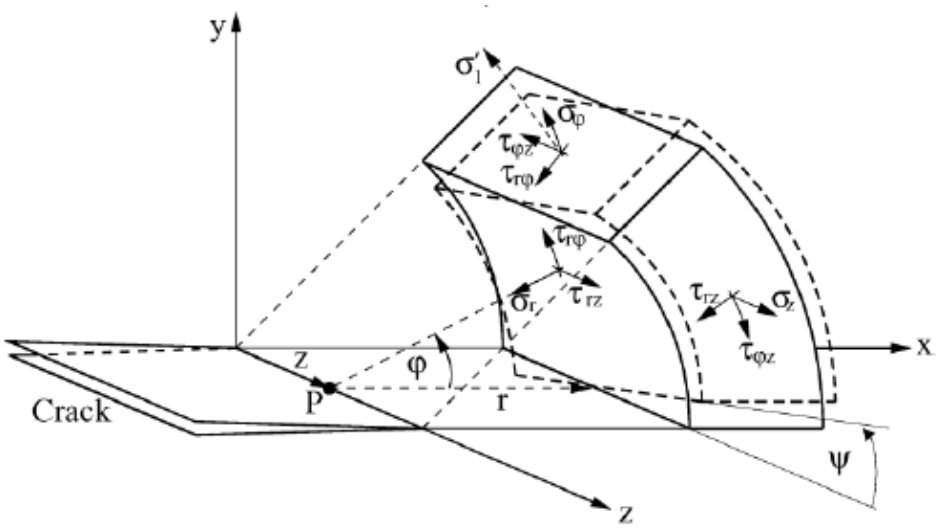

Figure 5.5. Cylindrical coordinate system [62].

At each step of the loading cycle, the maximum value of both mode I and mode III branch crack stress intensity factor are found by maximizing the analytical expression of $k_I(\varphi,\psi)$ and $k_{III}(\varphi,\psi)$ with respect to the angles φ and ψ, i.e. :

$$\begin{aligned} k_{I,max}(t) &= \max_{(\varphi,\psi)}\left(k_I(\varphi,\psi,t)\right) \\ k_{III,max}(t) &= \max_{(\varphi,\psi)}\left(k_{III}(\varphi,\psi,t)\right) \end{aligned} \tag{5.3}$$

The competition between mode I and mode III fracture modes at applied stress levels, where the onset of co-planar crack growth is observed, has been examined: samples tested at $\Delta K_{III}/\Delta K_{th,I}$ where the onset/the absence of mode co-planar propagation is observed (i.e. "growth"/"no-growth" sample) were then considered. Results, normalized with respect to the maximum value of the mode I threshold $K_{Ith,MAX}$ for short cracks, are shown trough Figure 5.6 to Figure 5.8. In the case of OOP and torsional loadings, the biggest size of the micro-notch (√area 630 μm) has been considered, nevertheless similar results could be obtained for micro-notch size √area = 220μm.

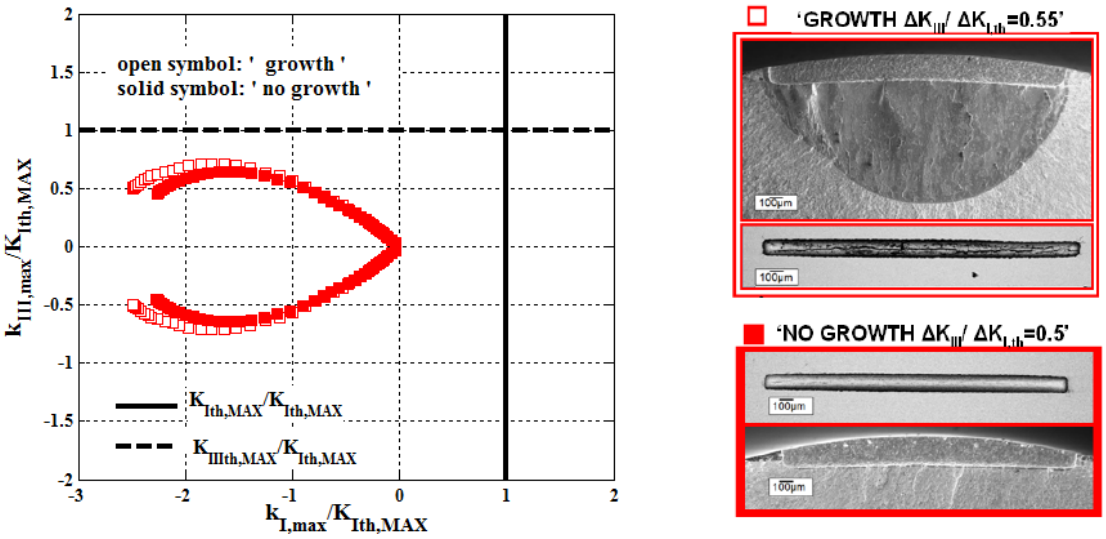

Figure 5.6. Competition between mode I and mode III crack branch stress intensity factors at the tip of mode I pre-crack at the bottom of the micro-notch (√area = 630µm): load path 1.

Figure 5.6 explains why, for a small co-planar crack ahead of the micro-notch, mode I cannot compete with mode III in the out-of-phase load pattern experiments since k_I is always negative, contrarily to what happens in torsional tests where on tilted planes at φ=45° $k_I=k_{III}$. However, the OOP load path is always below the maximum value of the nominal mode III threshold $K_{IIIth,MAX}$ thereby indicating that the crack should not start to propagate under mode III: during the loading cycle, the local mode III SIF, never exceeds $K_{IIIth,MAX}$. On the contrary, the SEM photos of the fractographic surfaces at the threshold condition (named as 'growth') (Figure 5.6), show evidence of shear propagation.

Furthermore, the torsional load path, described in terms of local SIFs (Figure 5.7), simultaneously exceeds the maximum value of both mode III and mode I nominal thresholds $K_{IIIth,MAX}$ and $K_{Ith,MAX}$ respectively, thereby indicating that, under torsional loading, a mixed mode I/III propagation always occurs. Consequently the experimental evidence of mode I propagation without any mode III propagation ("no growth" sample, see Figure 5.7) is not supported by theoretical analysis.

On the other hand (see Figure 5.8), the load path 2 expressed in terms of local SIFs, exceeds the maximum value of mode III nominal threshold $K_{IIIth,MAX}$ but it never exceeds $K_{Ith,MAX}$: accordingly the crack should start to propagate under mode III and

the sample should not never fail by tensile fracture. Oppositely, experimental observations of the fracture surfaces have shown that the fracture mode of samples tested under load path 2 is a mode I-dominated fracture.

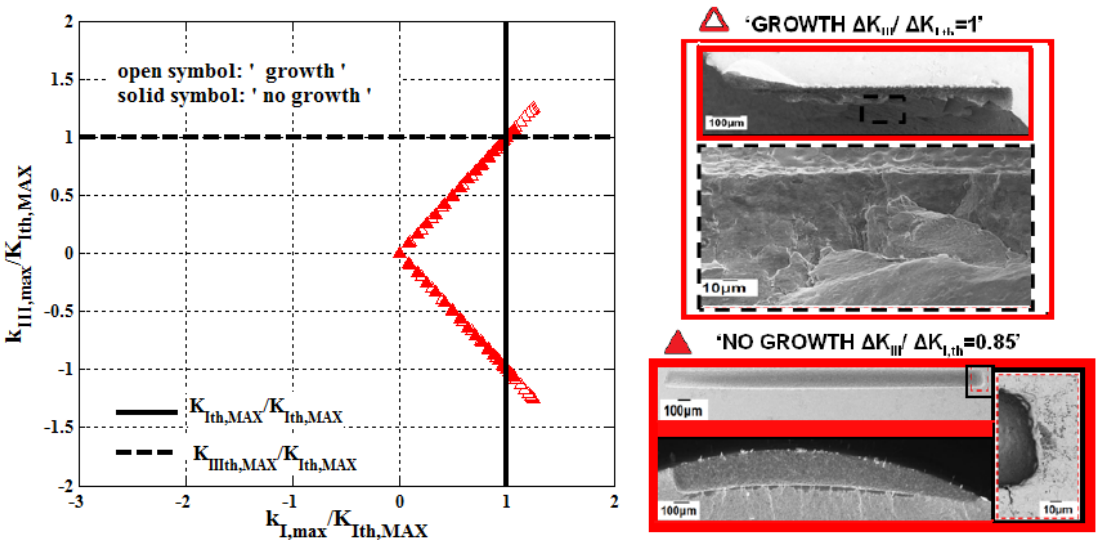

Figure 5.7. Competition between mode I and mode III crack branch stress intensity factors at the tip of mode I pre-crack at the bottom of the micro-notch (√area = 630µm): torsional loading pattern.

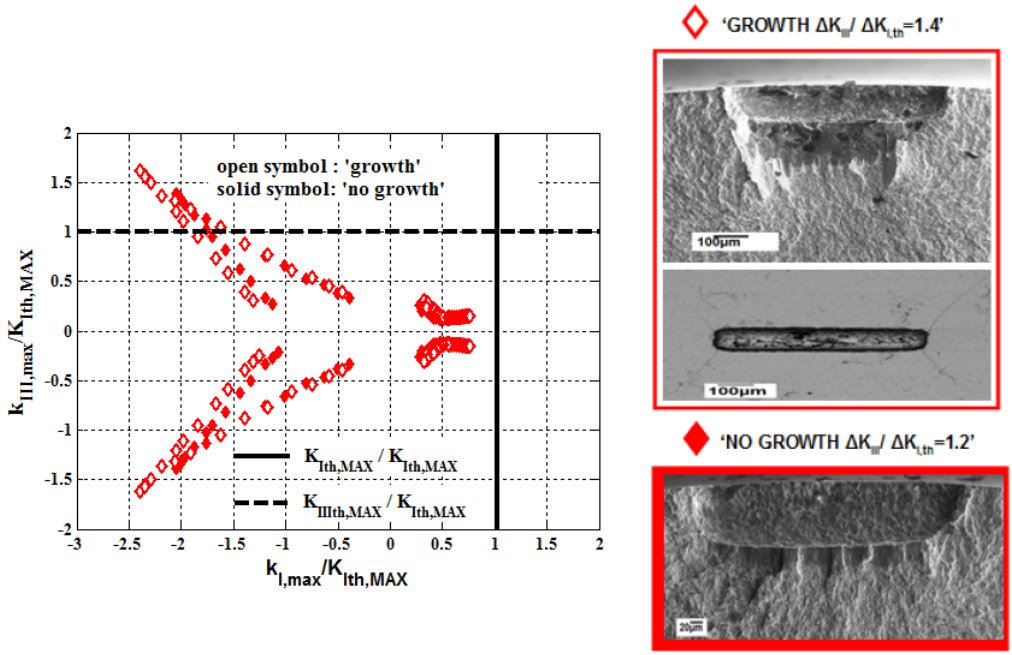

Figure 5.8. Competition between mode I and mode III crack branch stress intensity factors at the tip of mode I pre-crack at the bottom of the micro-notch (√area = 315µm): load path 2.

It appears therefore evident that the competition between mode I and mode III failure mechanisms cannot properly predicted in terms of branch stress intensity factors if both the nominal applied value of the stress intensities and the maximum value of the nominal mode III threshold are used (i.e. nominal K_I, K_{III} and $K_{IIIth,max}$). Again, the leading failure mechanism under both pure mode III and mixed mode I+III testing conditions should be re-examined in terms of effective branch stress intensity factors.

5.4 Competition between mode I and mode III fracture modes taking into account frictional effects

The model for crack sliding interaction, developed in *chapter 4*, has been now employed in order to calculate the effective SIFs, i.e. $K_{I,eff}$ and $K_{III,eff}$ at each time of the loading cycle; consequently, the loading patterns have been re-examined in terms of mode I and mode III branch stress intensity factors after having included the crack sliding interaction effects through $K_{I,eff}$ and $K_{III,eff}$ in Eq.(5.1). Moreover, the maximum value of the effective mode III threshold $K_{IIIth,eff,max}$ under simple shear, obtained in *chapter 3*, has been considered as the threshold value for mode III branching SIF.

The physical parameter used to describe the crack flank roughness, i.e. the slope of the asperity, has been derived from experimental roughness measurements. The topographical map of the asperity height distribution on a bearing steel out-of-phase sample (Figure 5.9) was used to extrapolate the value of asperity angle θ assumed in the current modelling analysis. It was found that θ range from 5° to 10°. The left- and right-hand-side facet angles were hypothesized to be equal and the Coulomb friction coefficient μ=0.5 was assumed.

However, according to the results of *chapter 3*, on account of the residual crack opening between the crack lips (peculiar of the OOP tests), crack face contact is prevented; consequently, during RCF cycles the applied SIFs were actually the effective SIFs experienced by the material at the crack tip.

Results, normalized with respect to the maximum value of the mode I threshold $K_{Ith,MAX}$ for small cracks, are shown trough Figure 5.10 to Figure 5.12.

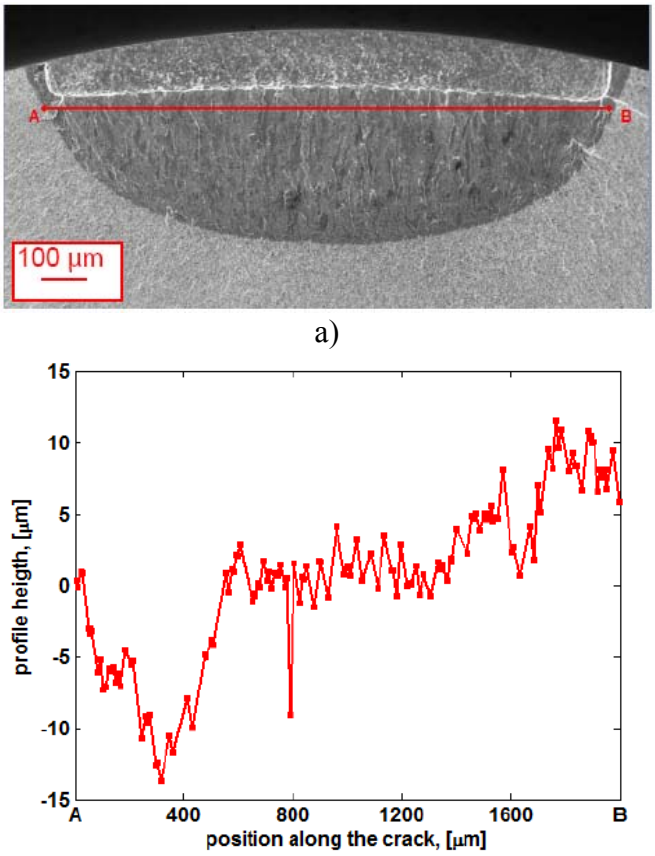

Figure 5.9. Experimental roughness measurements on a bearing steel out-of-phase sample: a) OOP fracture surface of a micro-notch √area = 630 µm tested at ΔKIII/ ΔKIth = 0.85 test interrupted at N = 1.2 x 10^5 cycles; b) asperity height distribution.

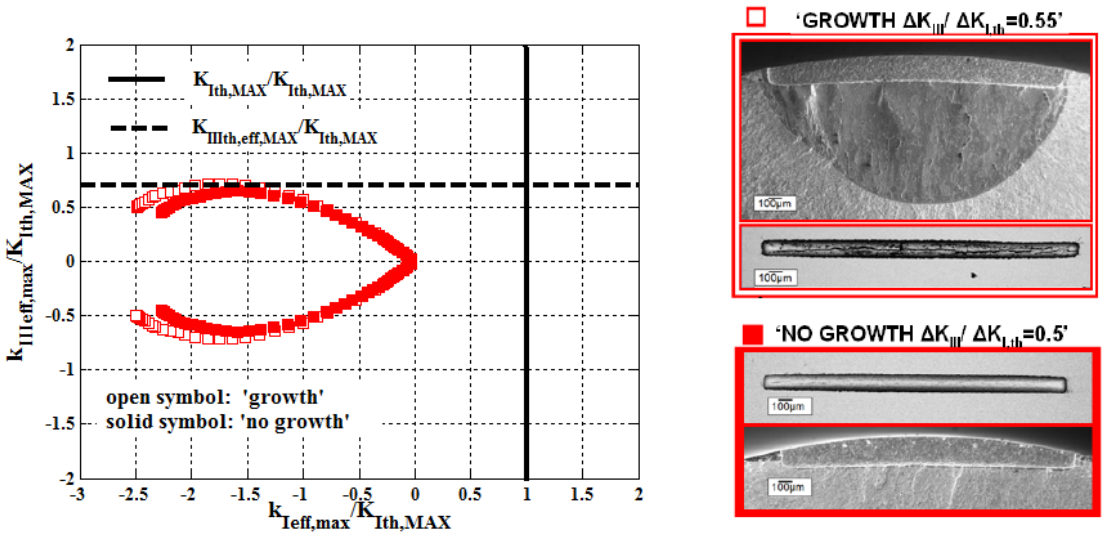

Figure 5.10. Competition between mode I and mode III crack branch stress intensity factors at the tip of mode I pre-crack at the bottom of the micro-notch (√area = 630 µm) after having included the frictional effects: load path 1.

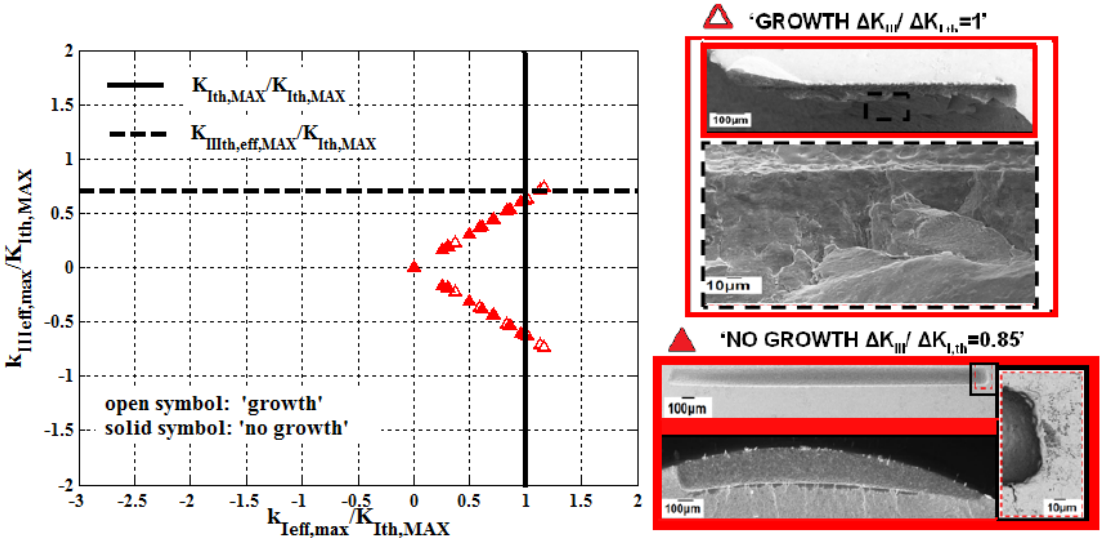

Figure 5.11. Competition between mode I and mode III crack branch stress intensity factors at the tip of mode I pre-crack at the bottom of the micro-notch (√area = 630 µm) after having included the frictional effects: torsional loading pattern.

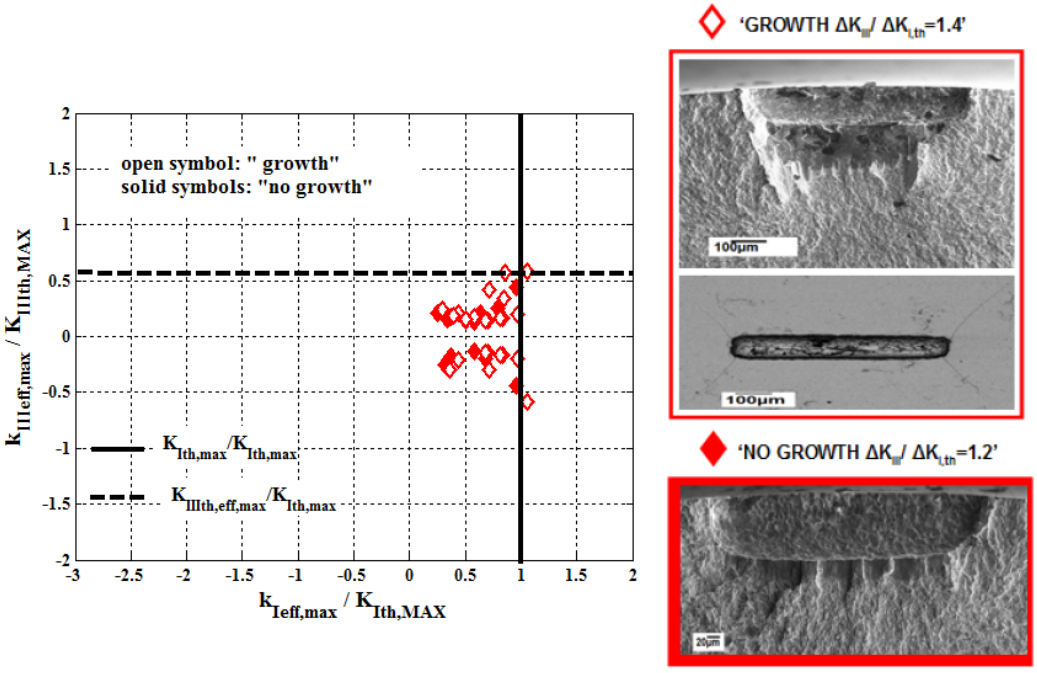

Figure 5.12. Competition between mode I and mode III crack branch stress intensity factors at the tip of mode I pre-crack at the bottom of the micro-notch (√area = 315µm) after having included the frictional effects: load path 2.

When both the maximum value of the effective mode III threshold $K_{IIIth,eff,max}$ (see *chapter 3*) and the crack sliding interaction effects (i.e. the shear attenuation engendered by the frictional stresses through $K_{III,f}$ as well as the induced mode I SIF

$K_{I,w}$ produced by the wedging displacements) are taken into account, the competition between the two fracture modes (mode I vs. mode III) can be finally properly predicted:

- under out-of-phase loading, the crack should start to propagate under mode III since during the loading cycle the local mode III SIF, reaches the maximum value of mode III effective threshold $K_{IIIth,eff,max}$, Figure 5.10;
- under both torsional and load path 2 testing conditions (see Figure 5.11 and Figure 5.12), the competition between the two fracture modes is won by mode I and the component should than fail by mode I fracture; the load patterns, depicted in terms of local branch SIFs, exceed the maximum value of the mode I threshold $K_{Ith,MAX}$ before than $K_{IIIth,eff,max}$ during the loading cycle.

5.5 Conclusions

In the present chapter the competition between mode I and mode III failures under pure mode III and mixed mode I+III testing condition has been examined. The role played by the far-field compression in the promotion of co-planar propagation has been stressed experimentally by carrying out new experimental fatigue tests. The new load path adopted (representative of the stress state experienced by an inclined subsurface crack) again consisted of an axial loading superimposed to the alternating torsion. Nevertheless, the mode I loading was not entirely compressive and the absolute value of the minimum compression was much lower than the one assumed in the OOP load path.

The comparison between mode III fracture surfaces under both the multiaxial testing conditions (i.e. load paths 1 and 2), has experimentally remarked that the enhanced coplanar propagation may be encouraged by the out-of-phase scheme only.

The differences between the macroscopic appearance of the fracture surfaces have also been analyzed: a transition from a shear- (mode III dominated), typical of the OOP samples, to a tensile- (mode I dominated) fracture was observed when the load

path 2 is adopted. Many similarities have also been found between the load path 2 and pure torsional surface appearance since three dimensional macro-structures, almost regularly spaced around the crack front, were observed on the macroscopic crack plane over the above testing conditions. However, unlike in the case of pure torsion testing condition where the nominal mode III threshold ΔK_{IIIth}, corresponding to a 'discontinuous' co-planar crack, was very close to $\Delta K_{Ith,}$ under load path 2 the onset of a stable mode III coplanar propagation has been observed at $\Delta K_{III}/\Delta K_{Ith}$=1.4.

The competition between mode I and mode III fracture modes has also been analyzed theoretically by adopting a LEFM approach: the multiaxial and torsional loading patterns have been examined in terms of local mode I and mode III branch stress intensity factors on tilted planes. When crack sliding interaction effects, which are proposed to generate both a shear attenuation and a positive mode I SIF, are accounted for, the theoretical discussion could support the experimental findings. The model for crack sliding interaction, developed in *chapter 4*, has been employed in order to calculate the effective SIFs, which in turn have been used in order to determine the conditions required for crack branching.

Chapter 6

The role of compression on rolling contact fatigue propagation

6.1 Introduction

Experimental investigations on specimens with shallow defects under out-of-phase loadings (which simulate subsurface rolling contact fatigue conditions in bearings) have clearly shown enhanced co-planar propagation with plastic deformation and rubbing between the crack lips. On the other hand, when the axial loading, superimposed to the alternating torsion, was not entirely compressive, mode III fatigue crack growth was only observed in the range of $\Delta K_{III}/ \Delta K_{Ith}$ larger than a critical value and tensile mode growth was found to be the leading mechanism governing the mode of fracture.

Although encouraged by the cyclic shear stress, the co-planar crack growth under rolling contact loading, is also promoted by the superimposed cyclic compression. The mechanism supporting the enhanced co-planar propagation under RCF may be intuitively explained by the residual opening between the crack lips engendered by the tensile plastic wake formed behind the tip. The shear attenuation was found to be reduced by the residual mode I opening, since the latter prevent crack face contact (see the discussion in *chapter 3*).

The relevant role played by the far-field cyclic compression on the mechanism of shear propagation under RCF was also stressed by Otsuka [2] and Matsunaga [13]. Nevertheless, no further research has been devoted to clarify the contribution of the compressive stress on the promotion of crack growth.

For the aforementioned reason, in the present chapter attempts have been done in order to investigate the role of compression on crack propagation. Furthermore, a test under pure compressive loading has also carried out in order to show experimentally

that the compression itself may not be the only responsible for the enhanced co-planar propagation, thereby confirming that the mechanism of crack growth is actually dominated by shear.

Finally, FE elastic-plastic analyses with crack advance under both pure compressive and rolling contact testing conditions, have been conducted using ABAQUS in order to support the experimental findings. An elastic-plastic constitutive model with non-linear kinematic hardening, fitted to the experimental stress-strain curves of the material, was used.

6.2 Experimental test under pure cyclic compression

6.2.1 Fatigue test procedure

A fatigue test under pure cyclic compression has been carried out on a pre-cracked micro-notched hourglass specimen. A defect size, expressed in terms of Murakami's √area parameter, equal to 315 μm, has been considered. The bearing steel specimen geometry and micro-notch adopted are already reported in *chapter 2*. Details of the preliminary mode I fatigue test pre-cracking procedure can also be found in the same chapter. The fatigue test was conducted in force control by means of a MTS 809 Axial Torsional System at the same frequency adopted in the out-of-phase tests (i.e. at 2 Hz). The compressive loading pattern has the shape assumed by the axial stress component in the OOP scheme (see Figure 6.1); the test has been carried out at a value of the compression load and for a number of cycles higher than the corresponding values adopted to test an out-of-phase sample which exhibited an enhanced mode III crack propagation.

6.2.2 Fatigue test result

The test under pure compressive loading has been carried out with the aim of experimentally confirming the "shear-type" nature of the enhanced co-planar

propagation observed under out-of-phase fatigue testing conditions, typical of subsurface rolling contact fatigue in bearings.

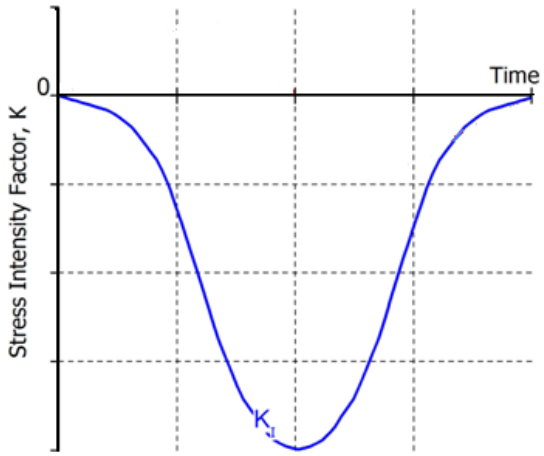

Figure 6.1. Cyclic compression load path adopted for uniaxial fatigue test.

The test has been carried out using the cyclic compressive stress corresponding to a test at $\Delta K_{III}/\Delta K_{Ith} = 0.8$, and it has been interrupted after $N = 2 \times 10^5$ fatigue cycles. The out-of-phase test carried out at $\Delta K_{III}/\Delta K_{Ith} = 0.7$ for $N=1.2 \times 10^5$ cycles on a micro-notched ($\sqrt{area}$=315μm) sample was chosen for comparison. The comparison between the co-planar propagation extents under the above testing conditions is shown in Figure 6.2. It appears evident that an enhanced co-planar propagation may only be achievable under out-of-phase loading conditions. While under pure cyclic compression the extent of the co-planar crack is about few tens longer than the pre-crack length, under RCF testing condition the crack propagated forward 220 μm from the notch depth on the plane perpendicular to the specimen longitudinal direction.

Consequently, it can be concluded that the co-planar crack growth may not be solely due to the compression itself, when it acts without the superimposition of an alternating torsion: mechanisms similar to the compression pre-cracking may not encourage the crack propagation.

6.3 Elastic-plastic FE analyses of crack advance: modelling issues

Till now, the role of compression has been extensively supported by the observations of experimental fatigue fracture surfaces, which have revealed the extent of the co-planar propagation. Elastic-plastic finite element analyses with crack advance have been also conducted in order to support the experimental findings. The crack tip shielding phenomena, engendered by crack tip wake plasticity, are investigated through the FE numerical study. Crack tip shielding strongly affects the propagation behaviour: in a fracture mechanics representation, in fact, the crack extension is driven by the "effective driving forces" which are reduced by closure phenomena at the crack tip.

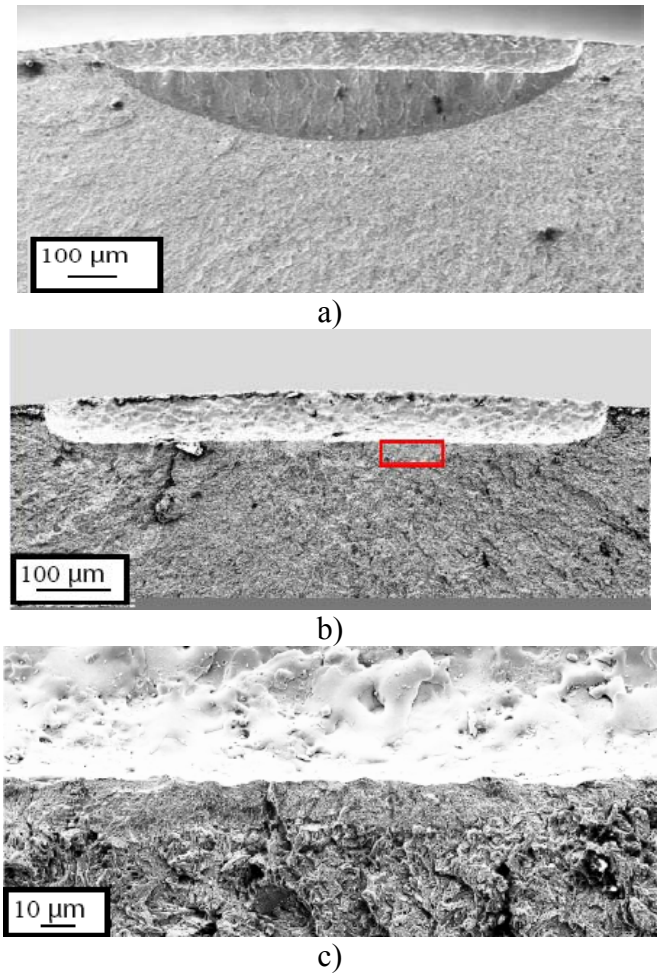

Figure 6.2. Co-planar fracture surfaces for micro-notches (√area = 315 µm): a) out-of-phase sample tested at $\Delta K_{III}/\Delta K_{Ith}$ = 0.7 (test interrupted at N = 1.2 x 10^5 cycles); b) pure compression sample tested at $\Delta K_{III}/\Delta K_{Ith}$ = 0.8 (test interrupted at N = 2 x 10^5 cycles); c) magnification of the framed area in b).

Consequently, the crack growth behaviour is dictated by the relative magnitude of the crack tip opening and sliding displacements ranges: as long as the crack tip is "protected" by tensile/sliding displacement, the crack propagation promoted by mode I/shear is not allowed. Accordingly, it should be then expected that under rolling contact loadings, the co-planar crack propagation is encouraged by shear since the opening/closing behaviour at the crack tip is fully suppressed by the compressive stress.

In order to verify such intuitive explanation of the crack propagation mechanism under RCF, FE analyses are conducted using ABAQUS. Because of the strict requirements on mesh refinements, which induce a severe computational burden, a two-dimensional numerical model is employed. Since the aim of the FE analyses with crack advance is to provide a straightforward comparison between the crack propagation behaviour under both pure compressive and rolling contact fatigue testing conditions, the above purpose can also be achieved by adopting a two-dimensional model of a centre notch with edge cracks initiated at both the ends.

The scheme of the numerical modelling analysis of a growing fatigue crack is conceptually simple: a geometrical model, with a refined mesh around the crack tip, is first constructed and the fatigue loads are then applied to the mesh. During the fatigue, the crack is advanced in some fashion and a plastic wake behind the crack tip is formed while the crack extends.

Nevertheless, it should be also remarked that FE simulations of a growing fatigue crack do not involve considerations of the crack growth physics, since crack advance increments are not comparable to the experimental crack growth rate per cycle. Otherwise enormous computation times would be required. The FE analyses of crack advance are in stead developed in order to predict both the opening-closing and slipping/unslipping behaviour at the crack tip. Although the conceptual scheme is extremely simple, numerical issues, which should be addressed when modelling a growing fatigue crack, are quite strict.

Up to now no attempts have been directed to model the crack tip shielding phenomena by crack tip wake plasticity under multiaxial loadings. Prior to the discussion of FE results, the basic modelling issues are briefly presented. Although the suggested FE

modelling design guidelines, provided by literature, are specifically pertinent to the numerical simulation of mode I growing fatigue crack, they are taken into account in the current study.

6.3.1 Mesh refinement

The refinement of the mesh along the crack line is a crucial aspect in the modelling analysis of a growing fatigue crack. The possible effects of different mesh design criteria were exhaustively discussed by McClung and Sehitoglu [63]. The refinement of the mesh is found to be extremely important at least for the two following reasons: first, the mesh should be fine enough to properly capture the stress variations around the crack tip (the plastic wake behind the crack tip could be accurately defined if a very refined mesh is adopted); second, the incremental crack extension, related to the element spacing, should be small enough in order to simulate the "real" crack growth. Suggested criteria, available in the literature, for sufficient mesh refinement are based on the ratio of the element size over the plastic zone dimension. However, the question of "the proper discretization" of the plastic zone has been and still is controversial. During crack advance in cyclic tension or compression, two different types of crack tip plastic zones can be defined, i.e. :

- the forward or monotonic plastic zone: it is defined by the plastically deformed material near the crack tip at the maximum applied load;
- the reversed or cyclic plastic zone: it is defined by the plastically deformed material near the crack tip after a loading cycle.

The extent of the reversed plastic zone for a stationary crack under cyclic tension is theoretically a quarter of the forward plastic zone [64]. Newman [65], who first investigated the problem of mesh refinement by modelling a middle-crack tension specimen of finite width with constant strain triangles of different sizes, described the mesh spacing on the basis of the ratio of the crack growth increment over the forward plastic zone size. On the other hand, Solanski et al [66] as well as McClung and

Sehitoglu ([63],[67]) related the crack growth increment to the reversed plastic zone size.

In opposition to the aforementioned considerations, computational times have to be considered: extensive mesh refinement will result in large execution times. In the current modelling analysis, an element size of 0.5 μm is used to mesh the zone around the crack tip. Further details of the mesh adopted are provided in the following.

6.3.2 Stabilization behaviour and notch effect

When dealing with closure phenomena engendered by the plastic wake formed behind the crack tip, it is of some importance to properly predict the stress value at which opening occurs. Numerical analyses of plasticity-induced fatigue crack closure under constant amplitude tensile loading have shown that the crack opening load will typically increase monotonically with the crack advance [63],[65].

A "notch effect" on the opening/closing behaviour at the crack tip was also stressed by McClung and Sehitoglu [63]: the stabilization of the closure stress levels were found to be relatively rapid and somewhat slow at low and high stress amplitudes respectively. A "true notch effect" was argued by the same authors after the observations of the crack opening stress variations corresponding to circular holes, with different radii, under the same applied tensile loading.

Design criteria suggest that, in presence of a notch, the crack should be allowed to grow out of the notch field. The above recommendation is properly taken into account in the current numerical study.

Furthermore, since the stabilization behaviour was found to be also affected by the "maximum time step size" during the loading application; the following assumptions are then adopted:

- in FE analysis of crack propagation under pure compressive loading, the maximum time step size is fixed equal to the 2.5% of the time period;
- in FE analysis of crack propagation under out-of-phase loading, the maximum time step size is fixed equal to the 5% of the time period.

6.3.3 Crack advance scheme

During the applied cyclic loading, the crack is incrementally advanced by releasing the crack tip node.

Consequently, after a node release the crack is advanced by an amount equal to the element size along the crack line. Nearly all FE analyses simulating a growing fatigue crack adopted three primary node release schemes, i.e.:

- crack tip node release at the maximum load in each cycle: this technique was suggested by Newman [65] and later employed by Fleck [68] and Blom & Holm [69];
- crack tip node release at the minimum load in each cycle: this technique was employed by Ogura et al [70]-[71]; however, since at the minimum load the crack tip is actually closed, the node release effectively occurs upon re-loading;
- crack tip node release immediately after the maximum load in each cycle: this technique was implemented by Lalor and Sehitoglu [72]; adopting this scheme the crack tip was advanced immediately after the point of maximum load, during the first increment upon unloading.

Each of these schemes has been found to give approximately the same results in terms of opening/closing stress values predictions [73]. Although some authors [74] have reported significative variations in the closure stress levels assessments, such differences may be attributed to an inadequate mesh refinement of the elements along the crack line. Moreover, in the above release schemes the crack is advanced on every cycle: however, the sudden release of a node, both at and immediately after the maximum/minimum load, could result in artificial residual strains or stresses which would be not eliminated before the next node release occurred [63]. Consequently, McClung and Sehitoglu have proposed a further node release where two or more full cycles were completed at each crack length before releasing the next node.

In the current numerical study the latter scheme is adopted: the crack tip is released just after the maximum compressive load (i.e. just after the time step where the axial

stress is zero) and the crack is cycled four times at each crack length before releasing the next node. Figure 6.3 shows the release schemes adopted for FE simulations under both pure compressive and out-of-phase loading conditions; the applied stresses are presented in a normalized form with respect to the maximum value of the shear stress component of the OOP pattern. In order to provide a straightforward comparison between the crack growth behaviour under the above loading conditions, the same value of the remote compressive stress is adopted.

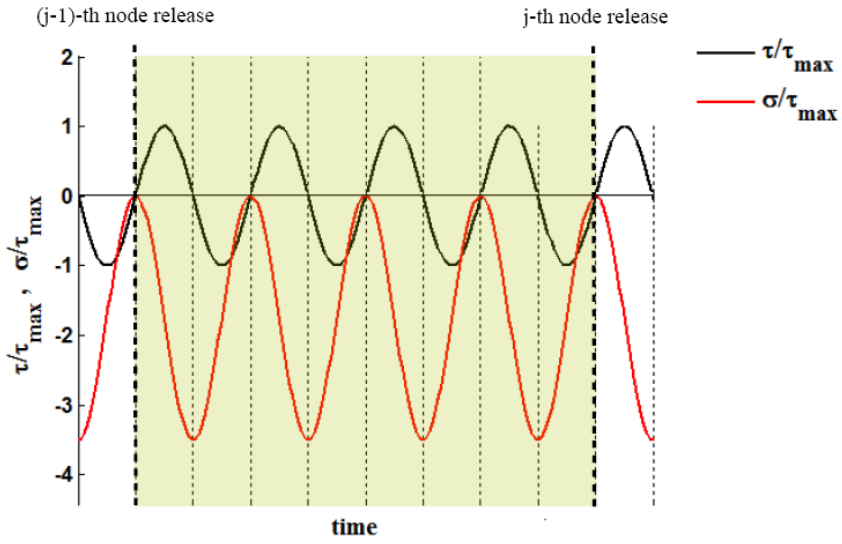

a)

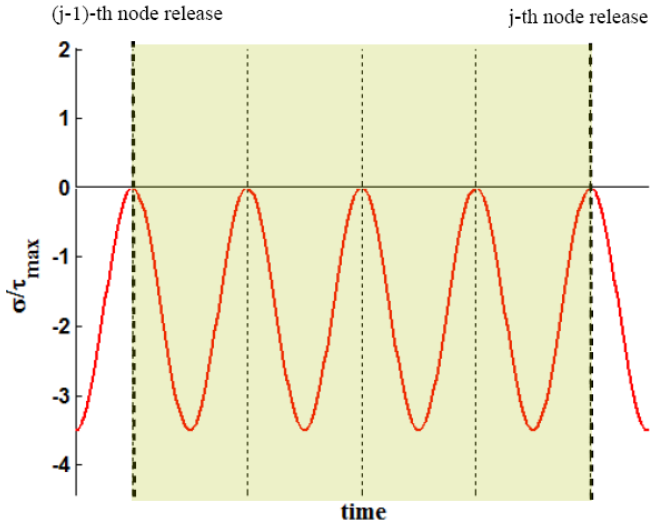

b)

Figure 6.3. Node release scheme adopted in order to simulate crack advance under: a) out-of-phase loading; b) pure compressive loading.

At each node release, the size of the crack increment is assumed as follows:

- in FE analysis of crack propagation under pure compressive loading, the growing fatigue crack is advanced forward 3μm;
- in FE analysis of crack propagation under out-of-phase loading, the growing fatigue crack is advanced forward 10 μm.

However, the size of the crack increment is not likely to change the closure levels provided that the model mesh refinement is fine enough to correctly capture the plastic zones around the crack tip [75].
A further relevant aspect in the numerical design of the growing fatigue crack FE model is the technique adopted to release a node: although different modelling techniques have been proposed by literature, many authors ([63], [76]) have used truss elements along the crack line to translate the changing boundary conditions into the FE model; the spring stiffness was set to an extremely large value before releasing a node, after the crack advance, in stead, it was set to a negligibly small value.
In the current numerical study, a different modelling technique is used to simulate the crack growth: the changing boundary conditions are directly accommodated by removing progressively the nodal constraints (as allowed by the ABAQUS software). At this scope, the computation is defined by many steps where the changing boundary conditions are written as an ABAQUS input file.
Furthermore, the penetration between the two crack lips is avoided by employing an "hard condition" when modelling the contact between the crack faces.

6.3.4 Crack opening and closing assessments

Two characteristic stress levels are descriptive of the crack tip closure phenomena:

- the crack opening stress: it is commonly identified by the value of the remote load corresponding to a "fully open" condition of the crack tip, (i.e. no points of contacts exist behind the crack tip) [67]; besides this conventional

definition, both the first node of the element behind the crack tip and the crack tip node itself have also been used to determine the crack opening levels; when the first node of the element behind the crack tip is used [76], the crack is assumed to be opened when the ratio of the displacement variation of this node over its maximum value (within a cycle) reaches 1.5%; on the other hand when the crack tip itself is used [74], the crack is assumed to be opened when the principal stress perpendicular to the crack tip becomes tensile;

- the crack closing stress: analogously the crack opening stress assessments, two definitions are commonly accepted; according to conventional definition the crack is assumed to be closed when some point along the crack surface first makes contact; according to the alternative definition involving the crack tip node, the crack is said to be closed when the principal stress perpendicular to the crack tip becomes compressive.

While the conventional definition relates the concept of closing and opening to the macroscopic physical contact and separation between the crack faces; the definition based on the crack tip stress field involves the necessary condition for crack propagation, which requires a tensile stress perpendicular to the crack tip.
Although the opening and closing stress levels are commonly assumed to be exactly the same, McClung and Sehitoglu [67] have shown that the closing levels can be consistently lower than the corresponding opening levels.
In the current modelling analysis of crack advance under both pure compression and out-of-phase loading conditions, the conventional definition proposed by McClung and Sehitoglu [67] is employed in order to determine the crack opening and closing stresses. Moreover, the determination of such stress levels is performed at the fourth cycle for each crack length.

6.3.5 Effect of the constitutive model

Crack shielding phenomena involve cyclic plasticity at the crack tip: as a matter of fact, the choice of the constitutive model adopted for the FE simulation of a growing

fatigue crack, is fundamental since it allows a properly representation of material cyclic plastic response. When a perfect plasticity assumption is employed, the material cyclic plastic behaviour is not accurately described since observed phenomena, such as softening, hardening, cyclic ratchetting and Bauschinger effect cannot be simulated. Unfortunately, nearly all FE analyses of closure phenomena induced by plasticity were not directed to investigate the effect of the material constitutive model [77].

McClung and Sehitoglu [67] showed that when a power-law hardening formulation was employed, the crack opening stress levels were significantly higher in comparison with the opening stresses obtained adopting a linear-hardening formulation consistently with the development of plastic strains at lower stress under the power-law hardening assumption. Moreover, the same authors also examined the effect of the ratio of the strain hardening exponent over the elastic modulus, showing that for low hardening material the FE results were comparable to numerical estimates under the assumption of perfect plasticity.

On the other side, Pommier and Bompard [76] investigated the Bauschinger effect on the closure levels: in their modelling analysis, the Bauschinger effect was accommodated by using the Chaboche plastic constitutive model. The retarding effect due to an overload was found to be vanished by the BE which is proposed to diminish the stress level at which the crack is again open during unloading.

In the current numerical simulation of a growing fatigue crack under both pure compressive and out of phase loading conditions, a rate independent nonlinear kinematic hardening constitutive model is used. It is accommodated by the Chaboche model [78], which is provided from version 6.9 in the ABAQUS code.

The yield surfaces is defined through the equation $F = 0$ according to the Von Mises yield criterion:

$$F = f\left(\boldsymbol{\sigma} - \boldsymbol{\alpha}\right) - \sigma^0 = 0 \tag{6.1}$$

where σ^0 is the yield stress and $f(\boldsymbol{\sigma}-\boldsymbol{\alpha})$ is the equivalent Mises stress with respect to the shift tensor $\boldsymbol{\alpha}$, i.e. :

$$f\left(\boldsymbol{\sigma}-\boldsymbol{\alpha}\right)=\sqrt{\frac{3}{2}\left(\mathbf{S}-\mathbf{A}\right):\left(\mathbf{S}-\mathbf{A}\right)} \tag{6.2}$$

In Eq. (6.2) $\boldsymbol{S}$ is the deviatoric stress tensor and $\boldsymbol{A}$ is the deviatoric part of the shift tensor. The shift tensor describes the displacement of the centre of the yield surface due to the plastic strain. The evolution law of the shift tensor is:

$$\dot{\boldsymbol{\alpha}}=\frac{C}{\sigma^{0}}\left(\boldsymbol{\sigma}-\boldsymbol{\alpha}\right)\dot{\bar{\varepsilon}}^{pl}-\gamma\boldsymbol{\alpha}\dot{\bar{\varepsilon}}^{pl} \tag{6.3}$$

where C is the initial kinematic hardening modulus and γ determines the rate at which the cinematic hardening modulus decreases with increasing plastic deformation.
Moreover, the kinematic hardening model assumes associated plastic flow, where the equivalent plastic strain rate is related to the rate of plastic flow:

$$\dot{\bar{\varepsilon}}^{pl}=\sqrt{\frac{2}{3}\dot{\varepsilon}^{pl}:\dot{\varepsilon}^{pl}} \tag{6.4}$$

The evolution of the yield surface size σ^{0} is described by a simple exponential law:

$$\sigma^{0}=\sigma|_{0}+Q_{\infty}\left(1-\mathrm{e}^{-b_{h}\bar{\varepsilon}^{pl}}\right) \tag{6.5}$$

where $\sigma|_{0}$ is the initial value of the radius of the yield surface, Q_{∞} and b_{h} are material parameters which respectively define the maximum change in the size of the yield surface and the rate at which the size of the yield surface changes as plastic straining develops.
The coefficients of the Chaboche model, fitted to the experimental stress-strain curves of the material, are reported in Table 6.1.
The constitutive model reduces to a nonlinear kinematic hardening model since the equivalent stress defining the size of the yield surface remains constant.

	$\sigma\|_0$ [MPa]	Q_∞ [MPa]	b_h	C [MPa]	γ
Bearing steel	1500	0	0	769790	684

Table 6.1. Parameters of the Chaboche constitutive model.

6.4 FE analysis of crack propagation under cyclic compression

6.4.1 Finite element formulation

A finite element analysis of crack advance under far-field cyclic compression has been conducted with the aim of confirming numerically the experimental result of the test under pure compressive loading (see paragraph 6.2). It has been shown that the co-planar crack propagation cannot be encouraged by the far-field cyclic compression only since, under pure compressive testing condition, the crack extension was about few tens longer than the pre-crack length.

The 2D model of the micro-notched specimen tested experimentally (where the defect size, expressed in term of Murakami's √area parameter is equal to 315 μm) is shown in Figure 6.4. Because of the symmetry, only one quarter of the specimen is modelled and boundary conditions, consistent with the symmetry, are then applied.

A representation of the FE mesh around the crack tip is shown in Figure 6.5. In the current numerical analysis, all the computations have been conducted under plane strain conditions. Accordingly, four-noded CPE4 elements together with a complete integration scheme have been used. It has been assessed by McClung and Sehitoglu [63] that true higher-order elements are not generally feasible due to the computation expense associated with the additional degrees-of-freedom required.

The smallest size of the element used to mesh the crack propagation region is 0.5 μm which is only ~ 1/1000 of the initial total crack length, where the latter is considered as the sum of the notch half-width (500 μm) and the mode I pre-crack (20 μm).

A "node to surface" numerical discretization for contact between a single crack surface node and a rigid body is used to model the contact between a single crack surface node and the plane of symmetry. The latter is represented by introducing an

analytical rigid surface (see Figure 6.4) and the symmetry boundary condition, in respect to the plane y = 0, is applied to the rigid surface by the reference point (see Figure 6.4). The cyclic compression is applied as “pressure” on the top surface and the stress amplitude is defined by an harmonic periodic function expressed as Fourier series. The maximum time step size is set equal to the 2.5% of the time period.

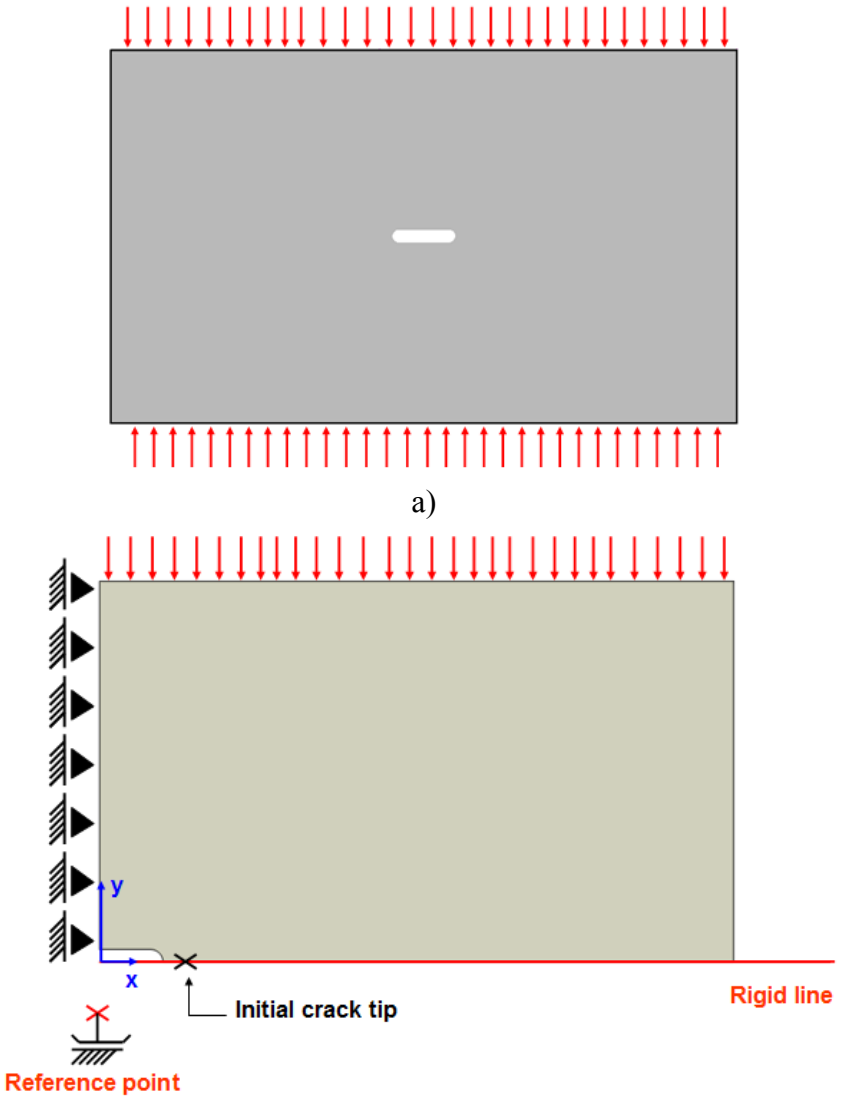

Figure 6.4. FE model under far-field cyclic compression: a) geometric model; b) a quarter of the specimen adopted for FE simulation.

The crack is advanced forward 3 μm following the scheme depicted in Figure 6.3. The node is released by changing the boundary conditions along the crack line.

The mechanical material properties adopted have already been reported in *chapter 2*, and the nonlinear kinematic hardening parameters of the Chaboche constitutive model are summarized in Table 6.1.

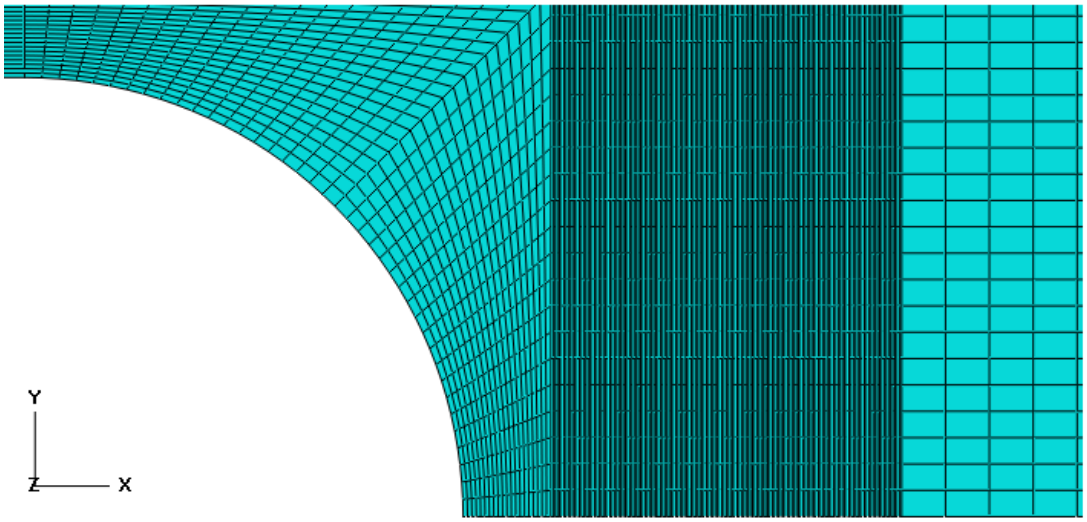

Figure 6.5. A typical FE mesh near the crack tip.

6.4.2 Results and discussion

The closure phenomena induced by the plastic wake formed behind the crack tip under far-field cyclic compression have been numerically investigated. The closure assessments definition has been already clarified in paragraph 6.3.4.

Figure 6.6 shows the crack opening/closing stresses normalized with respect to the maximum value of the corresponding shear stress component of the OOP load pattern. Both the closing and opening stresses approach the same values.

FE results, reported in Figure 6.6, are consistent with the theoretical and experimental discussion reported by Suresh [79]: for a short fatigue crack initiating from a notch, little closure phenomena exist behind the crack tip because of the limited crack plastic wake. In the early stage of crack propagation, the fracture crack surfaces remain closed during the 60% of the compressive loading cycle. As the length of the fatigue crack increases, a progressive enhancement in crack closure is noted on account of the residual tensile stresses engendered by the far-field compressive loading: complete

closure can be observed when the growing fatigue crack has propagated forward 63 μm from its initial length.

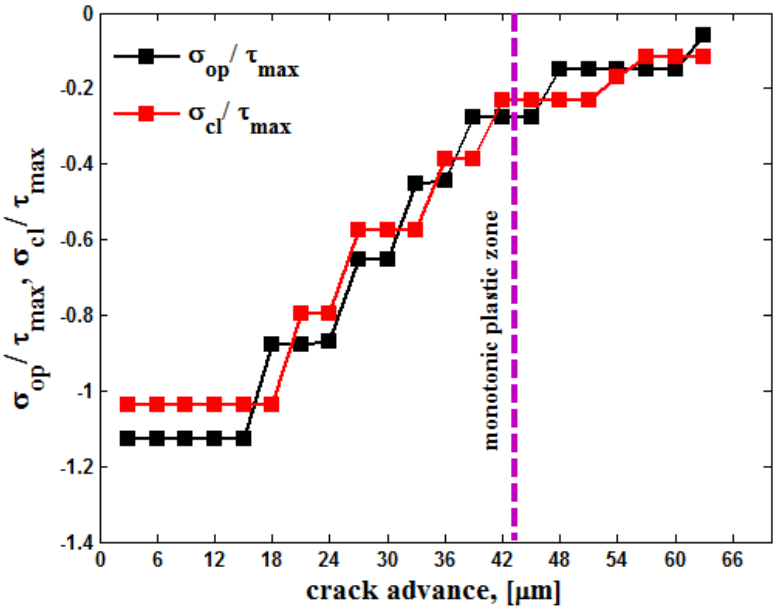

Figure 6.6. Normalized crack opening/closing stresses as a function of the current crack length for a crack under far-field cyclic compression.

The numerical results can be further examined in terms of mode I effective driving force: because of crack tip shielding phenomena induced by plasticity, the effective mode I SIF range ΔK_{Ieff}, which drives the crack extension, is related to the portion of the loading cycle where the crack is "fully open" till its tip.

Figure 6.7 shows the variation of ΔK_{Ieff} as a function of the crack advance. Results are normalized with respect to the effective mode I threshold for long cracks $\Delta K_{Ith,lc,eff}$. Closure information on $\Delta K_{Ith,lc}$ is conveyed by the effective stress range U (i.e. $\Delta K_{Ith,lc,eff} = U\, \Delta K_{Ith,lc}$). At R = -1, U ranges from 0.3 to 0.4.

The FE simulation of a growing fatigue crack under far-field cyclic compression is consistent with the experimental finding: the crack length at which the closure/opening loads decrease the effective mode I stress intensity factor ΔK_{Ieff} to a value below the effective threshold range for long cracks $\Delta K_{Ith,lc,eff}$ correspond well with the experimental evidence of a slender growth extent under cyclic compression. Finally, ΔK_{Ieff} progressively decreases with crack advance.

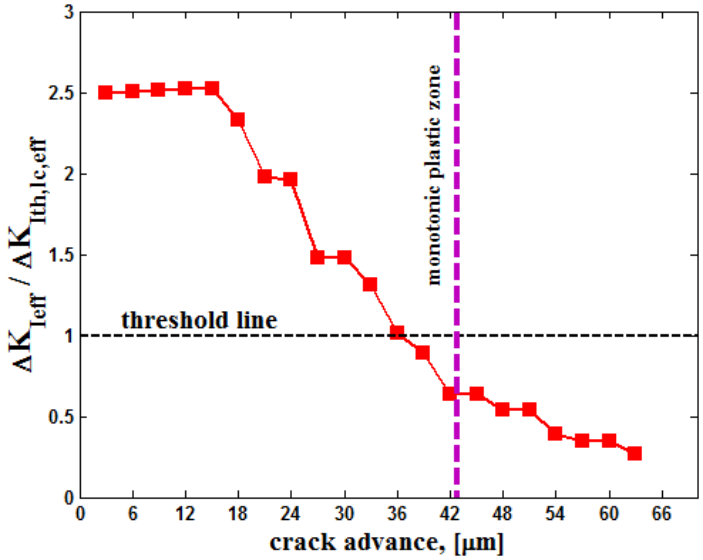

Figure 6.7. Variation of the effective stress intensity factor range, normalized in respect to the threshold range for long cracks, with increasing crack length.

6.5 FE analysis of crack propagation under out-of-phase loading

6.5.1 Finite element formulation

A finite element simulation of crack advance under out-of-phase loading is now conducted with the aim of clarifying the role played by compression on the mechanism promoting crack propagation under RCF. The two-dimensional geometrical model, adopted for the FE analysis, together with the mesh description have been already provided in paragraph 6.4. Boundary conditions are applied on the bottom surface by constricting displacements in the y direction. Additionally, the horizontal displacement of a single point on the bottom surface has been fixed in order to avoid numerical convergence problems (see Figure 6.8).

A "node to surface" numerical discretization is used to model the contact between the fracture crack surfaces. Moreover, besides the "hard contact" condition, introduced to prevent penetration of the two crack lips, a "penalty" condition, accommodated by a Coulomb friction model, is used. The friction coefficient is assumed equal to $\mu = 0.5$.

The cyclic compression is applied as "pressure" on the top surface, while the remote shear stress is applied as "surface traction stress" on the undeformed area. Both the

shear and the axial stress amplitudes are defined by an harmonic periodic function. The maximum time step size is fixed equal to the 5% of the time period.

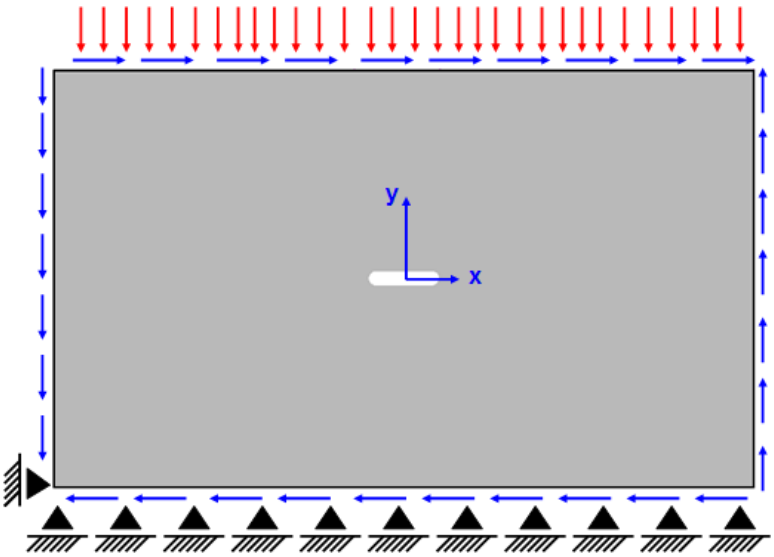

Figure 6.8. FE model adopted under out-of-phase loading pattern.

The crack is advanced forward 10 μm following the scheme depicted in Figure 6.3. A nonlinear kinematic hardening accommodated by the Chaboche constitutive model is again used.

6.5.2 Results and discussion

The leading mechanism (tensile vs. shear) governing the crack growth behaviour under rolling contact fatigue loading cannot be simply assessed by the observation of the opening/closing phenomena at the crack tip only. Although remaining closed, the crack flanks are displaced relatively to one another during the cyclic shear load. The interaction between the sliding crack surfaces has been proposed to be a very prominent shielding mechanism during fatigue crack growth under simple shear (see the discussion in *chapters 3* and *4*). For the aforementioned reason, both the opening/closing and the slipping/unslipping behaviour at the crack tip are now discussed.

Closure assessments, inferred according to criteria reported in 6.3.4, are shown in Figure 6.9. Results are again presented in a normalized form with respect to the

maximum value of the shear stress component. The opening and closing stresses approach the same value during fatigue crack growth. A "short crack effect" on the closure behaviour at the crack tip can be observed under OOP loading as well: in the early stage of propagation, little closure exist behind the crack tip and the crack surfaces are found to be opened during the 50% of the fatigue cycle. As the crack extends, a progressive enhancement in crack closure is noted: when the crack has propagated forward 100 μm from its initial length the closure range is up to 95% of the applied load range.

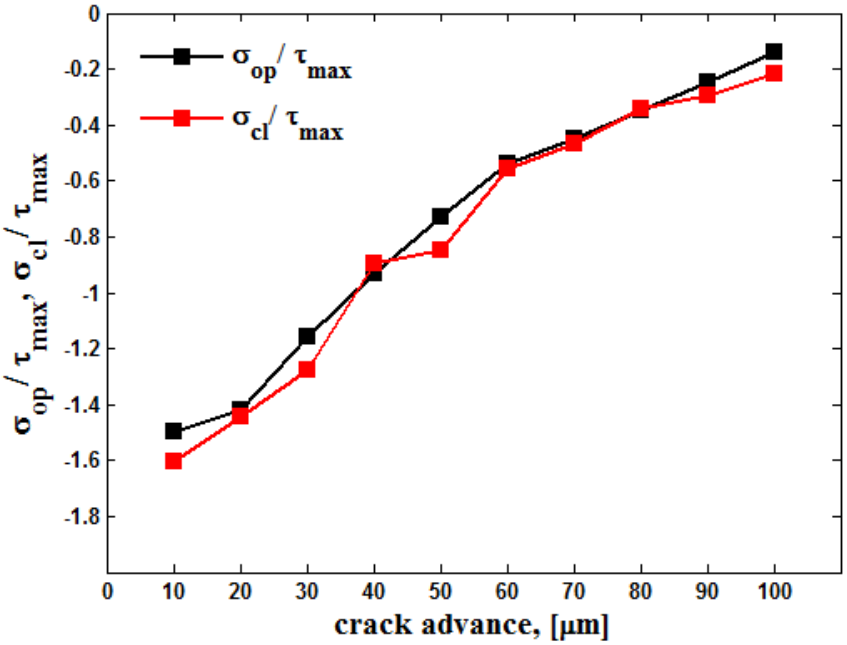

Figure 6.9. Normalized crack opening/closing stresses as a function of the current crack length for a crack under out-of-phase loadings.

Although the crack tip opening is progressively suppressed by the far-field cyclic compression as long as the crack extends, the crack faces are found to be always slipped during the fatigue cycle. Accordingly, since slip reaches the tip, the crack growth encouraged by shear can take place.

Consistently with the discussion developed in [6], [52] and in *chapter 4* as well, the effective shear driving force at the crack tip ΔK_{IIeff} is determined from mode II kinetic data. The effective mode II SIF range is calculated by interpolating the range

of cyclic crack flank shear displacements ΔU_x with the theoretical asymptotic profile in plane strain [80]:

$$\Delta U_x = \max_t \left(u_{x,i} - u_{x,j}\right) - \min_t \left(u_{x,i} - u_{x,j}\right) = \frac{8\left(1-\nu^2\right)}{E} \Delta K_{IIeff} \sqrt{\frac{a}{2\pi}} \tag{6.6}$$

where a is the current crack length.

The displacement field is computed using the FE program. In Eq. (6.6) the nodes, i and j, on opposing crack surfaces, are located at the same distance from the origin of the coordinate system. The local coordinate system at the crack tip is shown in Figure 6.10.

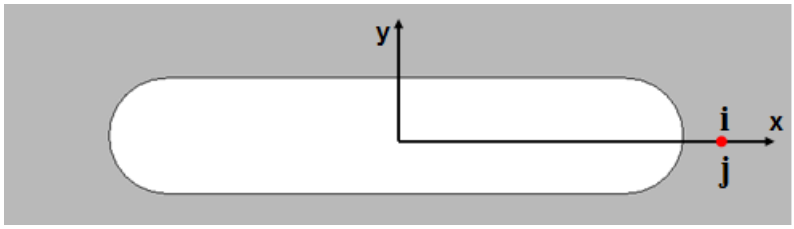

Figure 6.10. Local coordinate system.

The sliding displacement profile interpolated by the asymptotic solution (for a growing fatigue crack with the current crack tip located at a distance = 60 μm from the notch half-width) is shown in Figure 6.11.

Eq. (6.6) also accounts for frictional dissipative phenomena between the sliding crack flanks (the effective FE displacement field is calculated after having introduced the "penalty condition" in the ABAQUS code). The cyclic variation of the shear displacement at a distance equal to the notch half-width, for a growing fatigue crack propagated forward 40 μm from its initial length, is shown in Figure 6.12. A "macroscopic locking behaviour" can be observed at load reversals. Furthermore, at load reversal at the maximum load the crack remains "macroscopically locked" for almost half a cycle on account of the increasing value of the compressive stress; the extent of "macroscopic locking" at load reversal at the minimum load is , in stead, limited as the compressive stress is decreasing.

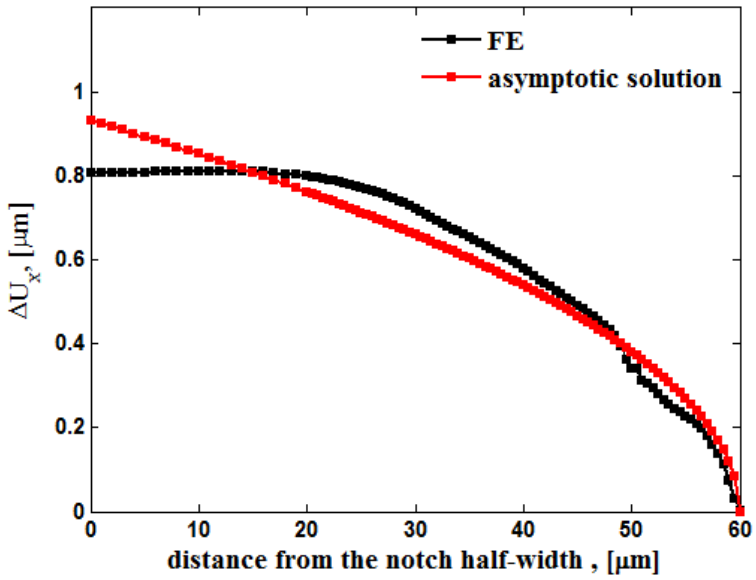

Figure 6.11. Sliding displacement profile interpolated by the asymptotic solution for the calculation of ΔK_{IIeff} .

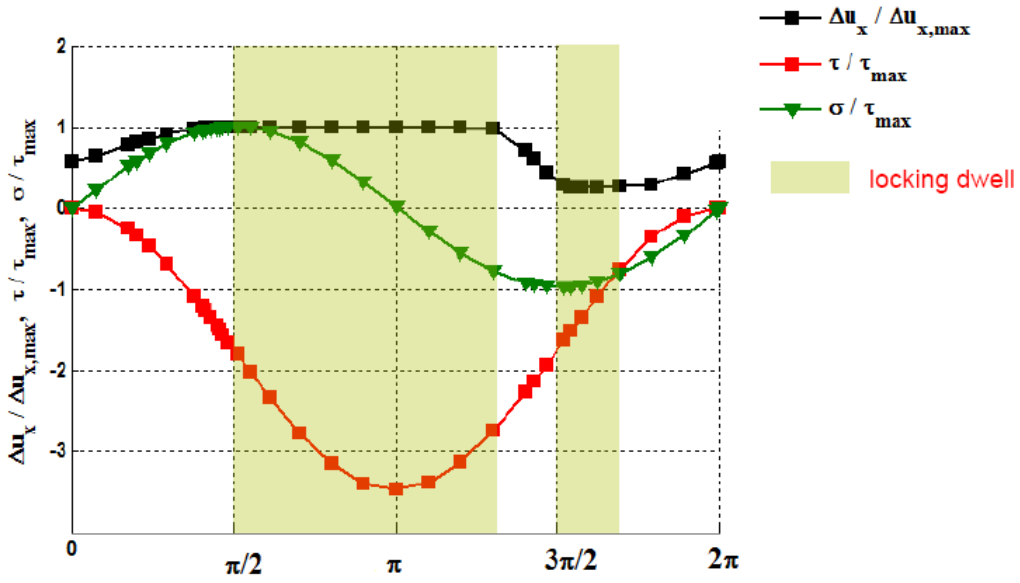

Figure 6.12. FE results for cyclic crack flank shear displacement at a distance equal to the notch half-width for a growing fatigue crack propagated forward 40 μm from its initial length.

Since $\Delta K_{Ieff}/\Delta K_{IIeff}$ drives the mode I/mode II crack extension, the leading mechanism (tensile vs. shear), governing the crack propagation behaviour under rolling contact fatigue testing conditions, can be explained by the competition between ΔK_{Ieff} and ΔK_{IIeff} (where the former is again related to the portion of the loading cycle where the crack remains open).

The competitive failure mechanisms is depicted in Figure 6.13. Both the effective stress intensity ranges are presented in a normalized form. ΔK_{Ieff} is again normalized with respect to the effective mode I threshold for long cracks $\Delta K_{Ith,lc,eff}$ (see paragraph 6.4.2), while ΔK_{IIeff} is normalized in respect to the effective mode II threshold $\Delta K_{IIth,eff}$ for the shallow defect with √area =630 μm (the length of this defect is of the same order of the long crack characteristic size, this assumption is also supported by the fact that the mode I threshold of this defect was equal to the corresponding value for long cracks). The assumption that $\Delta K_{IIth} = \Delta K_{IIIth}$ [15] has also been considered. For the value of the effective threshold under simple shear see the discussion in *chapter 3*.

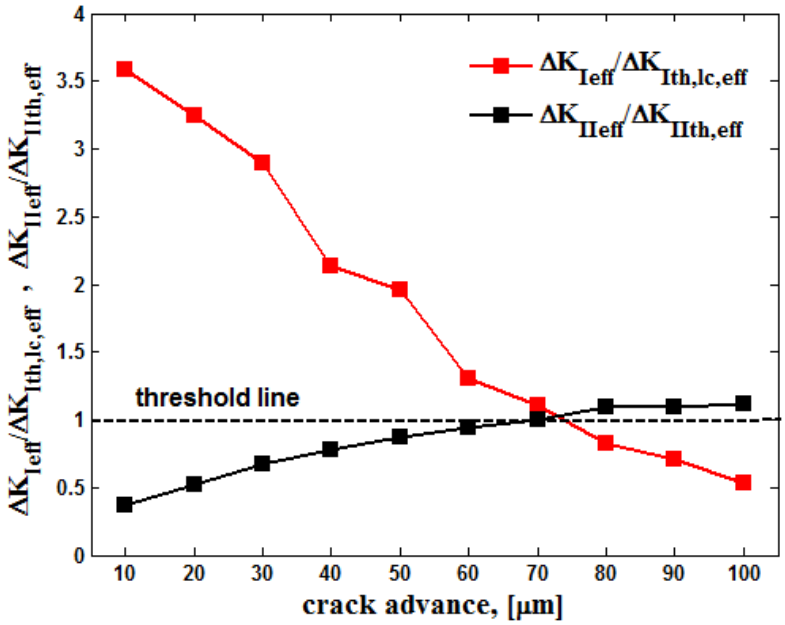

Figure 6.13. Tensile vs. shear driving forces as a function of the current crack length.

According to Figure 6.13, the fatigue crack propagation under OOP loads appears to be characterized by a complex propagation mechanism where two different stages can be distinguished: during the early stage of propagation, the crack growth is promoted by mode I under the residual tensile stresses produced by the cyclic compressive load; subsequently when the opening/closing phenomena at the crack tip vanish with increasing crack length, the crack grows by mode II.

Because of the increasing residual opening $\Delta U_{y,residual}$ between the crack lips while the crack extends (Figure 6.14), the shear attenuation (engendered by the sliding

interaction between the crack faces on the macroscopic crack plane) progressively diminishes as the current crack length increases.

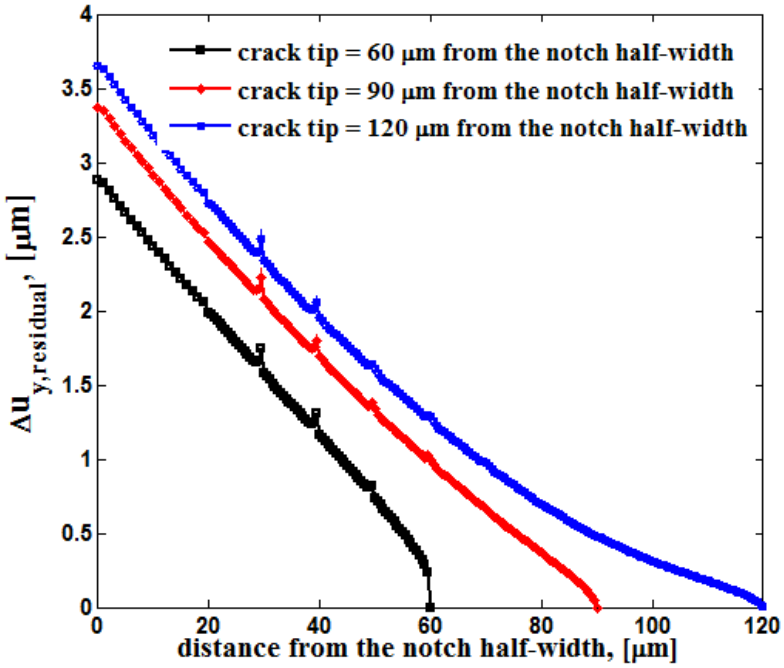

Figure 6.14. Residual opening displacement profile as increasing the crack length.

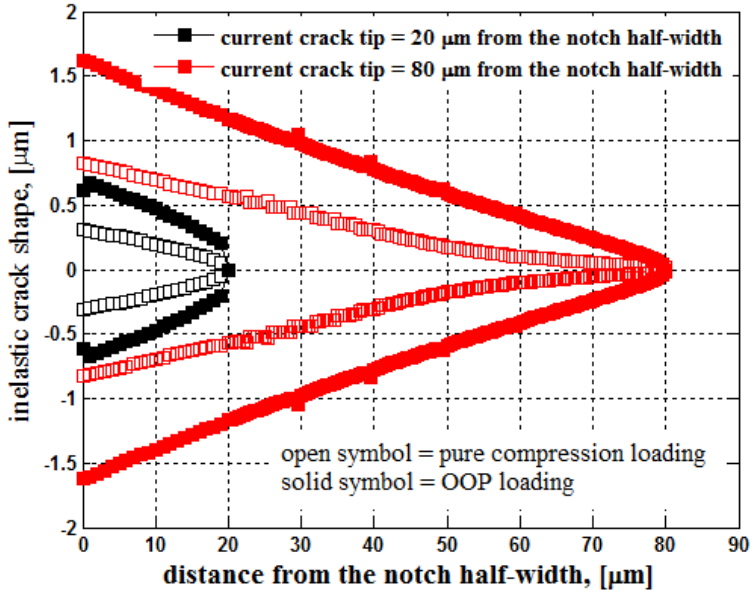

Figure 6.15. Comparison between the inelastic crack shapes under pure compression and OOP loading conditions as increasing the crack length.

Finally, a comparison between the inelastic shapes of a growing fatigue crack, under both pure compression and out-of-phase loading conditions, is depicted in Figure 6.15. During the early stage of propagation a blunt crack shape can be observed under both the above loading conditions. As long as the crack extends, the inelastic profile of the crack propagating from the notch half-width under far-field cyclic compression becomes progressively sharp and closed while approaching the crack tip. Oppositely, a blunt profile can be still observed when the crack is advanced under OOP loadings.

6.6 Conclusions

In the present chapter the role played by the far-field cyclic compression on crack propagation under rolling contact fatigue testing conditions has been investigated both numerically and experimentally.

A test on pre-cracked micro-notched specimen ($\sqrt{area}$ = 315 μm) under pure cyclic compressive loading has shown that the co-planar fatigue crack grew only few tens of μm before arresting completely. The co-planar crack arrest distance was not comparable with the enhanced crack extent measured after an out-of-phase test carried out by applying a lower compressive stress. Possible explanations of the enhanced co-planar crack growth based on mechanisms similar to the compression pre-cracking were then contradicted.

Furthermore FE elastic-plastic analyses with crack advance under both pure compressive and rolling contact testing conditions, have been conducted using ABAQUS on a 2D geometrical model in order to support the experimental findings. An elastic-plastic constitutive model with non-linear kinematic hardening, was used. The crack growth behaviour, under the above testing conditions, has been examined and compared in terms of crack tip shielding phenomena engendered by the plastic wake formed behind the crack tip.

FE elements results showed that:

- a “short crack effect” on the closure behaviour at the crack tip exist when the far-field compressive stress is applied (whatever it acts alone or

superimposed on the alternating torsion); for a fatigue crack initiating from the notch, little closure exist behind the crack tip on account of the limited plastic wake. As long as the crack extends, a progressive enhancement in crack closure is observed;

- under pure compression the length of the growing fatigue crack, at which closure phenomena decrease ΔK_{Ieff} to values below the effective mode I threshold for long cracks $\Delta K_{Ith,lc,eff}$,correspond well with the experimental crack arrest distance;
- under OOP loading, the leading mechanism (tensile vs. shear), governing the crack propagation behaviour, is found to be established by the competition between ΔK_{Ieff} and $\Delta K_{IIeff.}$ Two different stages of propagation can be distinguished: the crack growth is first promoted by mode I under the residual tensile stresses produced by the cyclic compressive load; subsequently the opening/closing phenomena at the crack tip vanish with increasing crack length and the crack propagation is then encouraged by shear.
- under OOP loading, the crack is always slipped and the shear attenuation (engendered by the sliding interaction between the crack faces on the macroscopic crack plane) progressively diminishes as the current crack length increases on account of the increasing residual opening $\Delta U_{y,residual}$ between the crack lips ;

Finally, the comparison between the inelastic shapes of a growing fatigue crack, under the above testing conditions, has shown that as long as the crack extends, the profile of the crack, which propagates from the notch half-width under far-field cyclic compression, becomes progressively sharp and closed while approaching the crack tip. Oppositely, a blunt profile is still observed under OOP loading as the crack extends.

Chapter 7
Conclusions

7.1 Summary

In this study the mechanism governing the shear-mode propagation of short fatigue cracks under mixed loadings simulating subsurface rolling contact fatigue conditions has been investigated. First, the crack growth behaviour under contact loadings has been examined experimentally: a novel test methodology, developed by Beretta et al [16], has been consolidated onto a bearing and a railway steels. The experimental procedure was directed to obtain mode III co-planar crack propagation data on pre-cracked specimens containing shallow micro-notches with $\sqrt{area} < 1000$ μm. The stress field, experienced by the material beneath the surface under contact loadings, has been simulated by adopting an out-of-phase load pattern, where the axial loading, always compressive, was shifted 90° in respect to the alternating torsion.
Under RCF testing condition, the experimental crack growth behaviour was found to be characterized by:

- an enhanced co-planar propagation; stable mode III crack growth was indeed observed at nominal ΔK_{III} much lower than ΔK_{Ith};
- a crack size dependency on the threshold values; in fact, the mode III thresholds decreased with a crack size decreasing;
- evidence of severe rubbing of the crack faces; a residual opening between the crack lips and the continuous emission of fretting debris, emerging from the crack during the tests, were observed.

Furthermore, few similarities have been found between the macroscopic appearance of the fracture surfaces under simple shear and rolling contact testing conditions. In

contrast with the faceted crack surface morphology under simple shear (characterized by a non-planar crack front, often rotated and segmented, i.e. “factory roof”), the OOP fracture surfaces were totally flat with evidence of shear rubbing marks parallel to the crack plane. A chromatic contrast, between the undamaged and the oxidized areas of the fatigue region, has been empathized after etching the co-planar surfaces in nital solution. Micro-structural changes were also found beneath the bearing steel contact surface, after sectioning and polishing, and dark etched areas (DEA) were indeed observed inside secondary cracks, developed along the coplanar crack depth and close to the notch region.

After having characterized experimentally the crack growth behaviour under RCF conditions, attempts have been done in order to clear up the mechanism encouraging the shear-mode propagation under the above testing condition. Firstly, it has been shown that a lack of similarity exists between torsional crack growth data and the experimental trend under RCF when the mode III crack growth behaviour is characterized by the nominal value of ΔK_{III}. In fact, on account of the sliding interaction between the microscopically rough fracture surfaces during cyclic shear loading, (which involve sliding, sticking and other abrasion phenomena), the nominal external value of ΔK_{III}, partly dissipated by friction, is reduced to a lower effective value. Crack growth data under simple shear were found to be consistent with the experimental trend under RCF only when the effect of crack face friction was taken into account through the exploitation of a micro-mechanical analytical model, based on assuming a 2D crack of depth *a* at the free surface of an elastic-plastic half space.

Secondly, the conditions required for the promotion of mode I/mode III crack branching have been examined theoretically by adopting a LEFM approach. It has been shown that the macroscopic appearance of the fracture surfaces (both under simple shear and RCF loading conditions) is established by the cracking mode dominating the competition between mode I and mode III failures, which in turn depends on the effective crack tip stress field. Since the stress field, actually experienced by the material at the crack tip, cannot be evaluated on the basis of the external loading only (on account of the crack sliding contact interaction, responsible for both the shear attenuation, i.e. the mode III SIF reduction to a lower effective

value, and the wedging open behaviour of the crack surface asperities, i.e. the generation of a positive mode I SIF), a model for crack sliding interaction under simple shear and mixed I+III loading has been developed at this scope.

Finally, the role played by the far-field cyclic compression on the promotion of co-planar crack growth under RCF conditions has been investigated both numerically and experimentally. It has been shown that when the axial loading superimposed to the alternating torsion is not entirely compressive, the macroscopic appearance of the fracture surface resemble a "factory-roof" type, thereby indicating that the enhanced co-planar propagation could actually be promoted by the out-of-phase scheme only. Furthermore, a test under pure cyclic compression has shown that the co-planar fatigue crack grew only few tens of μm before arresting completely.

The effects of crack tip shielding phenomena induced by the plasticity on the crack growth behaviour under both pure compressive and rolling contact testing conditions, have been also inspected by FE elastic-plastic analyses with crack advance. FE elements results showed that:

- a "short crack effect" on the closure behaviour at the crack tip exist when the far-field compressive stress is applied (whatever it acts alone or superimposed on the alternating torsion); for a fatigue crack initiating from the notch, little closure exist behind the crack tip on account of the limited plastic wake. As long as the crack extends, a progressive enhancement in crack closure is observed;
- under OOP loading, the leading mechanism (tensile vs. shear), governing the crack propagation behaviour, is found to be established by the competition between ΔK_{Ieff} and $\Delta K_{IIeff.}$ The crack growth is first promoted by mode I under the residual tensile stresses produced by the cyclic compressive load; subsequently when the opening/closing phenomena at the crack tip vanish with increasing crack length, the crack propagation is then encouraged by shear.

7.2 Contributions

The contributions given by the current study on the understanding of the mechanism of crack propagation encouraged by shear under rolling contact fatigue condition can be summarized as follows:

- short crack fatigue assessments under RCF conditions have been obtained onto a bearing and railway steels; until now only “experimentally” derived shear growth data on small defects have been incorporated into RCF models for subsurface fatigue;
- a comparison between crack growth data and thresholds under simple shear and RCF conditions has been provided;
- the competition between the cracking modes (tensile vs. shear) dominating the macroscopic fracture appearance under both simple shear and RCF conditions has been examined through the exploitation of a micro-mechanical model for crack sliding interaction under anti-plane shear (both pure mode III and mixed I+III loadings);
- the role of the far field compression on crack propagation under RCF conditions has been clarified.

7.3 Recommendations for prospective research

On the basis of the current study, the following aspects are indicated as possible topics of prospective research:

- experimental measurements of mode III kinetic data, which can be incorporated into the theoretical model developed for the analysis of the crack sliding interaction effects;
- theoretical and experimental investigation on the changing aspect-ratio of the semi-elliptical crack propagated under RCF testing conditions;

- short crack fatigue growth assessments obtained testing cylindrical specimens with shallow defects parallel to the sample longitudinal axis under RCF conditions;
- short crack fatigue growth assessments under RCF conditions on micro-notched sample where crack-like thin slits are introduced by FIB technique;
- development of a 3D micro-mechanical model for crack sliding interaction under pure mode III and mixed I+III loadings;
- numerical investigations on the crack tip shielding phenomena, induced by plasticity under RCF loading conditions, where the roughness of the crack flanks is included.

References

[1] Otsuka A, Sugawara H, Shomura M. *A test method for mode II crack growth relating to a model for rolling contact fatigue*. Fatigue Fract Engng Mater Struct; 1996; 19-10: 1265-1275.

[2] Otsuka A, Fuji Y, Maeda K. *A new testing method for mode II fatigue crack growth relating to a model for rolling contact fatigue*. Fatigue Fract Engng Mater Struct; 2004; 27: 203-212.

[3] Beretta S, Donzella G, Roberti R, Ghidini A. *Contact fatigue propagation of deep defects in railway wheels*. In: Proceedings of the 13th European Conference on Fracture - ECF13. 2000; 3R: 147.

[4] Vincent A, Lormand G, Lamagnèere P, Gosset L, Girodin D, Dudragne G, Fougeres R. *From white etching areas around inclusions to crack nucleation in bearing steels under rolling contact fatigue*. Bearing Steel STP 1327; 1998; 108-123.

[5] Murakami Y, Sakae C, Hamada S. *Mechanism of rolling contact fatigue and measurements of ΔK_{IIth} for steels*. Engng Against Fatigue; 1999; 473-485.

[6] Doquet V, Pommier S. *Fatigue crack growth under non proportional mixed-mode loading in ferritic-pearlitic steel*. Fatigue Fract Engng Mater Struct; 2004; 27: 1051-1060.

[7] Murakami Y. Metal Fatigue. *Effects of small defects and non-metallic inclusions*. Oxford: Elsevier; 2002.

[8] Campbell JP, Ritchie RO. *Mixed mode high-cycle fatigue crack growth thresholds in Ti-6Al-4V. A Comparison of large- and short-crack behaviour*. Engineering Fracture Mechanics; 2000; 67:209-227.

[9] Suresh S, Ritchie RO. *Propagation of short fatigue cracks*. Int Metals Rev; 1984; 29:445-476.

[10] Christman T, Suresh S. *Crack initiation under far-field cyclic compression and the study of short fatigue cracks*. Engineering Fracture Mechanics; 1985; 23; 6: 953-964.

[11] Tallian TE. *On competing failure modes in rolling contact*. ASLE Transactions, 1967; 10; 4: 418-439.

[12] Keer L M, Bryant M D, Haritos G K. *Subsurface and surface cracking due to Hertzian contact. Journal of Lubrication technology*; 1982; 104: 347-351.

[13] Matsunaga H, Shomura N, Muramoto S, Endo M. *Shear mode threshold for a small fatigue crack in a bearing steel*. Fatigue Fract Engng Mater Struct; 2010; 34: 72-82.

[14] Guy P, Meynaud P, Vincent A, Baudry G. *Sub-surface damage investigation by high frequency ultrasonic echography on 100Cr6 bearing steel*. Tribology International; 1997; 30: 247-259.

[15] Murakami Y, Fukushima Y, Toyama K, Matsuoka S. *Fatigue crack path and threshold in Mode II and Mode III loadings*. Engineering Fracture Mechanics; 2008; 75: 306-318.

[16] Beretta S, Foletti S, Valiullin K. *Fatigue crack propagation and threshold under out-of phase multiaxial loading in a gear steel*. Engineering Fracture Mechanics; 2010; 77:1835-1848.

[17] Akhurst KN, Lindley TC, Nix KJ. *The effect of mode III loading on fatigue crack growth in a rotating shaft*. Fatigue Fract Engng Mater Struct; 1983; 5: 345-348.

[18] Liu S, Chao Y J, Zhu X. *Tensile-shear transition in mixed-mode I/III fracture*. International Journal of solids and Structures; 2004;41:6147-6172.

[19] Suresh S, Tschegg EK. *Combined mode I-mode III fracture of fatigue-precracked alumina*. Journal of American Ceramic society 70; 1987; 10: 726-733.

[20] Tschegg EK, Suresh S. *Mode III fracture of 4340 steel: effects of tempering temperature and fracture surface interference*. Metallurgical Transactions A; 1988; 19A: 3035-3044.

[21] Ritchie RO, Mc Clintock FA, Tshegg EK, Nayeb-Hashemi H. *Mode III Fatigue Crack Growth under Combined Torsional and Axial Loading*. Multiaxial Fatigue ASTM STP 853; 1985; 203-227.

[22] Yates JR, Miller KJ. *Mixed mode (I+III) fatigue thresholds in a forging steel*. Fatigue Fract Engn Mater Struct; 1989; 12-3: 259-270.

[23] Tong J, Yates JR, Brown M. *Some aspects of fatigue threshold under mode III and mixed mode III and I loadings*. International Journal of Fatigue; 1996;18-5: 279-285.

[24] Nayeb-Hashemi H, Mc Clintock FA, Ritchie RO. *Micro-mechanical modelling of mode III fatigue crack growth in rotor steels*. International Journal of Fracture; 1983; 23:163-185.

[25] Tshegg EK, Ritchie RO, Mc Clintock FA. *On the influence of rubbing of rubbing fracture surfaces on fatigue crack propagation in mode III. International Journal of Fatigue*; 1983; 5-1: 29-35.

[26] Tschegg EK. *A contribution to Mode III fatigue crack growth*. Material Science and Engineering; 1982; 54: 127-136.

[27] Murakami Y, Takahashi K, Kusumoto R. *Threshold and growth mechanism of fatigue cracks under mode II and mode III loadings*. Fatigue Fract Engng Mater Struct; 2003; 26:523-531.

[28] Pokluda J, Slamecka K, Sandera P. *Mechanism of factory roof formation*. Engineering Fracture Mechanics; 2010; 77-11: 1763-1771.

[29] Valiullin K. *Multiaxial fatigue in presence of defects*. Ph.D. thesis. Politecnico di Milano; 2010.

[30] Tarantino MG, Beretta S, Foletti S, Lai J. *A comparison of Mode III threshold under simple shear and RCF conditions*. Engineering Fracture mechanics; 2011; 78:1742-1755.

[31] Hellier AK, Corderoy DJH, McGirr MB. *Some observations on mode III fatigue thresholds*. International of Fracture. 1985; 29: R45-R48.

[32] Beretta S, Foletti S, Valiullin K. *Fatigue strength for shallow defects/cracks in torsion*. International Journal of Fatigue; 2011; 33: 287-299.

[33] Kassir MK, Sih GC. *A three-dimensional stress distribution around an elliptical crack under arbitrary loadings*. Journal of Applied Mechanics; 1966; 33: 601-611.

[34] Graboulov A, Petrov R, Zandebergen HW. *EBSD investigation of the crack initiation and TEM/FIB analyses of the microstructural changes around the cracks formed under Rolling Contact Fatigue*. International Journal of fatigue; 2010; 32: 576-583.

[35] Pinna C, Doquet V. *The preferred fatigue crack propagation mode in a M250 maraging steel*. Fatigue Fract Engng Mater Struct; 1999; 22: 173-183.

[36] Melin S. *When does a crack grow under mode II conditions?* International Journal of Fatigue; 1986; 20:103-114.

[37] Tschegg EK. *Sliding mode crack closure and mode III fatigue crack growth in mild steel*. Acta metallurgica; 1983; 31-9: 1323-1330.

[38] Beretta S. *Propagation of short cracks in a high strength steel for railway axles*. In: Proc ECF14 conference; 2002; Cracow.

[39] Tada H, Paris P, Irwin G. *The stress analysis of crack handbook (2nd edition)*. Paris Production (and Del research). 1975; St Louis; Missouri; U.S.A.

[40] Newmann Jr JC. *A crack closure model fro predicting fatigue crack growth under aircraft spectrum loading*. ASTM STP 748; 1981:53-84.

[41] Suresh S, Ritchie RO. *A geometrical model for fatigue crack closure induced by fracture surface roughness*. Metallurgical and Materials Transactions A; 1982; 13-9: 1627-1631.

[42] Minakawa K, McEvily AJ. *On near-threshold fatigue crack growth in steels and aluminium alloys*. In: International Symposium on Fatigue Thresholds; 1981; Stockholm; Sweden; 2: 36.1-36.19.

[43] Walker N, Beevers CJ. *A fatigue crack growth mechanism in titanium*. Fat Fract Engng Mater struct; 1979; 1: 135-148.

[44] Gross TS, Mendelsohn D. *On the effect of crack face contact and friction due to fracture surface roughness in edge cracks subjected to external shear*. Engineering Fracture mechanics; 1988; 31: 405-420.

[45] Gross TS, Mendelsohn D. *An analysis of frictional effects on cylindrical mode III fatigue crack propagation specimens*. Fatigue Fract Engng Mater Struct; 1988; 11:167-178.

[46] Vaziri A, Nayeb-Hashemi H. *The effect of crack surface interaction on the stress intensity factor in Mode III crack growth in round shafts*. Engineering Fracture Mechanics; 2005; 72: 617-629.

[47] Suresh S, Zamiski GF, Ritchie RO. *Oxide-induced crack closure: an explanation for near-threshold corrosion fatigue crack growth behaviour*. Metallurgical Transactions A; 1981, 12: 1435-1443.

[48] Goulet RU, Gross TS, Mendelsohn D. *Evidence of fracture surface interference in shear detected by phase-shifted speckle interferometry*. Metallurgical and Materials Transactions A; 1995; 27A: 3853-3860.

[49] Beevers CJ, Bell K, Carlson RL, Starke EA. *A model for fatigue crack closure*. Engineering Fracture Mechanics; 1984; 19-1: 93-100.

[50] Carlson RL, Beevers CJ. *A mixed mode fatigue crack closure model*. Engineering Fracture Mechanics; 1985; 22-4: 651-600.

[51] Ballarini R, Plesha ME. *The effects of crack surface friction and roughness on the crack tip stress fields*. International Journal of Fracture; 1987; 34: 195-207.

[52] Smith MC, Smith RA. *Toward an understanding of mode II fatigue crack growth*. In: Basic Questions in Fatigue ASTM STP 924; American Society for Testing and Materials; Philadelphia 1988; 1; 260-280.

[53] Smith MC, Smith RA. Modelling the unlocking and slip of crack surfaces under mode II loading. In: Proceedings 6th International Conference on Fracture; Delhi; December 1984.

[54] Yu X, Abel A. *Modelling of crack surface interference under cyclic shear loads*. Fatigue Fract Engng Mater Struct; 2002; 22: 205-213.

[55] Yu X, Abel A. *Crack surface interference under cyclic mode I and steady mode II loading*. Engineering Fracture Mechanics; 2000; 66: 519-535.

[56] Tong J, Yates JR, Brown MW. *A model for sliding mode crack closure*. Engineering Fracture Mechanics; 1995; 52-4: 599-611.

[57] Mendelsohn D, Gross TS, Zhang Y. *Fracture surface interference in shear-I. A model based on experimental surface characterizations*. Acta Metall Mater; 1994; 43-3: 893-900.

[58] Gross TS, Mendelsohn D. *Mode I stress intensity factors induced by fracture surface roughness under pure mode III loading: application to the effect of*

loading modes on stress corrosion crack growth. Metallurgical Transactions A; 1989; 20A: 1989-1999.

[59] Elber W. *Fatigue crack closure under cyclic tension*. Engineering Fracture Mechanics; 1970; 2; 37-45.

[60] Hartrant RJ, Sih GC. *Alternating method applied to edge and surface crack problems*. Methods of Analysis and Solutions of crack problems. Noordhoff International; 1973.

[61] Hurd NJ, Irving PE. *Factors influencing propagation of mode III fatigue cracks under torsional loading*. In: Design of Fatigue and Fracture resistant structures. Abelkis Hudson editors; 1982: 212-233.

[62] Richard HA, Fulland M, and Sander M. *Theoretical crack path prediction*. Fat. Fract. Engng Mater. Struct.; 2005; 28: 3-12.

[63] McClung RC, Sehitoglu H. *On the finite element analysis of fatigue crack closure-1. Basic modelling issues*. Engineering Fracture Mechanics; 1989; 33-2: 237-252.

[64] Rice JR. *Mechanics of crack-tip deformation and extension by fatigue*. In Fatigue Crack propagation ASTM STP; 1967; 415: 247-311.

[65] Newman Jr JC. *A finite-element analysis of fatigue crack closure*. ASTM STP 590; 1976: 281-301.

[66] Solanki K, Daniewicz SR, Newman Jr JC. *Finite element modelling of plasticity-induced crack closure: an overview*. Engineering Fracture Mechanics; 2004; 71: 149-171.

[67] McClung RC, Sehitoglu H. *On the finite element analysis of fatigue crack closure-2. Numerical results*. Engineering Fracture Mechanics; 1989; 33-2: 253-272.

[68] Fleck NA. *Finite element analysis of plasticity-induced crack closure under plane strain conditions*. Engineering Fracture Mechanics; 1986; 25-4: 441-449.

[69] Blom AF, Holm DK. *An experimental and numerical study of fatigue crack closure*. Engineering Fracture Mechanics; 1985; 22: 997-1011.

[70] Ogura K, Ohji K. *FEM analysis of crack closure and delay effect in fatigue crack growth under variable amplitude loading*. Engineering Fracture Mechanics; 1977; 9: 471-480.

[71] Ogura K, Ohji K, Honda K. *Influence of mechanical factors on fatigue crack closure*. Advances in Research on the Strength and Fracture of Materials (Fracture 1977); ICF4; Waterloo; Canada; 2B: 1035-1047.

[72] Lalor PL, Sehitoglu H. *Fatigue crack closure outside small scale yielding regime.* Mechanics of Fatigue Crack Closure; ASTM STP 982; 1988; 342-360.

[73] McClung RC, Thacker BH, Roy S. *Finite element visualization of fatigue crack closure in plane stress and plane strain*. International Journal of Fracture; 1991; 50: 27-49.

[74] Wu J, Ellyin F. *A study of fatigue crack closure by elastic-plastic finite element analysis for constant-amplitude loading*. International Journal of Fracture; 1996; 82: 43-65.

[75] Sehitoglu H, Gall K, Garcìa AM. *Recent advances in fatigue crack growth modelling*. International Journal of Fracture; 1996; 80: 165-192.

[76] Pommier S, Bompard Ph. *Baushinger effects of alloys and plasticity-induced crack closure: a finite element analysis*. Fatigue Fract Engng Mater Struct; 2000; 23: 129-139.

[77] Skorupa M. *Load interaction effects during fatigue crack growth under variable amplitude loading- a literary review. Part I. empirical trends*. Fatigue Fract Engng Mater Struct; 1998; 21: 987-1006.

[78] Chaboche JL. *Viscoplastic constitutive equations for the description of cyclic and anisotropic behaviours of metals*. Bull. L'Academie Polonaise Des Sci. Series des Sciences et Techniques XXV; 1977; 1: 33-41.

[79] Suresh S. *Crack initiation in cyclic compression and its application*. Engineering Fracture Mechanics; 1985; 21-3: 453-463.

[80] Rice JR. *Mathematical analysis in the mechanics of fracture*. In: Fracture of solids: fracture of solids. Edited by Liebowitz H; New York USA; 1969; 2: 218-221.

Appendix A
Railway steel fatigue crack growth assessments under RCF conditions

A.1 Introduction

This appendix is devoted to the mode III fatigue crack growth assessments onto a railway steel under rolling contact loadings. Analogously to the fatigue assessments onto the bearing steel (see *chapter 2*), the crack growth curves were obtained after testing in ambient air cylindrical micro-notched specimens under an out-of-phase load path, which simulate sub-surface RCF stress conditions. The crack size dependency on the threshold values has also been investigated by introducing shallow defects with different sizes. The novel experimental methodology developed by Beretta et al [16] has been adopted.

Finally, the macroscopic appearance of the co-planar crack fracture surfaces has been examined after etching in nital solution and the micro-structural changes, eventually occurring beneath the contact surface, were inspected after sectioning and polishing.

A.2 Experimental details

A.2.1 Material

The material analyzed is perlitic railway steel. The monotonic and cyclic mechanical properties are reported in Table A.1. The material showed a strain hardening behaviour when subjected to cyclic loading.

	E	UTS [MPa]	$\sigma_{y\ 0.2\%}$ [MPa]	$\sigma_{y,\ cyclic\ 0.2\%}$[MPa]
Railway steel	206000	874	545	482

Table A.1 Railway steel mechanical properties.

A.2.2 Specimens

All fatigue tests were carried out on pre-cracked micro-notched hourglass specimens. Two defects sizes, expressed in terms of Murakami's √area parameter, equal to 630 μm and 220 μm were considered. The geometry of the specimens and the micro-notches adopted have been already reported in *chapter 2*. The sample preparation procedure was the same used for the bearing steel: all specimens were first electro-polished (to avoid the effect of the surface residual stresses) before introducing the artificial micro-notches by EDM. In order to promote coplanar crack propagation, a preliminary mode I fatigue test pre-cracking procedure was adopted: all specimens were subjected to push-pull axial fatigue for 10^7 cycles with a stress ratio R= -2 and at a stress level close to the range of the mode I stress intensity factor fatigue threshold ΔK_{Ith}. The success of the pre-cracking procedure was always verified by SEM before starting the test.

A.2.3 Fatigue tests

After the pre-cracking procedure, the specimens were subjected to multiaxial fatigue tests; the tests were conducted in force/torque control (at a frequency of 8 Hz) by means of an MTS 809 Axial Torsional System following the experimental procedure previously described in *chapter 2*. The out-of-phase load pattern (already adopted to test the bearing steel under RCF conditions) was employed and the loading amplitudes were defined by sinusoidal periodic functions into the test rig controlling software. The surface-mixed mode crack advance was constantly monitored during the test by employing the method of *plastic-replicas*.

Following the fatigue test, all the specimens were examined under SEM after having removed the debris clopping the defect by intense ultrasonic cleaning in acetone. Both

the specimen surface appearance and the co-planar fracture surface morphology were investigated (the latter inspected after static cryogenic rupture in liquid hydrogen).

A.3 Fatigue tests results

Following an examination of the co-planar fracture surfaces, it appears clear that the out-of phase loading scheme promotes mode III co-planar crack growth, owing to the fact that continuous mode III propagation was observed at ΔK_{III} levels much lower than mode I threshold (see Figure A.1). Fatigue tests results onto the railway steel fully confirm results onto the bearing steel (*chapter 2*).

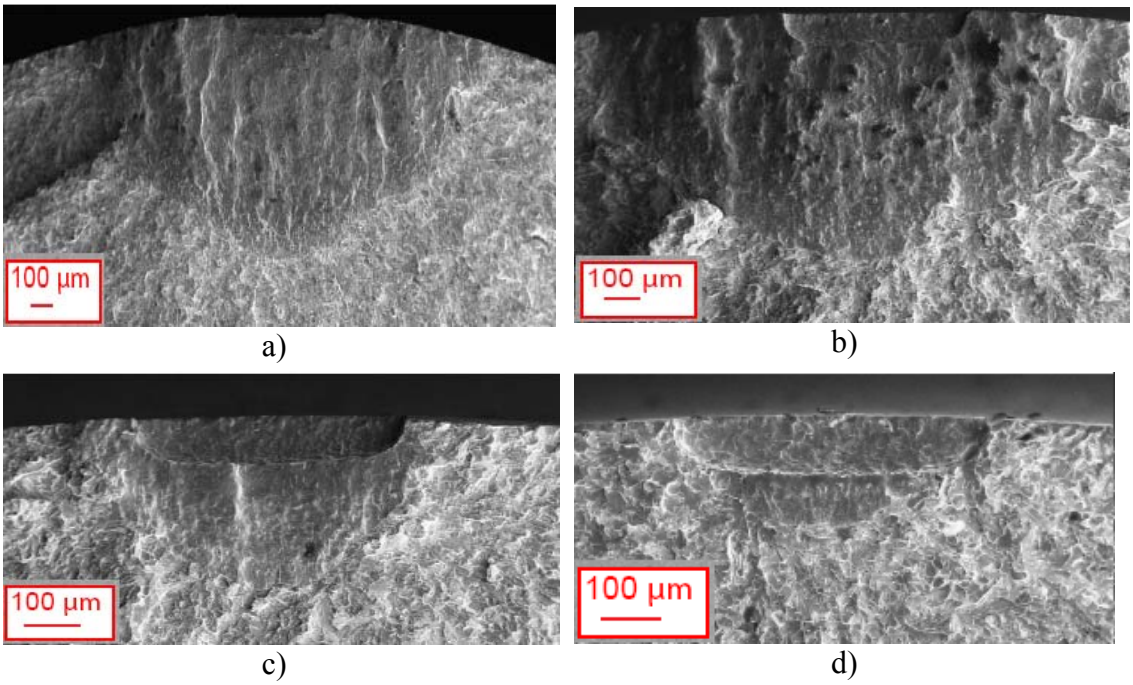

Figure A.1. Mode III fracture surfaces for micro-notches of √area = 220 µm specimen tested at: a) $\Delta K_{III}/\Delta K_{Ith}$ = 1.2 for N = $6 \cdot 10^4$ cycles; b) $\Delta K_{III}/\Delta K_{Ith}$ = 1 for N = $1.2 \cdot 10^5$ cycles; c) $\Delta K_{III}/\Delta K_{Ith}$ = 0.8 for N = $1.2 \cdot 10^5$ cycles; d) $\Delta K_{III}/\Delta K_{Ith}$ = 0.6 for N = $5 \cdot 10^5$ cycles.

Furthermore, following an examination of the specimens surfaces some differences, with the bearing steel samples surface appearance, could be detected: while in tests where $\Delta K_{III} < \Delta K_{Ith}$ no appreciable surface crack growth is noted (consistently with the bearing steel fatigue test results), the development of mode I tilted cracks along the crack front is not observed at $\Delta K_{III} > \Delta K_{Ith}$, see Figure A.2.

Moreover, although there is evidence of plastic deformation and rubbing of fracture lips (see Figure A.3), the residual opening between the crack lips appears less prominent in comparison with the amount of opening observed after OOP tests onto the bearing steel.

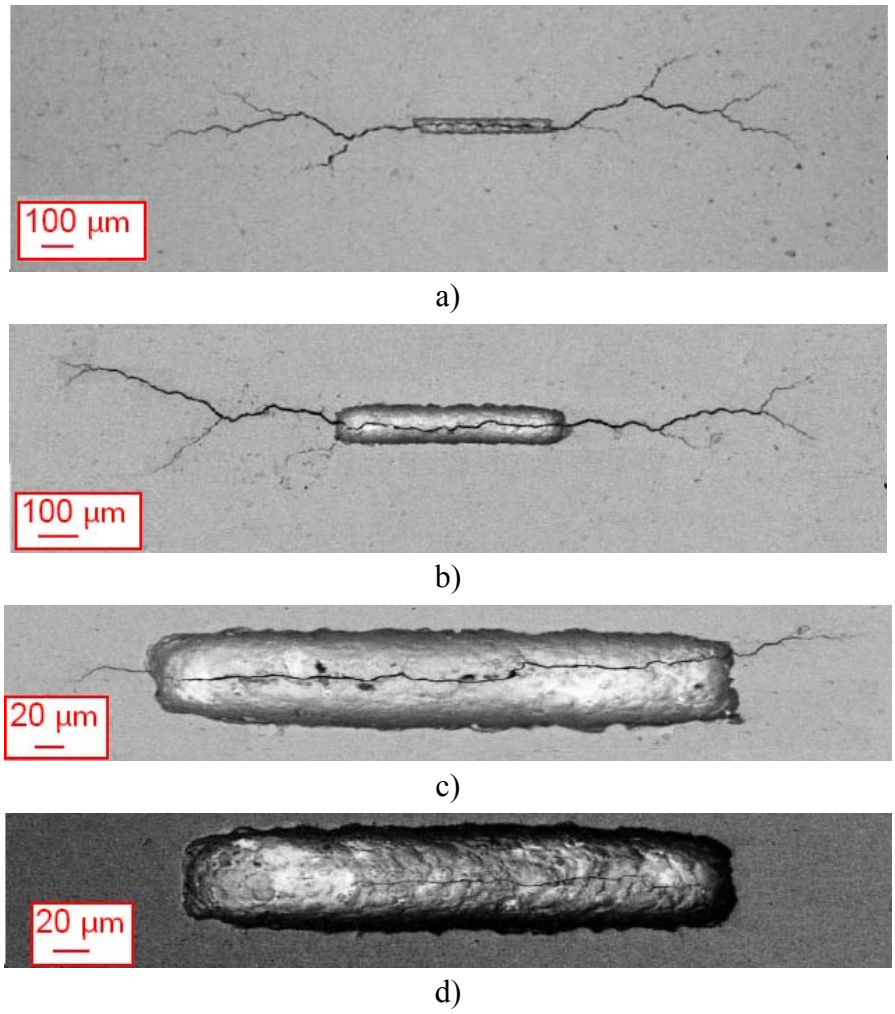

Figure A.2. Specimen surfaces for micro-notches of √area = 220 µm specimen tested at: a) $\Delta K_{III}/\Delta K_{Ith} = 1.2$ for $N = 6 \cdot 10^4$ cycles; b) $\Delta K_{III}/\Delta K_{Ith} = 1$ for $N = 1.2 \cdot 10^5$ cycles; c) $\Delta K_{III}/\Delta K_{Ith} = 0.8$ for $N = 1.2 \cdot 10^5$ cycles; d) $\Delta K_{III}/\Delta K_{Ith} = 0.6$ for $N = 5 \cdot 10^5$ cycles.

During fatigue tests the emission of debris emerging from the crack was also noted. Consistently with the discussion developed in *chapter 2*, the presence of debris has to be attributed to the abrasion process engendered by the interaction of the sliding rough crack surfaces during anti-plane shear.

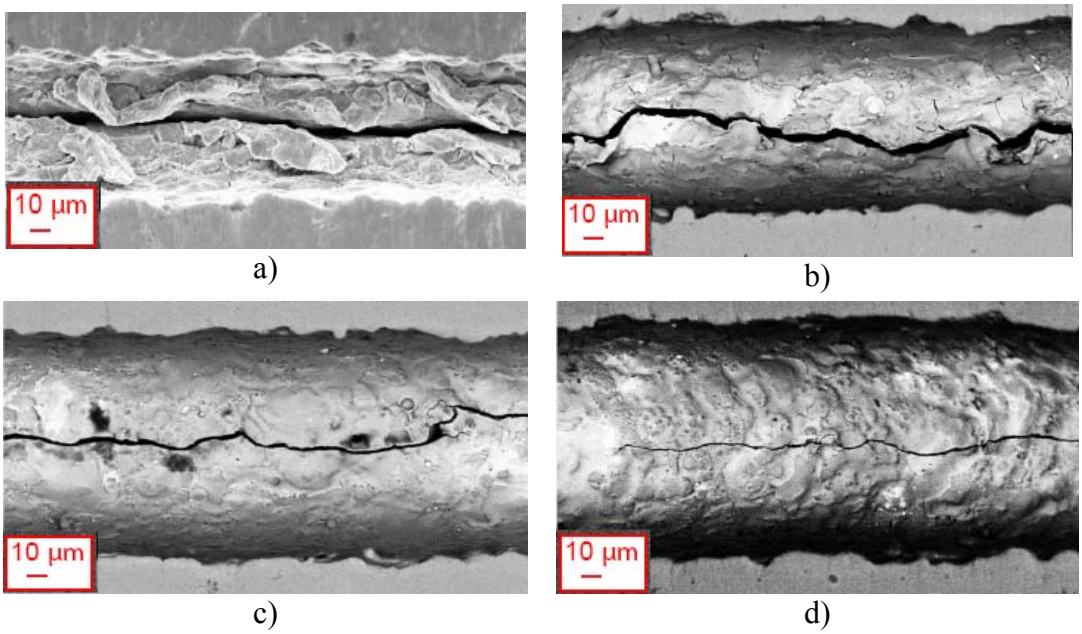

Figure A.3. Evidence of crack lips opening for micro-notches of √area = 220 µm specimen tested at: a) $\Delta K_{III}/\Delta K_{Ith} = 1.2$ for $N = 6 \cdot 10^4$ cycles; b) $\Delta K_{III}/\Delta K_{Ith} = 1$ for $N = 1.2 \cdot 10^5$ cycles; c) $\Delta K_{III}/\Delta K_{Ith} = 0.8$ for $N = 1.2 \cdot 10^5$ cycles; d) $\Delta K_{III}/\Delta K_{Ith} = 0.6$ for $N = 5 \cdot 10^5$ cycles.

The mode III crack growth rates, expressed in terms of nominal mode III stress intensity factor range ΔK_{III}, are reported in Figure A.4. The method used to compute both the nominal SIF [32] and the co-planar crack growth rates has been described in *chapter 2*. The threshold condition is again defined by the nominal mode III stress intensity range at which a absent co-planar propagation is observed.

The crack size dependency on the railway steel threshold value under out-of-phase loading is less prominent in comparison with the short crack effect observed onto the bearing steel. According to Figure A.4, the mode III threshold values slightly decrease with crack size decreasing.

A.4 Analysis of the fracture surfaces

The fracture surfaces have been carefully observed both under optical and scanning electron microscopes in order to inspect the presence of micro-structural changes, eventually occurring in the material beneath the fatigue region.

It has been shown in *chapter 2* that during fatigue crack growth promoted by shear, the changed microstructure is more dark in shading compared with the typical WEA

and butterflies. Furthermore, chemical analyses on the dark gray areas, have also revealed the presence of oxygen in the oxidized thick layers. Dissipative oxidation phenomena were, in fact, observed during the tests through the emission of fretting debris, emerging from cracks.

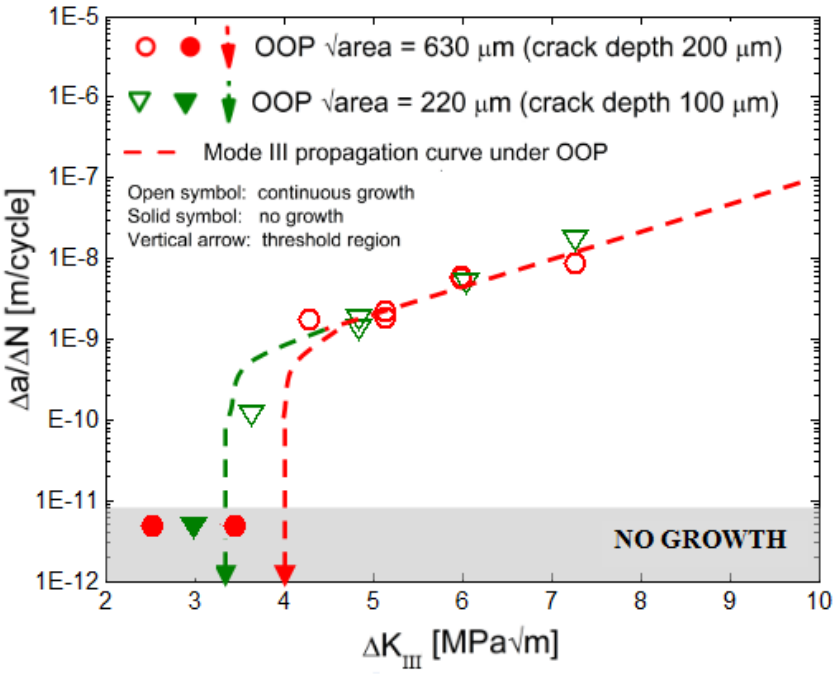

Figure A.4. Coplanar mode III average propagation rates: multiaxial fatigue tests vs. pure torsional fatigue test results in terms of ΔK_{III}.

At this purpose metallurgical and chemical analyses have been carried out. The co-planar fracture surfaces have been first etched in a nital acid solution (nital 0.2 %), and then observed under SEM at high magnifications. Figure A.5 shows the etched co-planar surface of a micro-notch √area = 220 μm tested at $\Delta K_{III}/\Delta K_{Ith}$ = 0.8 (test interrupted at N = 1.2 x 10^5 cycles). The chromatic contrast between "light" and "dark" gray areas is less emphasized than in the bearing steel; moreover, the undamaged micro-structure cannot be detected as in the bearing steel, where the carbides were clearly distinguished.

Both light and dark gray areas of the co-planar fatigue region have been analysed in order to inspect the chemical compositions. Chemical analyses were also directed to reveal the presence/absence of oxygen in the co-planar fatigue region. Two arbitrary

spots are chosen, they are referred as spot "A" and "B" respectively. Results are reported in Table A.2 and Table A.3.

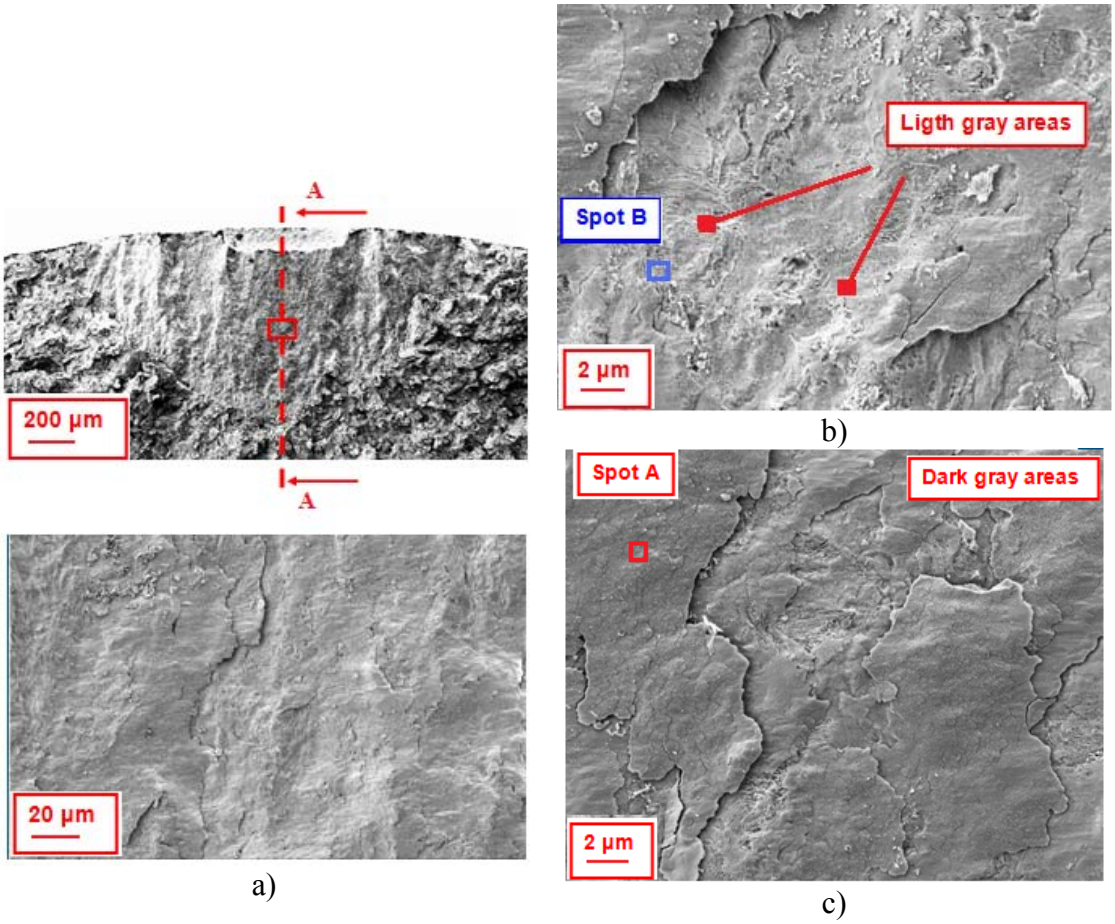

Figure A.5. Mode III surface SEM observations of a micro-notch √area = 220 µm tested at $\Delta K_{III}/\Delta K_{Ith} = 0.8$ for N = 1.2 x 10^5 cycles: a) fracture surface and high magnification (500 x) of the framed area after etching in nital solution; b)-c) magnifications (2000 x) of the framed area in a) revealing the undamaged and damaged microstructure respectively.

Oxygen can be detected in both spots A and B, thereby indicating that dissipative oxidation phenomena involve all the co-planar fatigue region. Nevertheless, the thick dark gray layers are more oxidized in comparison with the surrounding light gray areas: the weight percentage of oxygen in spot A is almost double than the corresponding value in spot B.

Furthermore, besides the examination of the co-planar fatigue region, the mode III fracture surfaces have been also sectioned and polished in order to inspect micro-structural changes eventually occurring beneath the fatigue region.

	C [%]	O [%]	Fe [%]
Spot A	3	24.18	72.82

Table A.2. Weight % of the elements present in spot A.

	C [%]	O [%]	Fe [%]
Spot B	4.52	13.18	82.29

Table A.3. Weight % of the elements present in spot B.

Figure A.6 reports the etched micro-structure of the central section A-A in Figure A.5. No secondary branched cracks, with evidence of DEA, can be noted along the co-planar crack depth, contrarily to what observed onto the bearing steel, and the micro-structure beneath the co-planar surface appears to be characterized by the bended perlitic bands (at 4000x magnification).

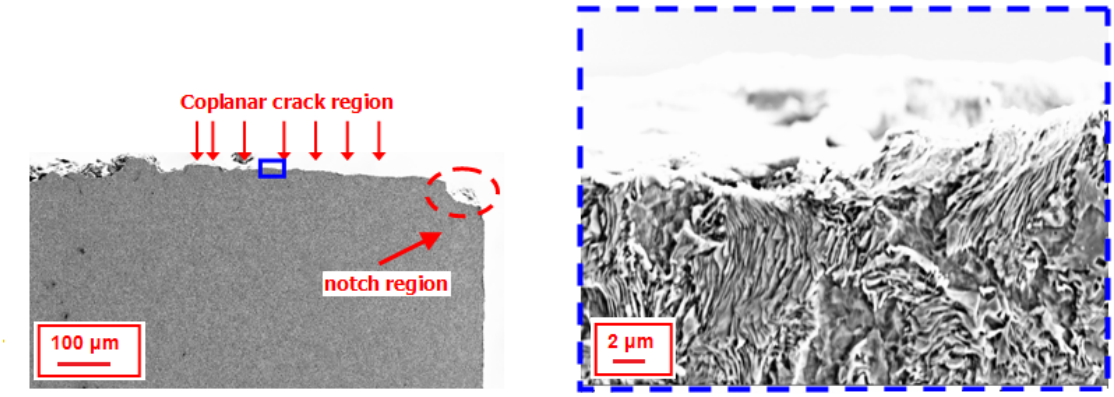

Figure A.6. Observation under SEM of the etched section A-A in Figure A.5: evidence of bended perlitic bands at high magnification (4000x).

A.5 Conclusions

The mode III fatigue crack growth assessments under rolling contact testing conditions, have been obtained onto a ductile railway steel. The novel experimental methodology, developed by Beretta et al in [16] and already consolidated onto a bearing steel material in *chapter 2*, has been employed.

Fatigue test results on the railway steel pre-cracked specimens containing shallow micro-notches (with √area < 1000 μm) confirmed that:

- the out-of-phase pattern enhances the co-planar crack growth owing to the fact that continuous mode III propagation was observed at ΔK_{III} levels much lower than mode I threshold;
- the crack size dependency on the railway steel threshold value is less prominent in comparison with the short crack effect observed onto the bearing steel;
- the enhancement of the co-planar crack growth under RCF conditions is associated with rubbing of the crack faces and a residual opening between the crack lips is also observed.

Following the optical and SEM observations of the co-planar fatigue region appearance (after etching in nital solution), the chromatic contrast between “light” and “dark” gray areas was found to be less emphasized than in the bearing steel: the undamaged micro-structure could not be detected and evidence of oxidation phenomena was revealed by the presence of oxygen both in dark and light gray areas. Finally, after sectioning and polishing the micro-structure beneath the contact surface was found to be characterized by bended perlitic bands and no secondary cracks with evidence of DEA was observed.

Appendix B

Closed-form expressions

In this appendix closed-form expressions for the effective mode I/mode III displacements at the notch depth have been obtained. For the sake of simplicity, the mathematical expressions have been obtained in the case of downhill sliding occurring at the right-hand facet ($\theta > \alpha$ has also been assumed). Nevertheless, the closed form-expressions for the other different movement situations can be obtained in the same manner.

Since the system of equations (4.1)-(4.11) has to be solved iteratively, at the first step of the numerical procure the effective mode III displacement $2u_{IIIeff}$ at the notch depth is assumed to be equal to the nominal mode III displacement $2u_{III0}$, i.e.:

$$2u_{III,eff}^{(1)}\left(x=b\right)=2u_{III\,0}\left(x=b\right) \tag{B.1}$$

In what follows, it is understood that both mode I and mode III displacements are calculated at the notch depth, i.e. (x = b) is then omitted.

Consequently, the effective mode I displacement is:

$$2u_{Ieff}^{(1)}=2u_{IIIeff}^{(1)}\cdot\tan\theta=2u_{III\,0}\cdot\tan\theta=2u_{I\,0}+2u_{Iw}^{(1)} \tag{B.2}$$

According to Eqs.(4.15)-(4.16) , the following expressions are obtained:

$$2u_{1w}^{(1)}=\frac{4a}{\pi E^{'}}h_I\left(b/a\right)p^{(1)}\left(x=a\right)=2u_{III\,0}\tan\theta-2u_{I\,0} \tag{B.3}$$

$$2u_{IIIf}^{(1)} = \frac{4a}{\pi G} h_{III}\left(b/a\right) q_f^{(1)}\left(x = a\right) \tag{B.4}$$

The normal and tangential component of the interactions stresses are related by:

$$q_f\left(x = a\right) = p\left(x = a\right)\tan\left(\theta + \alpha\right) \tag{B.5}$$

Substituting Eq. (B.5) and Eq. (B.3), (the latter resolved for $p^{(1)}(x = a)$), into Eq. (B.4):

$$2u_{IIIf}^{(1)} = C \cdot \tan\left(\theta + \alpha\right) 2u_{Iw}^{(1)} = C \cdot \tan\left(\theta + \alpha\right)\left[2u_{III\,0}\tan\theta - 2u_{I0}\right] \tag{B.6}$$

where C is defined by Eq. (4.14). Once the frictional displacement at the first iteration is known, the effective displacement at the second iteration is:

$$2u_{IIIeff}^{(2)} = 2u_{III\,0} - 2u_{IIIf}^{(1)} = 2u_{III\,0} - C \cdot \tan\left(\theta + \alpha\right)\left[2u_{III\,0}\tan\theta - 2u_{I0}\right] \tag{B.7}$$

It follows that:

$$2u_{Ieff}^{(2)} = 2u_{IIIeff}^{(2)} \cdot \tan\theta = 2u_{III\,0}\tan\theta - C\tan\theta\tan\left(\alpha + \theta\right)\left[2u_{III\,0}\tan\theta - 2u_{I0}\right] \tag{B.8}$$

$$2u_{Iw}^{(2)} = 2u_{Ieff}^{(2)} - 2u_{I0} = \left[1 - C\tan\theta\tan\left(\alpha + \theta\right)\right]\left[2u_{III\,0}\tan\theta - 2u_{I0}\right] \tag{B.9}$$

$$2u_{IIIf}^{(2)} = C \cdot \tan\left(\theta + \alpha\right) 2u_{Iw}^{(2)} \tag{B.10}$$

At the n-th iteration, for the mode I wedging displacement has the following expression:

$$2u_{Iw}^{(n)} = 2u_{Ieff}^{(2)} - 2u_{I0} = \left[2u_{III\,0}\tan\theta - 2u_{I0}\right]\left[1 + \sum_{k=1}^{n}\left(-C\tan\theta\tan\left(\alpha + \theta\right)\right)^k\right] \tag{B.11}$$

Upon converge , the following closed-form expressions is then obtained:

$$2u_{Iw} = \left[2u_{III\,0}\tan\theta - 2u_{I\,0}\right]\frac{1}{1+C\tan\theta\tan\left(\alpha+\theta\right)} \tag{B.12}$$

Consequently, both the frictional and the effective mode III displacements closed-form expressions can be finally obtained:

$$2u_{IIIf} = \left[2u_{III\,0}\tan\theta - 2u_{I\,0}\right]\frac{C\tan\left(\alpha+\theta\right)}{1+C\tan\theta\tan\left(\alpha+\theta\right)} \tag{B.13}$$

$$2u_{IIIeff} = \frac{2u_{III\,0}}{1+C\tan\theta\tan\left(\alpha+\theta\right)} + 2u_{I\,0}\frac{C\tan\left(\alpha+\theta\right)}{1+C\tan\theta\tan\left(\alpha+\theta\right)} \tag{B.14}$$